Improving Durability of Turbine Components Through Trenched Film Cooling and Contoured Endwalls

Final Report
1 Oct 2010 to 30 September 2014

Principal Investigator: David G. Bogard, University of Texas at Austin
Co-Principal Investigator: Karen A. Thole, Pennsylvania State University

Report issued May 21, 2015

DOE Award Number DE FE0005540
UTSR Project Number

Submitting organizations:

Turbulence and Turbine Cooling Research Laboratory (TTCRL)
Mechanical Engineering Department
University of Texas at Austin
Austin, TX 78712

Experimental and Computational Convection Laboratory (ExCCL)
Department of Mechanical and Nuclear Engineering
Pennsylvania State University
University Park, PA 16802

Disclaimer

Abstract

The experimental and computational studies of the turbine endwall and vane models completed in this research program have provided a comprehensive understanding of turbine cooling with combined film cooling and TBC. To correctly simulate the cooling effects of TBC requires the use of matched Biot number models, a technique developed in our laboratories. This technique allows for the measurement of the overall cooling effectiveness which is a measure of the combined internal and external cooling for a turbine component. The overall cooling effectiveness provides an indication of the actual metal temperature that would occur at engine conditions, and is hence a more powerful performance indicator than the film effectiveness parameter that is commonly used for film cooling studies. Furthermore these studies include the effects of contaminant depositions which are expected to occur when gas turbines are operated with syngas fuels. Results from the endwall studies performed at Penn State University and the vane model studies performed at the University of Texas are the first direct measurements of the combined effects of film cooling and TBC. These results show that TBC has a dominating effect on the overall cooling effectiveness, which enhances the importance of the internal cooling mechanisms, and downplays the importance of the film cooling of the external surface. The TBC was found to increase overall cooling effectiveness by a factor of two to four. When combined with TBC, the primary cooling from film cooling holes was found to be due to the convective cooling within the holes, not from the film effectiveness on the surface of the TBC. Simulations of the deposition of contaminants on the endwall and vane surfaces showed that these depositions caused a large increase in surface roughness and significant degradation of film effectiveness. However, despite these negative factors, the depositions caused only a slight decrease in the overall cooling effectiveness on the endwall, and in some cases a slight increase in overall cooling effectiveness on the vane model. This was attributed to the insulating effects of the depositions which compensated for the negative factors.

Table of Contents

List of Graphical Materials

Tables

Figures

Executive Summary

This final report describes work completed for the project conducted the University of Texas (UT) and the Pennsylvania State University (PSU). The project provided detailed understanding of the overall cooling effectiveness for combined advanced film cooling and TBC for turbine airfoils and contoured endwalls. These results show how to improve the durability of turbine components especially when subjected to contaminant deposition resulting from the use of coal derived syngas.

Phase I: Planning and Project Coordination

Coordination between the University of Texas and Penn State was done through regular teleconference. There was also significant interaction with Pratt & Whitney, a co-sponsor of this research. There were also regular teleconferences with the project monitor, Robin Ames, at NETL.

Phase II: No Film Cooling

In this phase of the study the focus was on the internal cooling only for the vane and endwall models. Experiments on the endwall conducted at PSU examined impingement cooling effects on overall effectiveness. Experimental temperature measurements were completed for varying coolant flowrates, which were comparable to the cases with film cooling studied later. Impingement cooling generates a uniform distribution of overall effectiveness that consistently increases with flowrate. Experiments with a vane model at UT were done without and with TBC. These experiments showed that the TBC had a dramatic effect on overall cooling effectiveness with the effectiveness levels increasing by factors from 2 to 4. Analytical models based on a 1D thermal transport approximation were developed to predict the effects of TBC. These models were found to generally predict lower levels of enhancement of overall cooling effectiveness than measured. This discrepancy was attributed to the 3D conduction within the vane body.

Phase III: Active Film Cooling

The primary focus of this phase of the research program was to evaluate a number of different cooling configurations including the effects of TBC, varying coolant hole configurations, and the effects of deposition of contaminants on the surface. Endwall experiments at PSU measured overall effectiveness for the cases of film cooling only and combined impingement and film cooling were evaluated for the flat endwall base case. The film cooling performance was not found to change significantly as blowing ratio was increased, except for the improvement in overall effectiveness above the film cooling holes due to in-hole convective cooling. To simulate contaminant deposition on the endwall, the molten wax deposition technique developed by Albert and Bogard (2012) was used. This investigation built upon the study by Lawson et al. (2013) for the effects of contaminant deposition on an adiabatic wall. Since the conjugate endwall accurately models the non-dimensional wall temperature, the surface temperature effects on the dynamic deposition process are correctly modeled in these experiments.

Enhanced film cooling configurations were investigated at UT by testing varying trench and crater configurations formed in simulated TBC. These varying configurations were evaluated in terms of film effectiveness and overall cooling effectiveness. Experiments were conducted with a thick and thin TBC. As expected, the trench configurations had significantly greater film effectiveness than the standard round hole configuration for high blowing ratios, but there was very little effect on the overall cooling effectiveness when TBC was used. This phase of the research program also included the evaluation of the effects of contaminant depositions on overall cooling effectiveness, and whether any of the film cooling configuration would reduce depositions on the surface. Since depositions were much greater on the pressure side of the vane, the focus of these experiments was on a single row of holes on this side of vane with varying trench configurations. Deposition of contaminants was simulated using the molten wax technique developed in our laboratories. The depositions were found to cause a very rough surface and to

significantly degraded the film effectiveness of all film cooling configurations. None of the film cooling figurations were found to significantly reduce the deposition of contaminants to the surface.

Phase IV: Optimized Film Cooling Configurations

In this phase the optimum cooling configurations identified in Phase III were investigated in more detail including flowfield and thermal field measurements. The effects of the endwall contouring were investigated at PSU using a non-axisymmetric endwall contouring with the three-dimensional contour geometry developed by Praisner et al. (2007). With a constant thickness endwall contouring design, there was a variation in the spacing between the impingement plate and the endwall. Therefore, the effects of varying the impingement plate spacing were tested for the cases of impingement only and combined film and impingement. Subsequently, the overall effectiveness with endwall contouring was compared to that of the flat endwall. Finally, flowfield measurements at the trailing edge of the contoured endwall were completed for cases with and without upstream film cooling.

An important part of this phase was a thorough evaluation of CFD predictions of film cooling performance using detailed thermal field measurements above the wall. This evaluation included both a low conductivity (nominally adiabatic) vane model and a high conductivity matched Biot number vane model. This allowed the direct measurement of the conjugated heat transfer effects on the over flowing coolant jets. Results from these experiments showed that the RANS simulation of film cooling jets was able to correctly predict the jet separation, but was very poor in prediction the dispersion of coolant from the jet core. Comparing the thermal fields for the adiabatic and conducting vane surfaces showed that conjugate heat transfer effects were confined to a very thin region near the wall.

Phase V: Supplementary Tasks

Additional computational and experimental studies were conducted at PSU as part of an additional fifth phase of the project. Computational predictions of conjugate heat transfer were compared to the experimental results for both the flat and contoured endwalls. An unstructured grid with wall prism layers was used for the flow domain. Conduction was modeled in the endwall mesh, and the flow was thermally coupled to the endwall. Using a properly scaled conjugate endwall allowed the effect of a thermal barrier coating to be studied for both the flat and contoured endwall geometries. Experimental measurements and computational predictions of effectiveness with a thermal barrier coating were in good agreement.

Introduction

Gas turbine engine efficiency may be improved by increasing the combustor temperature according to an analysis of the Brayton Cycle that governs these engines. Increases in the combustor temperature lead to harsher environments for turbine components. Eventually this can compromise the integrity of the component by exceeding its limits of durability. In order to counteract this effect, engine designers have implemented multiple thermal protection techniques, internal cooling, film cooling, and thermal barrier coatings. Internal cooling of the turbine components is accomplished by routing relatively cooler air from the compressor upstream of the combustor and passing it through passages within the component itself. This process allows for a reduction in the external wall temperature of the component thus increasing its ability to cope with higher combustor temperatures. The second technique is film cooling, in which the coolant air within the internal passages of the component is emitted onto the surface of the vane via discrete holes. This provides a barrier of colder fluid between the hot gas path and the component surface. The final thermal protection technique is to coat the surface of the component with a material with a low thermal conductivity, a thermal barrier coating (TBC). TBC's often have other characteristics to improve the durability of the turbine component, such as resistance to oxidation.

Recent interest has been placed on developing power generation facilities that are capable of using coal derived syngas due to some of its appealing system properties, such as reduced carbon emissions. It is expected that the use of this derived fuel coupled with efforts to drive up the combustor temperature will lead to increased contaminates in the gas path of the engine that remain molten when approaching the surface of the turbine components. This is expected to lead to increased rates of deposition that would detrimentally affect the operating capabilities of the engine and drive down system efficiency.

This project is intended to develop a unique and thorough understanding of how contaminates in a simulated gas path of a gas turbine engine interact with and deposit on the surface of turbine components and what this means in terms of the component durability. Multiple film cooling configurations will be tested under active deposition, such as round holes and a transverse trench, which should provide an understanding of how these various designs perform. Detailed measurements will also be taken of an endwall that is subject to active deposition. This project will also provide an understanding of the contribution that TBC plays in protecting a film cooled vane. Finally, velocity and thermal fields will be measured in order to provide physical insight to why the various cooling configurations perform differently. With this knowledge, future designs may be constructed that allow engines to operate at high levels of performance while mitigating the detrimental effects that are expected from the use of syngas at elevated combustor temperatures.

Experimental Facilities

University of Texas:

Experiments were conducted in a closed loop wind-tunnel which had a modified corner test section with a three vane linear cascade. This tunnel was driven by a 50 hp variable speed fan that allowed the mainstream flow to be maintained at a nominal velocity of 5.8 ± 0.05 m/s at the entrance of the cascade. Figure 1.1 shows a schematic of the wind tunnel test section with the simulated vane cascade. The vane cascade used C3X vanes with a pitch of 457 mm while the 12x scale center test vane had a true chord length of 562 mm. The Reynolds number based on true chord length and exit velocity for all tests was $Re = 7.2 \times 10^5$, which is representative of a typical first-stage turbine vane. The adjustable walls of the tunnel allowed the pressure distribution along the surface of the center test vane to be matched to a computational solution generated for an infinite cascade of C3X vanes. A removable turbulence grid was located 0.50 m upstream of the vane cascade. The grid consisted of multiple 38 mm diameter vertical rods that were spaced at an interval pitch of 85 mm, and generated a turbulence level of nominally $Tu = 20\%$ at the inlet to the vane cascade.

The coolant for the center test vane was supplied by a 7.5 hp blower that drew air from the mainstream and routed it through a heat exchanger that was cooled via liquid nitrogen. The coolant then passed through two separate supply lines that feed the internal passages of the vane. The separate supply lines each had in-line orifice plates and gate valves that allowed for accurate measurement and adjustment of the coolant mass flow rate into the center test vane. For typical test conditions, a coolant temperature of $T_{coolant} = 250$ K and a mainstream temperature of $T_\infty = 300$ K were used, yielding a density ratio of $\rho_{coolant}/\rho_\infty = 1.2$. A schematic of the coolant supply system and the mainstream flow is shown in Figure 1.2.

The center test vane was previously designed and constructed by Dees *et al.* (2013) with improvement and modifications by Albert *et al.* (2012, 2013). Two types of models were used, a very low conductivity model, which was used for measurements of adiabatic effectiveness, and a high conductivity model which designed to match the scaled thermal field through the model and internally. The low conductivity vane models were made of polyurethane foam which had a thermal conductivity $k = 0.048 \pm 0.002$ W/m·K. The high conductivity vane models were constructed from two materials, older models were made of a pourable epoxy resin and newer models were machined from DuPont Corian®. Both the materials had a thermal conductivity of $k = 1.0 \pm 0.1$ W/m·K, which was chosen in order to match the Biot number of the models to that found in a real engine. As shown by Dees et al. (2013), matching the Biot number as well as the ratio of the external to internal heat transfer coefficients is necessary to ensure that the scaled thermal fields are matched. Once this is done, the overall cooling

effectiveness, ϕ, is determined from measurements of surface temperatures, T_w, mainstream temperature, T_∞, and coolant temperature at the inlet to the vane coolant channels, T_c. The overall cooling effectiveness is defined as:

$$\phi = \frac{T_\infty - T_w}{T_\infty - T_c} \tag{1.1}$$

Note that the overall cooling effectiveness, ϕ, is similar to the more frequently used adiabatic effectiveness, η, defined as:

$$\eta = \frac{T_\infty - T_{aw}}{T_\infty - T_{c,exit}} \tag{1.2}$$

However ϕ provides a measure of the combined internal cooling and external cooling while η only provides a measure of the effectiveness of the external film cooling. In this both parameters were measured, but the primary measurement was the overall cooling effectiveness, ϕ, because only this parameter can be used to determine the combined effects of internal and external cooling while incorporating TBC.

As shown in Figure 1.3, the vane design incorporated three internal coolant passages. The forward two passages were connected by a U-bend while the rearmost was a straight radial passage. Figure 3 also shows how the vanes were designed with removable hatches that allow for interchangeable film cooling configurations on the surface of the airfoil. This was important for this study since it allowed a single vane model to have different film cooling configurations depending on the hatch that was used.

An important part of this study was to simulate the deposition of contaminates on a vane model by using a molten wax sprayer as described by Albert *et al.* (2013). A schematic of the wax spray system designed and implemented for this project is shown in Figure 4. The sprayer was designed to have the same form factor as one of the turbulence rods. This allows for the sprayer to be inserted into the tunnel in lieu of one of the rods while still maintaining the functionality of the turbulence grid.

The intention of using wax with a low melting temperature is to ensure that the wax particles remain partially molten prior to impacting the surface of the vane in order to match the adhesion physics of molten particles at the inlet of a high pressure turbine vane. Consequently, the waxes that were chosen for this study have solidification temperatures of $T_{melt/solidification} = 304 - 315$ K. A lumped analysis of these wax particles suggests that, dependent on the mainstream temperature, they should only partially solidify prior to encountering the vane surface. In the case that the melting temperature of the wax is lower than the temperature of the mainstream the particles will of course remain molten unless they approach or come in contact with the cold surface of the center test vane.

The Stokes number of the wax droplets must be properly scaled to that of coal ash particles in an actual engine in order to ensure that the physical behavior of the droplets in the mainstream flow accurately represents real contaminates. The Stokes number is defined as

$$Stk = \frac{\tau}{l_c / U_c} = \frac{\rho_p d_p^2 U_c}{18\, l_c \mu_g} \tag{1.3}$$

where τ is the time needed for an airborne particle to respond to a change in the fluid flow field and l_c/U_c is the time needed for a particle to pass an obstacle of characteristic length, l_c. Consequently, it may be recognized that a particle with $Stk << 1$ will closely follow any changes in the flow field while a particle with $Stk > 1$ will not. It is of utmost importance to generate wax particles of proper size in order to consistently achieve the desired Stokes numbers. The Stokes number of coal ash particles in a real engine was found to be $Stk_d = 1 – 100$ based on the characteristic length of a cooling hole diameter of $d = 0.41$ mm. This was based on the estimation that the particles are spherical with a diameter in the range of 1 – 10 μm and a density of $\rho_p = 1.98$ g/cm^3 according to Bons *et al.* (2007). In order to match the desired value of Stokes number in the wind tunnel the wax particles must have a diameter in the range of $d_{p,wax} = 9 – 90$ μm. The sprayer nozzle size, air pressure, and liquid flow rate were adjusted to obtain the appropriate particle size range. The sizes of the particles were determined using a scanning electron microscope (SEM).

Thermal field measurements were made using a micro-thermocouple probe traversed in the plane normal to the film cooling jet flow. The micro-thermocouple probe was an Omega CHCO-002 thermocouple with 2 *mil* (0.05 *mm*) thick wire. The very thin wire was used to reduce conduction effects on the temperature measurement because of the expected steep temperature gradients within the film cooling jet. To further reduce conduction errors due to the temperature gradients in the wall normal direction, the probe was oriented roughly parallel to the vane surface. In addition, the fine thermocouple bead diameter allowed for tight measurement resolution within the film cooling jet profile.

Penn State:

All thermal and aerodynamic measurements were performed in a low speed, closed loop wind tunnel within The Pennsylvania State University Experimental and Computational Convection Laboratory (PSU ExCCL). The turbine cascade test section was located in a closed loop wind tunnel as shown in Figure 1.4. Driving the flow through the wind tunnel was a 50 hp fan with a 60 Hz variable frequency drive. Downstream of the fan, the flow was split into three flow paths. The top and bottom portions, colored blue in Figure 0.1, passed through a chilled water heat exchanger, while the middle portion passed

through a heater bank followed by a series of screens and flow straightening honeycombs supplying the mainstream flow to the test section. Mainstream temperatures were measured by a 5-thermocouple rake inserted $0.52C_{ax}$ upstream of the blade leading edge at multiple locations across the cascade. The mainstream temperatures measured were averaged to find T_∞. The maximum variation from the average T_∞ for any location was ± 0.6°C.

The secondary flow for the endwall coolant supply was removed from the top channel of the wind tunnel and further cooled by an auxiliary heat exchanger as shown in Figure 1.5. The auxiliary heat exchanger circulated a sub 0°C glycol-water mixture from the auxiliary chiller. To prevent any ice formation on the heat exchanger fins, a desiccant drier was installed upstream of the heat exchanger. A laminar flow element, LFE, measured the total coolant flowrate, before the lines split the coolant feed for three separate plenums, which are described in detail later. The configuration shown in Figures 1.4 and 1.5 provided a mainstream to coolant temperature difference of about 40°C, resulting in a density ratio, DR, of 1.15. Coolant temperature was measured by two thermocouples ~8.7D below the impingement plate, and ~8.7D below the endwall when there was no impingement plate. These thermocouples agreed to within ± 3°C or less.

The linear turbine cascade test section used the Pack-B geometry, consisting of seven low pressure turbine blades with six full passages. The two-dimensional blade geometry, shown in Figure 1.6, has been presented in several studies in the literature (Knezevici et al., 2010; Lynch et al., 2011a, 2011b; Praisner et al., 2007). The operating conditions as listed in Table 1.1 include engine matched Re and geometric specifications. The inlet mainstream velocity was measured by inserting a pitot probe $0.52C_{ax}$ upstream of each blade leading edge. There was very little variation in U_∞ across the cascade, as the standard deviation over the mean was less than 1%. The test section inlet boundary layer parameters were reported previously in Lynch et al. (2011b). Based on the upstream boundary layer measurements, δ/S was 0.071 and the freestream turbulence was 4% at the blade inlet plane (Lynch et al., 2011b).

To ensure uniformity and periodicity of the linear cascade, static pressure taps in the blade midspan were used to measure the pressure distribution before all experiments. A typical set of pressure coefficient, C_p, data is plotted in Figure 1.7 as a function of normalized axial distance for all the blades. The measured C_p agreed well with the inviscid CFD prediction (Lynch et al., 2011a), confirming flow uniformity for all passages.

As mentioned previously, the total coolant flowrate fed to each plenum is measured with an LFE. For experiments using film cooling, the flowrate is adjusted to achieve the desired film cooling blowing ratio. Blowing ratios reported in this paper reflect the average blowing ratio of all ten film cooling holes, hence the use of M_{avg}. The local blowing ratio for each film cooling hole, M_{loc}, is calculated by considering the static exit pressure of each film cooling hole, measured using pressure taps installed in

passage 6. For the cases with only impingement cooling, the mass flow rate of coolant is matched to the total mass flow rate corresponding to the three Mavg values from film cooling. For 95% confidence interval the uncertainty in coolant flowrate is estimated to be ± 3%, using the sequential perturbation method described in Moffat (1988).

Steady state infrared (IR) thermography was used to measure surface temperatures on the endwall. To maximize the spatial measurement resolution and take advantage of the scaled up geometry, a FLIR P20 IR camera was used to measure endwall surface temperatures. The ceiling of the test section contained 16 removable viewing ports, distributed across five blade passages to allow direct optical access for the IR camera. At each viewing location the IR camera was placed perpendicular to the endwall surface at a distance of approximately 56 cm to acquire images. With a camera field of view angle of 25° and a camera resolution of 320 x 240 pixels, the resulting image resolution was 1.3 pixels/mm, which equates to 5.7 pixels/D. Thermocouples were placed in discrete locations on the endwall surface, arranged so that at least two thermocouples were captured in each image. When the thermocouples indicated that steady-state was achieved, five IR images were acquired at each port location. At each location the images were calibrated for emissivity and reflected temperature by minimizing the difference between the thermocouple readings and the image temperatures. The emissivity was typically 0.92 because all endwall surfaces were painted with flat black paint. After calibration, the five images were averaged, exported to an in-house MATLAB program, which assembled the averaged images from each location. Once a complete endwall temperature map was obtained, the data were reduced to ϕ.

The partial derivative method (Moffat, 1988) was used to determine the uncertainty in ϕ. The largest source of uncertainty comes from the calibration of the IR images which provide T_w. The bias error of T_w was estimated to be at most 0.8°C from the difference of the IR image temperatures from the thermocouples. The precision error of T_w was estimated to be 0.3°C from the standard deviation of the five images. Using a confidence interval of 95%, the total uncertainty in measurement of ϕ was estimated to be ± 0.02.

The deposition was dynamically simulated with a molten wax spray technique developed by Lawson et al. (2013; 2012a). The two-nozzle wax injection system depicted in Figure 1.8 was integrated into the turbulence grid upstream of the test section. The nozzle heads, located at one third span, contained a center jet for liquid wax and two air jets directed at the liquid stream to atomize the liquid jet into a mist of particles. Separate pressure regulators were used to independently control the liquid wax flowrate and the atomizing air pressure. The liquid flowrate for each nozzle was set to 1.9 g/s for an estimated particle loading of 0.8 ppm (570 ppmw). The air pressure was set to 138 kPa (20 psi) to generate particles with a median size of 34 μm, as discussed in Lawson et al. (2013), achieving a median

Stk of 6. The liquid wax and air lines were heated such that the injection temperature, measured by a thermocouple in the nozzle, was about 84°C. To achieve a *TSP* of 0.3, the mainstream temperature during deposition, T_∞, was 47°C. The deposition was performed once steady state was reached for these thermal conditions as well as the mainstream and coolant flow conditions of *Re* and M_{avg}. The wax spray lasted more than four minutes, which was beyond the point of deposition equilibrium (Lawson & Thole, 2012a). Following the deposition, photographs were taken of the wax deposition, and a coat of flat black spray paint was applied for the thermal measurements in the second phase of the experiment. The thermal resistance of the paint was estimated to be less than 5% of the thermal resistance of the wax. In the second phase of the experiment, the same mainstream *Re*, coolant flowrate, and ΔT of 40°C were generated for steady state measurements of external wax temperature, T_{wax}. These measurements were made with IR thermography as described earlier.

Time resolved particle image velocimetry (PIV) was used to measure the flowfield in three two-dimensional planes near the trailing edge of the passage suction side as shown in Figure 1.9. Planes A and B were parallel to the exit flow direction, 5*D* and 3*D* from the center of the centerline of the blade trailing edge, respectively. Plane C was parallel to the trailing edge of the passage at an axial location of $1.08C_{ax}$ from the leading edge. Plane C was at an angle of 30° from Planes A and B and crossed the other planes near the trailing edge as shown in Figure 1.9a. Figure 1.9b shows the approximate locations where Planes A and B cross Plane C while viewing the flat endwall predicted contours of turbulent kinetic energy in Plane C. Figure 1.9a also shows the relative locations of the film and impingement holes in the endwall.

During the PIV measurements, the flow was seeded with atomized liquid di-ethyl-hexyl-sebecat (DEHS), resulting in an average *Stk* number much less than one. The particles in the measurement planes were illuminated with an Nd:Nd:YLF laser sheet and imaged with a high speed CMOS camera oriented normal to each measurement plane. Images at Planes A and B were taken for a window size of 1024 x 1024 at 1 kHz and a resolution of 22 pixels/*D*. Images at Plane C were taken for a window size of 1024 x 512 at 2 kHz and a resolution of 16 pixels/*D*. The total number of image pairs recorded was 3000 at Planes A and B, and 6000 at Plane C. The total data acquisition time for all three planes was 3 s. The flow crossed the domain at least 90 times in the data acquisition period. The time delay between laser pulses was chosen based on an estimated bulk movement of 10 pixels, about 1/6 the initial interrogation window size.

Image processing and vector calculation were performed with LaVision software (*DaVis 8.1.4*, 2012). To increase the contrast of the raw images, the sliding minimum of the surrounding three images was subtracted from each image prior to vector calculation. The vector calculation was performed using a cross-correlation over four passes, with a decreasing interrogation window at each pass. Vector post-

processing evaluated possible spurious vectors through two passes of a median filter using universal outlier detection for a 3 x 3 pixel region (*DaVis 8.1.4*, 2012). Empty spaces surrounded by at least two calculated vectors were filled by interpolating between the surrounding vectors.

Results and Discussion

This section is organized by the project phases listed in the project milestones, except for Phase I which involved only the initial project planning and coordination. It is important to note that close collaboration between the University of Texas and Penn State was important in this research program as many techniques and technical insights were achieved by regular teleconference meetings. In the results presented and discussed below, not all tasks listed in the project milestones are discussed. Many of these tasks were focused on developing facility capabilities and experimental techniques, whereas this final report focusses on the overall insights and understanding achieved from the study.

Phase II: No Film Cooling

In this phase of the project, the focus was on the cooling achieved with internal cooling alone for the vane and endwall. This required development and use of matched Biot number models for the vane and endwall. Furthermore, the overall cooling effectiveness was measured with and without TBC of varying thickness on the vane model and endwall. Finally analytical models for predicting the effects of TBC were developed and evaluated.

Task: Develop the conducting endwall model

The experimental endwall model in this study incorporates external film cooling, wall conduction, and internal impingement jet cooling, thereby including the conjugate effects. A simplified model of the endwall with impingement and film cooling is depicted in Figure 2.1a. Figure 2.1b is the corresponding schematic for film cooling only, and Figure 2.1c is for impingement cooling only. The schematics in Figure 2.1 identify the critical parameters and temperatures for the conjugate model development, the experiments and the analysis. All non-dimensional temperatures are scaled by taking the difference between the hot mainstream temperature, T_∞, and the temperature of interest and then dividing by the overall temperature difference between T_∞ and the internal coolant temperature at the plenum supplying the coolant, $T_{c,in}$.

To model overall effectiveness, ϕ, an endwall design that matched Bi, and external to internal heat transfer coefficient ratio, h_∞/h_i, to engine parameters was constructed. Two endwall designs were tested, which included a flat endwall and an endwall with non-axisymmetric contouring (Praisner et al., 2007). Typical endwall parameters found in an engine are reported in Table 1.1. Corian®, a material manufactured by DuPont, was chosen to construct both the flat and contoured endwalls. The external heat transfer coefficients due to the passage flows, h_∞, has been previously reported for the flat and contoured endwalls in this cascade by Lynch et al. (2011b). The measured Nusselt number contours are presented in Figure 2.2a for the case of a flat endwall. Figure 2.2b reports the heat transfer augmentation

for the contoured endwall. The internal heat transfer coefficient, h_i, was calculated from Nusselt number correlations in the literature (Florschuetz et al., 1981; Hollworth & Dagan, 1980). For the contoured endwall, the range of h_i was calculated based on the range of values of *H/D* that existed.

The thermal effect of thermal barrier coatings was simulated experimentally by placing a layer of cork over the conducting endwall. The conductivity and thickness of the cork were chosen to replicate the ratio of thermal resistances that would be seen for a typical engine case. The ratio of thermal resistances, R_{TBC}/R_w, is defined in Table 2.1. The engine and model values for conductivity and thickness of both TBC layer and endwall are reported as well. The condition produced in these tests represents a R_{TBC}/R_w at the lower end but within the range for an engine.

The conductivity of the paraffin wax deposits (T_{melt} = 60°C) is estimated assuming an air porosity of 0.6 in the deposits, similar to the porosity of engine deposition (Richards et al., 1992). The thermal conductivity of coal ash deposition depends on deposition temperature, chemical composition and porosity, which is reflected in the range of $(k_{dep}/k_w)_{engine}$ given in Table 2.1. Table 2.1 also shows a wide range of *Stk* and *TSP* for engines due to the range of possible particle diameters (Bons et al., 2007). The median values of *Stk* and *TSP* in the experiment are chosen to simulate the distribution of these parameters in the engine. The *Stk* is provided for definitions based on the film cooling diameter, *D*, as well as the mainstream length scale, C_{ax}. Because access to the outer surface of the endwall is obstructed by the wax deposition, measurements of ϕ cannot be obtained with IR imaging, and thermocouples on the outer surface of the endwall would change the deposition pattern and the external flow. Instead, the internal effectiveness, ϕ_i, is used to assess the endwall cooling performance after deposition at discrete locations in the passage.

The endwalls were constructed with a geometric configuration and parameters of *Bi* and h_∞/h_i relevant to engine design. The schematic in Figure 2.3a shows the internal and external flat endwall cooling scheme used. Coolant flow is directed into a stagnant plenum passing around a splash plate. The plenum feeds an array of 28 holes in an impingement plate, which feed ten angled film cooling holes in the endwall. The diameter, *D*, is the same for the film and impingement holes. Film cooling holes are inclined at an angle of 30° relative to the surface, corresponding to a hole *L/D* of 5.8. Figure 2.3b shows the locations of the impingement jets and film holes for the contoured endwall. The film cooling hole inlets are staggered between the impingement jets. Each film cooling hole has been rotated to align with the local endwall flow direction. Figure 2.4a shows the hole locations, as well as the endwall streaklines for the flat endwall, which were determined by Lynch et al. (2011b) through an oil flow visualization technique. The flat endwall has some streaklines nearly perpendicular to the mainstream flow direction, resulting in strong secondary flows across the passage. The area outlined in black in Figure 2.2b is used to calculate the area averaged ϕ.

In experiments with TBC, the cork layer extends $1/2C_{ax}$ upstream of the blade leading edge and $1/3C_{ax}$ downstream of the trailing edge as illustrated in Figure 2.3b. When the TBC is applied to the contoured endwall, slits are cut into the cork to allow the cork to lay uniformly over the non-developable contoured surface. The thickness of the cork, t_{TBC}, is $0.45D$. The cork is adhered to the endwall using two to three layers of DAP® Weldwood® Original Contact Cement. The contact cement provides a strong and even adhesion across the surface. The thermal resistance for the combined cork and adhesive layer, given in Table 2.1, was measured by Kistenmacher (2013) for the same cork and adhesive method. To determine the wall temperature and the overall effectiveness with TBC, thermocouples were installed on the wall under the thermal barrier coating. A high conductivity epoxy, k = 4.3 W/m-K, was used to attach the thermocouples to the wall at the locations shown as blue squares in Fig. 2.3b. These points follow two inviscid streamlines referred to as suction side (SS) and pressure side (PS) streamlines.

To study the effects of the internal and external cooling features separately as well as together, the endwall was divided into three sections of two passages. Each section was fed independently by a separate plenum and incorporated a different cooling arrangement shown in Figure 2.5. The center passages, 3 and 4, contained both internal impingement cooling and external film cooling. Passages 1 and 2 had a static plenum and film cooling, but no impingement plate. Passages 5 and 6 incorporated internal impingement cooling only, which imposed crossflow. Instead of exhausting the coolant through film cooling holes, the coolant flowed out of the channel in the vertical direction from a slot above passage 6. The turquoise area of the endwall in Figure 2.5 represents the endwall constructed of Corian® material, and the light area represents the rest of the endwall constructed of medium density fiberboard.

The internal heat transfer coefficient can be calculated using measured temperatures from a simple one-dimensional analysis with knowledge of at least three temperatures directly driving heat transfer. Considering the general case shown in Figure 2.1, the relevant temperatures are T_{film}, T_w, $T_{w,i}$, and $T_{c,in}$. The mainstream temperature, T_∞, cannot be used directly since it is not the external driving temperature with film cooling, as previously described. Since T_{film} is very difficult to measure, and it is the farthest of the four temperatures from the internal convection process, the latter three temperatures are used to determine h_i. To derive an equation for h_i using these three temperatures, the internal convection heat flux is set equal to the conduction heat flux through the wall. Equating two adjacent modes of heat transfer limits the impact of three-dimensional effects. This approach generates the following Equation (2.1) for h_i obtained from the experiments. The h_i obtained from the computational results is directly calculated from the local heat flux and temperature, shown in Equation (2.2).

$$h_{i,\,meas} = \frac{k_w}{t_w}\frac{(\phi_i - \phi)}{(1 - \phi_i)} \tag{2.1}$$

$$h_{i,\,pred} = \frac{q_{w,\,i}}{\left(T_{w,\,i} - T_{c,\,in}\right)} = \frac{q_{w,\,i}}{\left(T_{\infty} - T_{c,\,in}\right)\left(1 - \phi_i\right)} \tag{2.2}$$

Task: Measure overall effectiveness of the endwall with impingement only

For impingement cooling only the ϕ_o contours with impingement hole locations are shown in Figure 2.6a-c. Figure 2.6a specifies direction of coolant exiting the impingement channel under the endwall for the case of impingement only. Although the peak values of ϕ_o are not above 0.5, there is a uniform distribution that increases with blowing ratio. The influence of the external passage flow can be observed in higher effectiveness near the blade suction side compared to the blade pressure side. As hot external flow travels across the middle of the passage, the cooler endwall reduces the temperature of the flow. The cooler passage flow carries less heat to the downstream suction side of the passage resulting in cooler wall temperatures. Laterally averaged ϕ_o is plotted as a function of axial distance in Figure 2.6d. The highest values of ϕ_o occur in the middle part of the passage and decrease after $x/C_{ax} > 0.5$, near the last row of impingement jets. Impingement effectiveness increases with blowing ratio due to the corresponding increase in impingement jet flow rate and internal heat transfer. A similar trend for impingement cooling only was noted for the vane in Williams et al. (2014).

Task: Quantify effects of TBC on the vane model with internal cooling only

Thermal Barrier Coatings

Cork was selected as an appropriate material to simulate the thermal barrier coatings due to the fact that the ratio of TBC to vane thermal conductivity matches the range of ratios that are expected for a real engine. Furthermore the thickness of the cork was selected to also properly scale the model geometry to that of a real engine. A second, thinner, thickness or cork was also selected for use to determine the effects of TBC thickness. Details of the simulated TBC used, and comparisons to actual engine conditions are shown in Table 2.2. To determine the overall cooling effectiveness on models incorporating TBC, measurements of the temperature of the vane model surface below the TBC were required. These vane surface temperatures were measured using an extensive array of surface thermocouples as shown in Figure 2.7.

When using TBC it is important to recognize that the overall effectiveness, ϕ, defined in Equation 1.1, is based on the external "metal" temperature, i.e. the temperature between the vane wall and the TBC as shown in Figure 2.8. When using TBC, the normalized TBC surface temperature was defined as

$$\tau = \frac{T_{\infty} - T_{TBC,e}}{T_{\infty} - T_c} \tag{2.3}$$

Measurements of overall cooling effectiveness on the vane model with and without TBC

Experiments were conducted using the matched Biot number C3X vane model to determine overall cooling effectiveness, ϕ, with no film cooling. Details of the vane model and operational parameters are described in Table 2.3. The effects of TBC thickness on overall effectiveness with no film cooling are presented in Figure 2.9 for two TBC thicknesses and two internal coolant flow rates. The TBC thicknesses (relative to a typical film cooling hole diameter, d) were t/d = 0.6 and t/d = 1.0, which represent a moderate to large thickness for the simulated TBC. The internal coolant flow rates were characterized in terms of the internal channel Reynolds numbers, which were Re = 10,000 and 20,000 for the two cases shown in Figure 2.9. For reference, also shown in Figure 2.9 is the overall cooling effectiveness with no TBC with a coolant flow Reynolds number of Re = 20,000.

Immediately apparent from Figure 2.9 is that the TBC causes a dramatic increase in overall cooling effectiveness with a factor of 2 to 4 increase in ϕ. There was a consistent trend with the thicker TBC having ϕ values approximately 0.1 higher than the thinner TBC. This is expected since the thicker TBC provides greater insulation effects as expected and results in a lower metal temperature. Even though the thicker TBC was 80% thicker than the thin TBC, there was only about a 30% larger increase in overall effectiveness, relative to the no TBC case, when using the thick TBC compared to the thin TBC. An analytical study, described in the next section, was done to determine whether this increase in ϕ was as expected. There was also an approximately 0.1 increase in ϕ values when the internal coolant flow rate was increased from Re = 10,000 to 20,000. Since the internal cooling increases with increase in Re, this increase in ϕ was as expected.

Also noticeable in Figure 2.9 is a strong variation in ϕ values around the vane model with lower values in the leading edge region and higher values farther downstream on both the suction and pressure sides. To determine whether this variation was due to the variation of the external heat transfer coefficient, the ϕ distributions were compared to the h_e distribution as shown in Figure 2.10. Lower values of ϕ in the leading edge region were found to correspond to higher h_e values, and higher ϕ values on the pressure side were found to correspond to lower h_e values. However, on the suction side there was an increase in ϕ values for s/d > 40 even though there was a strong increase in h_e in this region. An explanation for this apparent anomaly is found when considering the internal coolant channels. Figure 2.11 presents a schematic of the cross-section of the vane model showing the internal channels and the relative s/d locations. For these tests both the U-bend and Radial channels were operated with a coolant flow corresponding to Re = 20,000. However, the hydraulic diameter of the Radial channel is significantly smaller than the U-bend channel. This means that, although the Nu for the two internal channels will be similar, the heat transfer coefficient h_e for the Radial channel will be significantly higher. This causes an increase in the overall cooling effectiveness ϕ for s/d > 85 on the suction side and s/d < -44

on the pressure side, which is consistent with the ϕ distributions shown in Figure 2.10. Note that the very low ϕ value on the pressure side at *s/d* = -92 corresponds to a position downstream of the coolant channel so cooling will be poor in this region.

Investigation of analytical models to predict the cooling effects of TBC.

Analytical models were developed in an effort to predict the experimental results for ϕ and τ. The purpose of this study was to determine whether a simple 1-D analysis would provide reasonable predictions of the effects of the TBC. The analysis of heat transfer through the TBC and vane wall results in the following equation for the prediction of ϕ:

$$\phi_{pred} = \frac{\alpha \ (R_{TBC} + R_{e,total})}{R_{i,total} + R_w + R_{TBC} + R_{e,total}} \tag{2.4}$$

where $R_{i,total}$, R_w, R_{TBC}, and $R_{e,total}$ are the thermal resistances for heat transfer through the internal surface, the vane wall, the TBC, and the external surface, respectively. Also, α is the internal heat factor which accounts for the heating of the coolant from the inlet of the vane to any given internal location, and is defined as:

$$\alpha = \frac{T_{e,\infty} - T_{i,\infty}}{T_{e,\infty} - T_{c,inlet}} \tag{2.5}$$

All the thermal resistances in Equation 2.4 (which are defined in Kistenmacher, 2013) could be determined by the physical properties and measurements of the external heat transfer coefficients, except for $R_{i,total}$, because there was not a direct measurement of the internal heat transfer coefficient. Consequently, $R_{i,total}$ was estimated using measurements obtained with the vane model with no TBC. Three estimates were made, one based on convective heat flux through the external surface, the second based on the conductive heat flux through the blade wall, and the third based on a combination of external and conductive heat transfer (details provided in Kistenmacher, 2013). Predicted ϕ values based on these estimates are presented in Figures 2.12 and 2.13 under the headings "Convection", "Conduction", and "Combined". Predictions for the thin TBC, *t/d* = 0.6, shown in Figure 2.12, were generally lower than measured values, with predictions using the "Conduction" technique generally better than the other two estimates. The results obtained with the thick TBC, *t/d* = 1.0, shown in Figure 2.13, were also lower than the measured, but had greater discrepancies than were seen with the thin TBC. Based on these results we concluded that the 1-D thermal transport model was inaccurate, suggesting that 3-D conduction effects within the blade body probably needed to be taken into account.

Phase III: Active Film Cooling

Task: Measure overall effectiveness on endwall with film cooling only

The overall effectiveness contours for film cooling only, ϕ_f, are presented in Figure 3.1a-c. The film cooling holes and plenum boundaries are shown for reference. Although there is near stagnant air below the endwall, conduction caused ϕ_f to be above zero along the pressure side of the passage. In-hole conduction effects are apparent from the increased ϕ_f upstream of the film cooling hole exits. Also, there is evidence of cross passage flow sweeping film coolant to the suction side of the passage in all cases. From the contours, the film cooling jets appear lifted off the surface for M_{avg} = 1.0 and 2.0, while most of the jets remain attached to the endwall for M_{avg} = 0.6. Laterally averaged ϕ_f for film cooling only is plotted as a function of axial distance in Figure 3.1d. The $\overline{\phi_f}$ is almost the same for M_{avg} = 0.6 and 1.0. There is a peak around x/C_{ax} = 0.15, coinciding with the first row of film cooling holes, and a dropoff after x/C_{ax} > 0.55 near the last film cooling hole. Local increases are apparent for M_{avg} = 2.0 at the first row of holes, as well as in the downstream parts of the passage, after x/C_{ax} > 0.3.

Task: Measure overall effectiveness on endwall with combined impingement and film cooling

Overall effectiveness for internal impingement and film cooling, ϕ, is measured in passages 3 and 4 in the same experiment. The measured results are presented in Figure 3.2. Figure 3.2 includes the impingement and film cooling hole locations as well as the boundaries just below the blades, which prevent coolant from crossing from one passage to another in the channel above the impingement plate. Although there is high ϕ throughout much of the passage, ϕ varies significantly and is not uniform. The primary effect of film cooling, conduction within the film cooling holes, results in high ϕ around film holes. The blowing ratio for which this effect is most noticeable is 2.0. Figure 3.2d shows laterally averaged measured ϕ from passage 4 plotted as a function of axial distance. Similar to film cooling only, there is a peak at x/C_{ax} = 0.15 around the first row of film holes, and a decrease in ϕ after x/C_{ax} > 0.55. The influence of impingement can be observed in the increase of $\overline{\phi}$ with blowing ratio. Figure 3.2 also shows a repeat experiment performed for film and impingement at M_{avg} = 1.0. Good agreement between the two experiments for M_{avg} = 1.0 as well as both passages in the contour plots supports the repeatability and reproduceability of the measurements.

The measured data for each cooling arrangement are summarized in Figure 2.4 in which area averaged, using the area in Figure 1.3b, overall effectiveness is presented as a function of M_{avg}. Area averaged ϕ for film and impingement increases from about 0.3 to 0.4 with an increase in M_{avg} from 0.6 to 2.0. Consistent with the laterally averaged data, an increase in blowing ratio improves area averaged $\overline{\overline{\phi_o}}$

more than $\overline{\overline{\phi_f}}$. Figure 3.3 also highlights the improved cooling that results from adding impingement. From this perspective, the increase of $\overline{\overline{\phi}}$ from $\overline{\overline{\phi_f}}$ is larger for higher blowing ratios. In other words $\overline{\overline{\phi}}$ increases faster than $\overline{\overline{\phi_f}}$. This trend was also observed for a flat plate in Panda and Prasad (2012). Alternatively, the effect of adding film cooling to an impingement cooled plate indicates a smaller benefit, especially for M_{avg} = 2.0.

The laterally averaged effectiveness at M_{avg} = 1.0 for film cooling only, impingement only, and film and impingement are plotted together in Figure 3.4. Laterally averaged ϕ for the combined cooling scheme is higher than $\overline{\phi_f}$ or $\overline{\phi_o}$ from x/C_{ax} = 0.05, around the inlets of the film cooling holes, to x/C_{ax} = 0.35, just before the last row of impingement holes. However, $\overline{\phi_o}$ is not much lower than $\bar{\phi}$ indicating that the effectiveness is dominated by impingement cooling. Upstream and downstream, x/C_{ax} < 0.05 and > 0.45, $\overline{\phi_o}$ is higher than $\bar{\phi}$. This unexpected result for impingement only occurs because, after impingement, coolant flows away from the middle of the passage and convectively cools the internal wall in the region x/C_{ax} < 0.05 and > 0.45. With combined film and impingement, the coolant is instead directed into the film cooling holes.

Just downstream of the first row of film cooling holes, at axial distance x/C_{ax} = 0.22, ϕ is plotted across the passage as a function of normalized distance, y/p, in Figure 3.5a-c. Peaks and valleys due to the film cooling jets can be seen in the cases with film cooling. For impingement cooling ϕ_o has a relatively flat distribution from y/p = 0.2 to 0.55, corresponding to the impingement jet locations. For film cooling there is a peak in ϕ_f and ϕ around y/p = 0.25, corresponding to one of the film cooling holes in the diagonal row. The drop after this peak, especially for M_{avg} = 2.0, is attributed to detachment of the film cooling jets from the first row of holes. Figure 2.6a-c also shows that ϕ_o is closest to ϕ_f at M_{avg} = 0.6, but ϕ_o becomes closest to ϕ at M_{avg} = 2.0.

Task: Measure endwall overall effectiveness with deposition

The first objective of the deposition portion of this study is to evaluate the influence of the endwall cooling on the distribution of deposition. Once the deposition has been applied to the endwall, the second objective is to determine the change in endwall cooling performance and the causes for the change. The effect of simulated contaminant deposition is quantified through measurements of external wax temperature, used to compute wax effectiveness (ω), and internal endwall surface temperature, used to compute internal overall effectiveness with deposition ($\phi_{i,dep}$). The experiments considered the cooling configurations of film cooling only and combined film plus impingement for blowing ratios of 0.6 and 1.0.

Figures 3.6 and 3.7 compare the overall effectiveness before deposition, ϕ_f and ϕ, to the external wax effectiveness after deposition, ω_f and ω. Below the ω contours are photographs of the deposition patterns on the endwall prior to the application of black paint for thermal measurements. The pitchwise laterally averaged ϕ and ω are compared in Figure 3.8, which is plotted as a function of the axial direction, x/C_{ax}.

Film Cooling Only

Film cooling only results are shown in Figure 3.6a-b for M_{avg} = 0.6 and Figure 3.6c-d for M_{avg} = 1.0. As the can be seen in the photographs, the deposition generates roughness elements with the size of 0.2 – 0.5D. The deposition is relatively uniform on the endwall, except near the pressure side of the passage. Particles with a Stk_{Cax} greater than one account for 8% of the total particle mass from the particle size distribution measurements reported in Lawson et al. (2013). These larger particles are carried into the pressure side instead of turning with the flow. Toward the upstream portion of the pressure side there are mostly small deposits, and toward the downstream half of the pressure side there are more large deposits. The effect of blowing ratio can be seen by comparing the photographs of the film cooling holes in Figure 3.6b to 3.6d. Some deposits form around the edges of the holes for M_{avg} = 0.6, but at M_{avg} = 1.0, the coolant jets prevent deposits around the hole edges and downstream of the hole for about 1D. Farther downstream of the first row of film cooling holes in Figure 3.6d, it appears there is increased deposition from vortices induced by the film cooling jets bringing particles down to the wall. The deposition downstream of the film cooling holes is consistent with the deposition and flow visualization reported by Lawson and Thole (2012b). In Figure 3.6d there is slightly less deposition just upstream of the first row of film cooling holes compared to farther upstream. As the ϕ_f contours on the left of Figure 3.6c show, the in-hole convection cools the endwall just upstream of the film cooling holes, and increased cooling prevents deposition, as also reported in Albert and Bogard (2013).

For film cooling only at both blowing ratios, the temperatures measured on the deposition surface are the same or warmer than the temperatures measured on the endwall before deposition. The ω_f contours are also not as smooth as the ϕ_f contours, reflecting the roughness elements of the deposition. The roughness appears to degrade the performance of the film cooling jets, since the distances of the jet footprints on the surface are reduced. The roughness increases coolant jet mixing with the mainstream and degrades the effectiveness of the coolant as a protective barrier from the mainstream. The effect is more apparent when the pre-deposition coolant jets are attached, as with M_{avg} = 0.6. Also, the mitigation of deposition just downstream of the film cooling holes allows the film coolant to be more effective at M_{avg} = 1.0 after deposition.

Combined Impingement and Film Cooling

The effectiveness contours and deposition photographs for combined film and impingement cooling are shown in Figure 3.7. The deposition photographs in Figure 3.7 have similar features as Figure 3.6. There are increased levels of deposition near the pressure side, with smaller deposits concentrated toward the upstream pressure side, and larger particles concentrated toward the downstream pressure side and into the wake. Again, the higher blowing ratio mitigates some deposition just downstream of the film cooling holes, but slightly increases deposition farther downstream. It also appears that for M_{avg} = 1.0, there are fewer large deposits across the entire area cooled by impingement cooling, indicating that the local temperature of the endwall has an effect on the accumulation of deposition. The height of deposition was observed to correlate with surface temperature in Albert and Bogard (2013) with larger thicker deposits for higher surface temperatures.

For film and impingement cooling, the ω is significantly less than ϕ for both blowing ratios, meaning the external wax temperatures are warmer than the endwall temperatures without deposition. The deposition causes a greater reduction in effectiveness for the case of combined film and impingement cooling compared to the case of film cooling only. The combined impingement and film cooling performance is degraded due to roughness induced coolant jet mixing like the case of film cooling only discussed earlier. An additional reason ω is less than ϕ is because the deposition has an insulating effect on the endwall. Although the layer of deposition is thin and not uniform, k_{dep} is much less than k_w, and the estimated conduction thermal resistance of the deposition is on the same order of magnitude as the conduction resistance of the endwall. The conduction resistances are also on the same order as the internal convection resistance for impingement cooling. Without impingement (film cooling only), the internal convection resistance is much higher than either of the conduction resistances. Before deposition, film cooling only has lower rates of overall heat transfer compared to combined film and impingement. Therefore for film cooling only, the insulating effect of the deposition is less significant. Because the deposition acts as an insulating layer to the impingement cooled endwall, the wax temperature is warmer than the endwall under the wax ($\omega < \phi_{dep}$). This conclusion however does not reveal whether the external surface of the endwall itself is cooler or warmer after deposition.

Because measurement access to the external endwall temperatures is prevented by the deposits, the endwall cooling performance cannot be directly calculated. However, the internal endwall effectiveness, ϕ_i and $\phi_{i,dep}$, can be directly compared with measurements on the inner side of the endwall. The average internal effectiveness from the four red locations in Figure 1.3b is plotted in Figure 3.9 along with the area averaged ϕ and ω for comparison. The area used for averaging the external effectiveness is

shown in Figure 1.3b. If the overall endwall heat transfer is unchanged before and after deposition, the presence of the deposition layer would insulate the endwall temperatures from the mainstream, and $\phi_{i,dep}$ (with deposition) would be higher than ϕ_i (without deposition). Although the wax does act as an insulator, $\phi_{i,dep}$ is lower than ϕ_i for all four cases by 0.01 – 0.03, which is just slightly above the uncertainty level for the average internal effectiveness. This result means that the overall heat transfer must increase with deposition. An increase in the overall heat transfer can be attributed to roughness effects, which degrade the performance of the film cooling and increase the external heat transfer coefficients. It is worth noting that if the internal wall temperatures are warmer with deposition for both cooling configurations, it is expected that the external wall temperatures are warmer with deposition also.

To understand why deposition decreases endwall overall effectiveness, the external convective heat transfer coefficients with deposition $h_{\infty,dep}$, are estimated with a one-dimensional analysis using the measured temperatures. The location closest to the pressure side in Figure 1.3b is chosen for this analysis, since the external driving temperature there is not affected by film cooling. The heat transfer analysis at this location uses T_∞ as the external driving temperature. The heat transfer is assumed to be primarily in the direction through the thickness of the endwall. Although the lateral surface temperature gradients and endwall vertical temperature gradient are approximately equal at this location in the passage, the lateral heat flux is limited by the lower thermal conductivity of the wax. Equating the external convective heat transfer without film cooling to the internal convective heat transfer results in the following equation for $h_{\infty,dep}$.

$$h_{\infty,dep} = h_i \frac{\left(1 - \phi_{i,dep}\right)}{\omega} \tag{3.3}$$

The quantities of $\phi_{i,dep}$ and ω are directly measured in the experiment. The internal heat transfer coefficient, h_i, is unchanged from the experiments without deposition. Therefore, h_i can be calculated from the internal and external endwall temperature measurements without deposition using Equation (1.1).

The calculation of $h_{\infty,dep}$ at the pressure side location is compared to the local h_∞ measured by Lynch et al. (2011b), which is 41 W/m^2-K. The estimated $h_{\infty,dep}$ ranges from 54 – 81 W/m^2-K (30 – 100% increase) for the different cooling configurations and blowing ratios. The variation in predictions does not correlate with either the cooling configuration or the blowing ratio, but reflects the variation in the deposition surface as well as the uncertainty in the one-dimensional analysis and the measurements.

Task: Design and test various trench/crater type film cooling configurations which could be incorporated in the TBC on a vane

Previous studies, including several in our laboratories, have shown that a shallow trench configuration can provide much improved film cooling adiabatic effectiveness. A major part of this study was to evaluate various trench and crater configurations which were formed within the TBC around film cooling holes. This testing included the ability to improve overall cooling effectiveness and ability to mitigate the effects of depositions of contaminates to the surface. Because of our desire to evaluate the effects on mitigation of deposition effects, we selected the first row of film cooling hole on the pressure side of the vane as shown in Figure 3.10. This was done because previous studies and our own experiments showed that deposition of contaminants was much more severe on the pressure side of the vane.

Schematics of the five film cooling hole configurations tested in this study are shown in Figure 3.11, and a photographic images of the configurations as manufactured are shown in Figure 3.12. For a reference a standard round hole configuration with an inclination angle of 30° and a pitch between hold of $p/d = 3$ was tested. The length of this standard hole was $l/d = 6$ within the vane body material which had a thickness of 3d, but a total length of $l/d = 8.4$ when including the length through the TBC which had a thickness of $t/d = 1.2$. The "ideal trench" and "crater" configurations were based on configurations tested by Dorrington et al. (2007) and shown to significantly improve adiabatic effectiveness. The "modified trench" and "realistic trench" configurations were a new designs tested in this study. The basis of the "modified trench" design was to provide as much TBC coverage as possible while allowing a complete spreading of the coolant along the downstream edge of the trench. The basis of the "realistic trench" design was to have the trench walls slightly displaced from the edge of the coolant holes to allow for tolerances of the placement of the TBC relative to the holes during the manufacturing process. Also, the "realistic trench" had a rounded edge at the top of the trench, again to better mimic a configuration that could realistically be manufactured.

Initial evaluation of the performance of all film cooling configurations was done in terms of the laterally averaged distribution of τ, which is the normalized external surface temperature when using TBC. Because of the low conductivity of the TBC covering, the τ values are very similar to adiabatic effectiveness values, η. A representative result from these comparisons is presented in Figure 3.13 where the τ distributions are presented for all film cooling configurations at a blowing ratio of $M = 2.0$. Also shown on Figure 3.13 is a τ distribution for no film cooling, which provides a reference for the cooling of the surface due to internal cooling alone. The round hole configuration had a τ value just slightly larger than the no film cooling reference, which was expected since the coolant jets with round holes will be

fully separated for high blowing ratios used. Note one of the configurations shown is listed as "Round + SH", which indicated testing of the round hole with the showerhead coolant holes also operational. There was no difference in the τ distributions for the "Round" and the "Round + SH", indicating that the showerhead coolant had no effect at this distance downstream on the pressure side of the vane. All the trench and crater configurations had much better performance than the round hole reference, again as expected since these configurations were expected keep the coolant jets attached. Furthermore the performances of all the trench configurations were essentially the same. This is important in showing that a realistic trench, which could actually be manufactured, still performed as well as the ideal trench for a thick TBC.

The performances of the realistic and ideal trenches are compared to the round hole configuration in Figure 3.14 using contour plots of the τ distributions. At the lowest blowing ratio of $M = 0.5$, the performance of the round hole is similar to the ideal trench. This is due to the coolant jets from the round holes remaining attached for this relatively low blowing ratio. Trench configurations generally show much better performance at higher blowing ratios due to their ability to keep coolant jets attached at the higher blowing ratios. This was shown to be the case in this study as shown in Figure 3.14 where the two trench cases had much better performance for $M \geq 1.0$. Another important observation from Figure 3.14 is the similar performance for the ideal and realistic trenches for blowing ratios as high as $M = 5$, although the realistic trench had a more non-uniform lateral distribution of τ values.

Overall effectiveness measurements were made for also made for all film cooling configurations. It is important to note that ultimately the purpose of film cooling is to minimize the metal surface temperature, i.e. to maximize overall cooling effectiveness, ϕ. Consequently the evaluation of the various film cooling configurations in terms of ϕ is the key evaluation. For these tests the showerhead cooling holes were not used so that the performance of the various cooling hole configurations on the pressure side could be more clearly discerned. Results from these measurements are presented in Figure 3.15 including a reference condition of no film cooling. For $s/d > -10$, i.e. far upstream of the pressure side coolant hole row, the ϕ values were the same for all configurations, which was expected since the film cooling would not be expected to have an effect upstream of the coolant holes. However, for a distance about $15d$ upstream of the coolant holes there was significant increase in ϕ for all film cooling configurations compared to the no film cooling case. Since the surface film effectiveness upstream of the coolant holes is zero, this upstream cooling effect is clearly due to conduction within the vane wall. Downstream of the coolant holes there was an increase in ϕ values for all cooling configurations compared to the no film cooling case. However, the increase in ϕ for the trench configurations were only slightly greater than for the round hole configuration. Recall that the surface cooling for the trench

configurations were much better than the for the round hole configuration, so this result is particularly important because it shows that when using TBC the surface cooling, i.e. film effectiveness, has only a small influence on the overall cooling effectiveness. In fact, the comparable cooling that occurred upstream and downstream of the coolant holes for all film cooling configurations indicates that the convective cooling within the coolant holes has a much greater effect on overall cooling than the film cooling of the external surface. This result was confirmed in multiple tests, and represents a major finding from this study, i.e. when using TBC the type of film cooling hole is essentially irrelevant, and the holes should be viewed as points where local convective cooling of the airfoil metal occurs.

The effect of combined TBC and film cooling on the pressure side of the vane model, with the showerhead and pressure side coolant holes operating, is shown in Figure 3.16. In this figure ϕ is presented for varying M, and performance without TBC is included as a reference. The discrete data points for ϕ with TBC are discrete measurements of the mid-span temperature at the interface of the TBC and the vane wall. To account for spanwise variation downstream of the pressure side coolant holes, a 4x3 array of thermocouples was placed immediately downstream of the pressure side film cooling holes. The discrete data points in Figure 3.16 at locations of s/d = -36, -39, and -48 represent an average of four thermocouples in the array. As would be expected, the presence of a TBC significantly improves the cooling effectiveness of the vane. An important result from these measurements is collapse of the ϕ values downstream of the pressure side cooling holes for varying M when using TBC in contrast to the results without a TBC. This shows that the dominant factor for locally cooling the vane wall is the presence of the TBC and that improved convective cooling through the holes with increasing blowing ratio helps to mitigate the detrimental effect of jet separation.

In the leading edge region with showerhead film cooling holes, there was a dramatic increase in ϕ with film cooling. The ϕ values showed a systematic increase with increasing blowing ratio. The cooling performance of the showerhead is heavily dependent on convective cooling through the holes due to the large number of coolant holes in this region. Furthermore, the showerhead cooling holes are oriented radially, 90º to the streamwise direction. This allows for the coolant to accumulate in the stagnation region of the vane and improve cooling despite jet separation at higher blowing ratios.

In order to increase the blowing ratio for the vane model a greater amount of coolant must be fed into the vane. This results in an altered internal Reynolds number that could affect internal convective heat transfer. As previously discussed, the internal Reynolds number is established by averaging the entrance and exit Reynolds numbers. This average was set to be Re = 20,000±500. The variation in internal Reynolds number through the U-bend is greater with the showerhead running due to the increased coolant loss out of the additional holes. This results in a difference in internal Reynolds number, ΔRe, at the mid-

span of the showerhead of approximately ΔRe = 1,000 for the M = 2.98 case when compared to the M = 0.96 case. Consequently, the change in ϕ near the showerhead shown in Figure 3.16 is primarily due to increased convective cooling through the holes considering that the change in internal Re is relatively minimal, at worst ΔRe = 1,000. However, this difference is significantly larger, approaching ΔRe = 5,000 at the mid-span of the pressure side holes. As previously mentioned, the difference in Re at the inlet and exit of the U-bend is increased with increasing blowing ratio. This means that the pressure side Re decreases as the blowing ratio increases. Consequently, ϕ at high blowing ratio might be expected to decrease due to reduced internal Re and increased separation of the coolant jets. However, referring again to Figure 3.16, it is seen that ϕ increases slightly at the location of the pressure side holes as the blowing ratio is increased. This further supports the claim that the dominant mode of cooling the vane locally, is convective cooling through the holes. In fact, it seems the increased convective cooling through the holes, due to increased blowing ratio, is offsetting the detrimental effects of reduced internal Re and increased jet separation.

Task: Determine the effects of using a thinner TBC on the overall cooling effectiveness for the vane

Given the dramatic effects of TBC that were found for a relatively thick TBC, t/d = 1.0, it was important to test a relatively thin TBC to determine whether these effects would persist. An extensive study of the effects of a "thin" TBC with thickness t/d = 0.6 (see Table 2.2) was completed, and details of this study are presented in Stewart et al. (2014). The key result from this study was that even when the TBC thickness was reduced by 40%, it still had a dominating effect on the cooling, such that the external surface cooling by film cooling had little influence on performance. Comparisons of the overall cooling effectiveness for three cases, TBC t/d = 1.0, TBC t/d = 0.6, and no TBC, are shown in Figure 3.17. These tests were done with showerhead and pressure side coolant holes operational, anda blowing ratio of M = 2.0 for all coolant holes. The no TBC configuration showed a significant increase in overall effectiveness downstream of the pressure side holes between s/d = -50 and -80 with film cooling. However both TBC thicknesses were consistent in showing negligible increases in overall effectiveness with film cooling. This was attributed to the insulating effect of the TBC which significantly reduced the sensitivity to the external film effectiveness. However, in the showerhead region the film cooling caused a substantial increase in overall cooling effectiveness in all cases, with and without TBC. This can be attributed to the extensive in-hole convective cooling in the showerhead region due to the large number of closely spaced holes.

Task: Simulate contaminant depositions on the vane and determine effects on overall cooling effectiveness

Depositions were simulated in our laboratory tests using the molten wax technique described in the section on Experimental Facilities. All film cooling hole configurations shown in Figure 3.11 were tested to determine how well each of these configurations mitigated the growth of contaminant deposits. Depositions in the leading edge region with and without showerhead cooling holes blowing were also tested. Results from these studies are detailed in Davidson et al. (2014b) and Kistenmacher et al. (2014). Key results from the study are highlighted below.

The buildup of depositions on the pressure side of the vane model are shown in Figure 3.18 for the ideal trench and realistic trench configurations. For these tests there was no showerhead blowing. It is evident from the images shown in Figure 3.18 that the buildup of deposits was primarily in the center of the vane model, but this is an artifact due to the loation of the molten wax sprayer being located at the center of the tunnel height. Although the deposition started to cover the trench opening, the trenches were never fully blocked by depositions. The realistic trench had a large deposition the developed from the downstream edge of the trench, which was likely due to the rounded corner for the realistic trench compared to the ideal trench. During extended operation of the contaminant sprayer, the deposition on the trailing edge of the realistic trench would build up and then break off, with a repeating cycle.

A close up of the depositions around the ideal trench is shown in Figure 3.19 showing that the depositions did not fully cover the trench. The thickness of the deposition immediately downstream of the trench was slightly decreased relative to the thickness with no film cooling, but there was no change farther downstream. i.e. beyond 10*d* from the trench trailing edge. As is evident in Figures 3.18 and 3.19, the depositions caused a large increase in surface roughness. This surface roughness caused a significant degradation of the coolant film downstream of the trench as shown by the contours of τ presented in Figure 3.20 before and after depositions. Note that Figure 3.20 also shows a decrease in τ values upstream of the coolant trench. This decrease can be attributed to the increase in the heat transfer coefficient that would be expected to occur with increased surface roughness.

A key result from the study of the effects of depositions was the resulting effects on overall cooling effectiveness. Measurements of ϕ on the pressured side row of holes with the ideal trench and the realistic trench are shown in Figure 3.21 for cases with and without depositions. For this test the showerhead was blocked. The most striking result evident from this figure is there is very little change in ϕ values after deposits have occurred. This is surprising because the large increase in the external heat transfer coefficient that would occur with large roughness with depositions would be expected to be reduce ϕ values. However, in the leading edge region, where there was no film cooling, the ϕ values actually increased following depositions. This increase can be attributed to the insulating effect of the

wax particle depositions, which apparently offsets the increase in the external heat transfer coefficients. A similar effect likely occurs downstream of the film cooling trench where the ϕ values stayed constant, probably due to the insulating effect of the depositions offsetting the degrading effects on the film cooling and the increased heat transfer coefficients due to large roughness.

Phase IV: Optimized Film Cooling Configuration

In this phase of the research program, the endwall studies focused on the contoured endwall that was designed to optimize the cooling of the endwall. Results are presented comparing the cooling of the contoured endwall with the flat endwall discussed previously. An important part of this phase of the research was measurements of the velocity and thermal fields associated with the film cooled vane and endwall. Detailed velocity fields were measured for the contoured endwall flows, and extensive thermal field measurements were made for the film cooled vane model. These measurements are important for validation of CFD predictions of these complex flows.

Task: Apply contoured endwall design to endwall (Penn State)

The contoured endwall design has positive and negative variations in height, shown qualitatively in Figure 1.4c. The contoured endwall was constructed with a constant thickness throughout the passage to maintain similar *Bi* values as the flat endwall. The location of the outlets of the film cooling holes on the upper surface of the contoured endwall have been maintained from the flat endwall. Though the surface gradient varied throughout the passage due to the contour, the hole inclination angle to the local surface gradient is 30° for all holes. As a result, the contoured wall *L/D* varies between 4.2 and 8.0. Like the flat endwall, the film cooling holes are aligned with the local flow direction, which is different for the contoured endwall. Figure 1.4b shows the contoured endwall film hole locations on the contoured endwall streaklines (Lynch et al., 2011b). The contoured endwall streaklines have a larger axial component and are more aligned with the mainstream flow compared the flat endwall. The reduction in secondary flows with the contoured endwall decreases aerodynamic losses in the turbine and also changes the distribution of heat transfer coefficient as presented in the measurements of heat transfer augmentation in Figure 1.2b (Lynch et al., 2011b).

Effect of Changing Impingement Channel Height

Because the contoured endwall has a constant thickness and the impingement plate remains flat, there is a variation in the spacing between the impingement plate and the endwall, *H*. When the leading

and trailing edges of the impingement plate are at a gap height of H/D = 2.9, the H/D throughout the passage varies between 0.6 and 6.3. Therefore, the overall effectiveness with the gap height of H/D = 0.6 is tested for the cases of impingement only and combined film and impingement.

For impingement cooling only the measured ϕ_o for H/D = 0.6 is given in Figure 4.1. Compared to the measured ϕ_o for H/D = 2.9 in Figure 2.1, the effectiveness in the center of the impingement cooled area with H/D = 0.6 is reduced. Increasing effectiveness with H/D within this range is consistent with the trends in the literature for impingement cooling, in which measured heat transfer coefficients increase with H/D, up to an H/D between 1.5 and 4 (Viskanta, 1993). Additionally, ϕ_o for H/D = 0.6 is higher than for H/D = 2.9 in Figure 2.1 near the blade suction side, especially on the upstream half of the blade. The increase on the upstream suction side is the result of internal cooling by the narrow channel flow that develops as the impingement jets are exhausted in the direction indicated in Figure 4.1a. The ϕ_o data are laterally averaged across the pitch direction and plotted as a function of axial distance in Figure 4.1c. The plot shows that the cases with H/D = 0.6 have higher effectiveness than H/D = 2.9 upstream of x/C_{ax} = 0.05. However, for most of the passage ($0.1 < x/C_{ax} < 0.6$), the case with H/D = 0.6 is less effective.

Flat endwall ϕ for combined impingement and film cooling is measured H/D = 0.6 and shown in Figure 4.2. The ϕ contours for H/D = 2.9 are found in Figure 3.2 for comparison. The laterally averaged $\bar{\phi}$ results are plotted as a function of axial distance in Figure 4.2c. Although impingement only ϕ_o has significant differences as H/D changes, combined film cooling and impingement ϕ is almost indistinguishable between the two values of H/D. Measurements of the average Nu for impingement jets staggered with angled extraction holes are available for impingement jet spacing of 5D (Hollworth & Dagan, 1980), which is close to the spacing used here, 4.65D. The angled extraction holes in Hollworth and Dagan (1980) lead to a distinctly different flow, compared to no film extraction for ϕ_o in Figure 4.1. The Nu results of Hollworth and Dagan (1980) are unchanged between H/D = 1 and 2.5, which is in agreement with results in Figure 4.2. The finding that combined film and impingement ϕ does not significantly change between $0.6 < H/D < 2.9$ indicates that the internal h_i for the contoured endwall is not greatly affected by a variation of H/D within this range.

Task: Measure overall effectiveness of the contoured endwall (Penn State)

Film Cooling Only

The overall effectiveness contours for the contoured endwall are shown for film cooling only in Figure 4.3. These figures can be compared to the flat endwall ϕ contours given in Figure 3.1. The laterally averaged ϕ_f are shown in Figure 4.4a, which compares the contoured and flat endwall data. Generally, the results for the contoured endwall are similar to those for the flat endwall, but slightly

higher. With and without contouring, increasing blowing ratio does not produce a significant increase in ϕ_f. In-hole convection becomes more effective as blowing ratio increases, but the film jets detach at higher blowing ratios. Compared to the flat endwall, the film cooling jets, appear to be more attached with endwall contouring. The better film jet attachment with contouring provides better downstream cooling than the corresponding jets on the flat endwall. The two film cooling jets closest to the suction side of the leading edge show the most change from the flat endwall. At M_{avg} = 2.0, these two jets are still partially cooling the endwall. It is observed that these holes are located in a valley of the contour, as seen in Figure 1.4c. Upon leaving the film cooling hole, these jets experience a more favorable pressure distribution coming out of the valley, which promotes jet attachment.

Impingement Cooling Only

The contours of ϕ_o for the contoured endwall are shown in Figure 4.5. Figure 4.4b plots the laterally averaged ϕ_o as a function of the axial distance across the passage for both flat and contoured endwall cases. Like the flat endwall, the effectiveness from impingement shows a significant increase with each increase in blowing ratio. However, the level of ϕ_o is considerably less with the contoured endwall compared to the flat endwall. Since the endwall thickness is uniform and the same as the flat endwall, the differences arise from the changes that the contour wall has on the internal and external heat transfer coefficients. The changes to h_i and h_∞ are examined later. Because the contoured endwall considerably weakens the strength of the passage vortex, the cooling by the vortex downstream of the impingement area is diminished in Figure 4.5 compared to the flat endwall case.

Combined Impingement and Film Cooling

Figure 4.6 shows the overall effectiveness with film and impingement cooling for the contoured endwall. With contouring there is improved film cooling attachment compared to the flat endwall results in Figure 3.2, especially on the upstream row of film cooling holes due to the surface angle effects discussed for film cooling only. For M_{avg} = 1.0 and 2.0, near the blade on the pressure side, ϕ with contouring is about two contour levels higher than ϕ for the flat endwall because the h_∞ is reduced by about 20-30% with contouring, as shown in Figure 1.2b (Lynch et al., 2011b). The laterally averaged ϕ are plotted in Figure 4.4c as a function of axial distance for the both flat and contoured endwalls. Similar to the case of film cooling only, the flat and contoured endwall data are not very different. The overall effectiveness peaks around the first row of film cooling holes and increases with blowing ratio everywhere in the passage. The laterally averaged data for the flat and contoured cases are almost identical to one another.

Figure 4.7 summarizes the overall trends for the contoured endwall data in terms of area averaged overall effectiveness for the area shown in Figure 1.3b. The highest average effectiveness is for the case of combined film and impingement cooling. The contoured endwall values fall very close to the flat endwall values for both cases of H/D = 2.9 and 0.6. With combined film and impingement cooling, endwall contouring has a negligible effect. The cases with film cooling only have the lowest effectiveness. The results for flat and contoured endwalls are similar for film cooling only, although there is a slight increase in effectiveness with contouring for M_{avg} = 1.0 and 2.0 due to better attachment of the film cooling jets from the more favorable pressure gradient.

As previously mentioned, there is a significant reduction in impingement only effectiveness with endwall contouring because of a change in the internal and external heat transfer coefficients. The internal h_i is affected by the contouring because the H/D varies across the passage, and Figure shows how $\overline{\overline{\phi}}_o$ for the flat endwall is less for H/D = 0.6 (the minimum for the contoured endwall), compared to the nominal H/D = 2.9. For combined impingement and film cooling, there is a smaller difference in $\overline{\phi}$ with the same change in H/D. The variation in H/D contributes to lower $\overline{\overline{\phi}}_o$, but the contoured $\overline{\overline{\phi}}_o$ is lower than the flat $\overline{\overline{\phi}}_o$ with H/D = 0.6, as seen in Figure . The reason is that the external h_∞ has also changed with contouring as shown in Figure 1.2b (Lynch et al., 2011b). Although Lynch et al. (2011b), noted that the contouring reduced the overall h_∞ averaged across the whole passage, h_∞ is locally increased for most of the area cooled in the current study. The area surrounding the impingement and film cooling region is overlaid on the augmentation contours in Figure 1.2b. Within this area, the average heat transfer augmentation is +4%. For impingement cooling only, the external driving temperature is T_∞, and higher h_∞ leads to higher wall temperatures. In the other configurations of film cooling only and combined film and impingement, film cooling can locally reduce the external driving temperature. Therefore, an increase in h_∞ has less of a heating effect on a film cooled endwall.

Task: Measure flowfield for the contoured endwall (Penn State)

The average velocity vector field and turbulent kinetic energy (*tke*) fields are obtained with time resolved PIV for the planes in Figure 1.9. The three trailing edge planes are of interest because the passage vortex causes an increase in endwall heat transfer in this region (2011b). The time-averaged in-plane streamlines are given in Figure 4.8 for no film cooling and for two blowing ratios, M_{avg} = 1.0 and 2.0. The main component of velocity is in-plane for Planes A and B, whereas Plane C has a significant out of plane component. The line of sight location of the blade trailing edge is shown in each image for

reference. The background of each image is colored by the measured velocity magnitude normalized by the inlet $U_{\infty,in}$.

The low velocity region in Planes A and B in Figure 4.8 is assumed to be the location of the top of the passage vortex as it circulates through the measurement planes, which are approximately aligned with the inviscid flow direction. The streamlines within the low velocity region converge downstream of the trailing edge line, indicating a significant out of plane velocity component associated with the rotating vortex. The top of the vortex is moving away from the endwall as the streamlines below the top of the vortex are turned upward. The passage vortex appears to be very close to the blade, since the velocities in Plane B are much lower than in Plane A. In Plane C, the passage vortex appears slightly to the right of the line of sight location of the trailing edge because the flow is exiting the passage at a 30° angle to Plane C and the flow exiting the passage is 6.9*D* to the right of its location at the blade trailing edge (see Figure 0.6a).

The approximate *z* (spanwise) location of the top of the passage vortex, or the center of the low velocity area, is labeled in Figure 4.8a as Z_p. As film cooling is introduced in Figure 10d-i, Z_p increases. Table 4.1 reports the non-dimensional Z_p/S for all nine images in Figure 4.8. The endwall film cooling not only increases the height of the passage vortex, but also appears to fill some of the velocity deficit, especially with the highest blowing ratio. The low-velocity region shrinks in Plane A with each increase in blowing ratio. In Planes B and C, the velocity increase is more significant for the change from M_{avg} = 1.0 to 2.0. There are other small changes in the shape of the low-velocity region with film cooling for all three planes. In Plane C, it appears that the passage vortex not only rises from the endwall, but widens as blowing ratio increases.

Contours of normalized turbulent kinetic energy (*tke*) are given in Figure 4.9 for no film cooling a-c, for M_{avg} = 1.0 d-f, and for M_{avg} = 2.0 g-i. The line of sight location of the blade trailing edge is shown in each image for reference. For a two-dimensional velocity field, is *tke* is defined as $\frac{3}{4}\left(\overline{u'^2}+\overline{v'^2}\right)$, which assumes the root mean square of the out of plane velocity fluctuations is an average of the other two components (*DaVis 8.1.4*, 2012). The *tke* is non-dimensionalized by the inlet velocity, $U_{\infty,in}^2$.

The contours of tke characterize the turbulence generated by shear layers as well as the unsteadiness of large flow structures such as the passage vortex and film cooling jets. In the mainstream flow outside of the boundary layer, $tke/U_{\infty,in}^2$ is quite low and only reflects the level entering from the upstream grid as expected. Consistent with the average velocity data, the shear layer at the top of the passage vortex clearly rises moving downstream. In Figure 4.9c, without film cooling, there are two distinct regions of maximum tke, indicating there is a counter rotating vortex located above the passage vortex. Figure 4.9b indicates the presence of another vortex, with two bands of maximum *tke* on top of

one another. With the addition of film cooling, these bands become clearer in Figure 4.9e and h. The presence of a second vortex also explains the elongated region of low velocity observed in the average velocity contours of Figure 4.8c, f, and i. This vortex originates from the suction side leg of the horseshoe vortex (Goldstein & Spores, 1988), or the second vortex could be a vortex induced by the passage vortex (H. P. Wang et al., 1997). Goldstein and Spores (1988) noted that both this second vortex and the passage vortex move away from the endwall along the blade on the suction side of the passage because the pressure is lower away from the endwall.

Film cooling has a significant impact on the tke at the upstream side of the images in Figure 4.9d and g. The levels of *tke* at the upstream side of Plane A approximately double with each increase in blowing ratio. For both blowing ratios tested, the film cooling jets are not well attached and mix into the passage vortex. Although the last film cooling hole in the diagonal row exits at approximately 40*D* upstream of the Plane A images, film cooling has a significant impact on the turbulence levels downstream. Film cooling also increases *tke* levels of the passage vortex in the upstream half of Plane B and on the right side of Plane C. However, the other vortex is weakened with film cooling, as seen on the downstream half of Plane B and at the trailing edge line in Plane C. Figure 4.9i also has a third peak in *tke*, located to the left of the trailing edge line and below the peaks associated with the vortices. This region is also just below the extended region of low velocity in Figure 4.8i.

Task: Measure thermal fields for the film cooled vane model

Thermal field measurements were made downstream of a row of round cooling holes located on the suction side of the vane model as shown in Figure 4.10. The vane model used for this part of the study was different than previous experiments in that the internal cooling was altered to incorporate an impingement cooling configuration. This model was chosen for the thermal field measurements because an extensive CFD prediction of the film cooling performance of this model had previously been completed in our laboratory (details of the CFD study are in Dyson et al., 2012). Since a major motivation for the thermal field measurements was to evaluate CFD predictions, this model was select so that direct comparisons could be made between experimental measurements and CFD predictions.

Experiments and CFD predictions were made for both low conductivity "adiabatic" models and high conductivity "matched Biot number" models. By comparing the overflowing thermal fields for the adiabatic and matched *Bi* models, the interaction between the thermal boundary layer and the coolant jet and the effect of the heat transfer through the vane wall on the coolant jet was determined. The experimental conditions were: d = 6.35 mm, Tu = 20%, DR = 1.2. Measurements were made for M = 0.28, 0.65, 1.11, and 2.41 at x/d = 0, 5 and 10 downstream of a single row of coolant holes on the suction side of the vane. The adiabatic model was constructed of low thermal conductivity polyurethane, k =

0.043 W/m·K, and the thermally conducting vane model was constructed of DuPont Corian® with a thermal conductivity, k = 1.0 W/m·K. As discussed above, DuPont Corian® was selected to match the range of Biot numbers on an actual engine vane. In addition, the CFD vane model simulation by Dyson et al. (2012) used a thermal conductivity of k = 1.0 W/m·K.

Verification that the thermal field measured with a micro-thermocouple probe was consistent with the surface temperatures measured with an IR camera was done as demonstrated in comparison shown in Figure 4.11. In this figure the normalized air temperature above the wall is defined in the same way as adiabatic effectiveness, i.e.:

$$\theta = \frac{T_\infty - T_{x,y,z}}{T_\infty - T_{c,hole\ exit}} \quad (2)$$

The contours of θ above the wall shown in Figure 4.11 were measured at x/d=5 and these contours are shown intersecting with the contour plots of η at the same location. The IR temperature measurements agree within uncertainty with the micro-thermocouple probe measurements close to the surface.

The thermal fields were compared in two ways, first between the experimental adiabatic and conducting vane results, and second between the experimental and computational results. The thermal fields measured above the conducting vane surface were expected to differ from the adiabatic vane results because of the interaction of the coolant jet with the thermal boundary layer along the conducting vane surface.

At the lowest blowing ratio, M = 0.28, comparison are shown in Figure 4.12 at x/d = 5 and 10. The coldest region of the experimental jet in Figure 4.12 (a) and (b) was attached to the vane surface, and the coolant jet has spread across the entire pitch. The coldest region of the experimental coolant jet above the adiabatic vane at x/d = 5 in Figure 4.12(a) is θ = 0.35, but the coldest region above the conducting vane model at the same position for the same blowing ratio (Figure 4.12 (e)) is θ =0.40. A similar trend can be seen by comparing Figure 4.12 (b) to (f), where the core of the coolant jet is colder above the conducting wall at x/d = 10. For M = 0.28, the vane wall was cooling the coolant jet. In contrast, the CFD simulation for M = 0.28 predicted a jet core that was much colder than the experimental result, and hence for the CFD case the conducting wall warms the core of the jet at x/d = 5, Figure 4.12 (c) and (g). Both the experimental and CFD coolant jets spread vertically to about y/d= 1.0, indicating the CFD simulation can predict the proper level of wall-normal spreading. The experimental jet above the adiabatic vane spread laterally across the entire pitch at x/d = 5 and 10, but the CFD jet above the adiabatic vane only spread to z = ±1d from the centerline at x/d = 5 and 10. Outside of the region very near the vane surface, the experimental thermal profiles above the adiabatic and conducting vane models were very similar.

For M = 0.65, the simulation again predicted a much colder jet core than the experimental results, shown in Figure 4.13. The magnitude of this discrepancy is emphasized in Figure 4.14, showing centerline profiles of θ for the CFD and experimental coolant jets at x/d = 5 above the conducting vane surface. In addition, the coldest region of the jet core for the simulation was not attached to the surface, see Figure 4.13 (c) and (d), while the coldest region of the experimental jet core was attached to the vane surface as shown in Figure 4.13 (a) and (b). In Figure 4.14, the peak θ value is over-predicted by a factor of 2 while the local ϕ at the surface was only over-predicted by ~20%. However, the distance from the surface to the peak of the jet and the total height of the coolant jet were well predicted. This highlights the importance using full thermal fields to evaluate computational predictions of film cooling.

The effect of the conducting vane wall is highlighted in Figure 4.15 which shows centerline profiles of θ and IR surface temperature measurements at x/d = 5 and 10. In Figure 4.15, for y/d < 0.5, the jet profile above the conducting vane surface is warmer (lower θ) than the jet above the adiabatic vane surface because $T_w > T_{aw}$ or $\theta_w < \theta_{aw}$. Above y/d = 0.75, the centerline profiles are identical within uncertainty above both vane surfaces. However, at x/d = 10, the experimental coolant jet profiles above both vane surfaces are almost identical even for y/d < 0.5. This is expected because the local conducting wall temperature measurement, T_w, is near to the local adiabatic wall temperature measurement, T_{aw}.

Results for measurements made with M = 1.1 and 2.4 are presented in Stewart and Bogard (2015). As would be expected, the coolant jets for these higher blowing ratios were clearly detached. Consequently the interaction with the wall was small and the thermal fields for the adiabatic and conducting walls were very similar. The computational simulations still predicted much colder core temperatures in the coolant jets than measured experimentally indicating an under prediction of the coolant dispersion.

Phase V: Supplementary Tasks

Task: Computational predictions of conjugate heat transfer

Computational Methods

Conjugate simulations for the endwall with and without TBC are performed using commercial computational fluid dynamics (CFD) software (*FLUENT 13.0.0*, 2010). The segregated pressure-based SIMPLE algorithm is used to solve the steady-state RANS and energy equations using the SST k-ω turbulence model (Menter, 1994) for closure with second-order spatial discretization schemes. The SST k-ω model is chosen because it has shown reasonable agreement with experimental results in turbomachinery applications (Dyson et al., 2012; Lynch et al., 2011a; Panda & Prasad, 2012; Schwänen & Duggleby, 2009; Snedden et al., 2009).

Computational Domain and Boundary Conditions

The computational grid begins $3.5C_{ax}$ upstream of the blade leading edge in the inlet flow direction to capture the flow development upstream of the cascade, as shown in Figure 5.1a. At this location, a velocity inlet is applied with a freestream velocity of 10.5 m/s and a boundary layer profile benchmarked to the measurements by Lynch et al. (2011b). The inlet velocity, turbulent kinetic energy, and specific dissipation profiles are generated using the boundary layer code TEXSTAN (Crawford, 2009) to match the measured momentum thickness Reynolds number, $Re_\theta = 1330$, at the measurement location $2.85C_{ax}$ upstream of the blade leading edge in the inlet flow direction (Lynch et al., 2011b). The temperature distribution at the inlet is uniform with a T_∞ similar to the experiments. An outflow boundary condition is applied $1.5C_{ax}$ downstream of the blade trailing edge in the axial (x) direction. Symmetry is imposed at the top of the domain, which is located at the midspan of the blade in the experiments. A single blade passage is simulated using periodic boundaries that extend vertically through the entire domain, cutting through the mainstream section, the TBC and endwall, four film cooling holes, the impingement channel, and the plenum.

A mass flow inlet boundary condition is applied at the bottom of the computational plenum, which is located $65D$ below the impingement plate to reflect the dimensions of the plenum in the experiments. The mass flow rate and temperature applied at the boundary match the conditions in the experiment for that blowing ratio. Air properties used for the flow are incompressible-ideal gas for density, polynomial fits to temperature for thermal conductivity and specific heat, and Sutherland's law for viscosity. The properties used for the endwall and TBC are listed in Table 1.1.

A thermally-coupled wall interface is used at all conjugate solid/fluid boundaries. For the simulations with TBC, a cork layer extends along the entire endwall surface of the computational domain except for the film cooling holes. A thermally-coupled wall interface is also used at the boundary between the TBC and the endwall. All other wall surfaces in the domain are modeled as adiabatic.

Grid Generation and Convergence

Separate unstructured grids are generated for the conducting endwall solid, the conducting TBC solid, and the flow domain. A commercial grid generation program (*Pointwise 17.1r3*, 2013) is used to generate the unstructured grids for the endwall and TBC geometries, shown in Figure 5.1b. The endwall grid contains 1.5 million cells, and the cork grid contains 0.3 million cells. For the flow domain, the Advancing-Front/Local-Reconnection unstructured grid generation software, AFLR3 (Marcum & Gaither, 1999), is used to create a high-fidelity tetrahedral grid with wall-normal prism layers to resolve the boundary layer on key surfaces. Prism layers are grown on the blade, the entire external endwall

surface, the internal endwall surface, the film cooling holes, and the impingement holes such that $y^+ < 1$ at the first grid point. The unstructured grid for the flow is depicted in Figure 5.1c, showing a slice in the x-plane through the mainstream, film cooling holes, impingement channel, impingement holes, and plenum. Figure 5.1d shows a slice in the y-plane through a film cooling hole inlet and an impingement hole. The initial grid size for the flow domain is 9.8 million cells.

Convergence of a simulation is achieved when the normalized residuals are less than $1x10^{-4}$ and the area-averaged endwall ϕ changes by less than 0.0015 over 500 iterations. To ensure grid independence, the initial grid that contains a total of 11.3 million cells is uniformly refined to a grid containing a total of 18.5 million cells. The difference in the solution for M_{avg} = 1.0 from the refined grid relative to the initial grid for area-averaged ϕ over the endwall is $1x10^{-4}$. Also, the total heat flux at the internal endwall surface varies by less than 0.25% for the refined grid relative to the initial, nominal grid. Thus, it is concluded that the nominal grid is of sufficient resolution for the present conjugate heat transfer predictions and that the CFD solutions are grid insensitive.

As a check for consistency between simulations, the area-averaged *Nu* on internal endwall surface is compared between the cases with and without TBC. For M_{avg} = 1.0 the difference is only 0.1%, showing that the internal flow predictions are consistent. Likewise the predicted internal $\overline{\overline{Nu}}$ for M_{avg} = 2.0 has a difference of 0.4% between the cases with and without TBC.

Flat endwall

The predicted overall effectiveness results are compared to the measured results in Figure 5.2 for two blowing ratios. The predicted effectiveness contours are repeated for two passages to correspond to the two passages where measurements were taken. Figure 5.2 includes the impingement and film cooling hole locations as well as the boundaries just below the blades, which prevent coolant from crossing from one passage to another in the channel above the impingement plate. There are good comparisons between the measured and predicted ϕ contours at both blowing ratios in Figure 5.2. The simulations correctly predict the extent of lateral conduction into the uncooled areas. The strong effect of in-hole convection at M_{avg} = 2.0 is well predicted in the high ϕ at the exits of the film cooling holes. As seen for M_{avg} = 1.0, there are some discrepancies between the measured and predicted ϕ in the areas with film cooling. As other studies have found, RANS CFD often has difficulty predicting mixing in the film cooling jet shear layer and difficulty predicting film attachment. For M_{avg} = 2.0, a small difference can be seen in the influence of the film cooling jets closest to the suction side. Although the CFD correctly predicts the jet detachment, the predicted ϕ here is less than in the measurements. The simulations are under-predicting

the cooling influence that the detached jets have on the wall, which was also observed by Dyson et al. (2012).

A small difference in the predicted ϕ is also seen downstream in the passage for both blowing ratios. In the downstream region of Figure 5.2b and c, the simulations show a slightly lower ϕ (by about 0.05) and a warmer endwall than the experiment. These differences are attributed to small heat losses present in the experiment that are not captured in the simulation. An example of a surface modeled as adiabatic that loses heat to the surrounding environment is the downstream side of the Corian® endwall. The endwall is surrounded on the side and bottom by medium density fiberboard shown in Figure 1.3a. The conduction heat loss from the downstream sides of the endwall into the fiberboard (k = 0.3 W/m^2) is estimated to be on the same order as the convective heat transfer into the endwall from the mainstream. The lateral conduction in this part of the endwall is estimated to be an order of magnitude less because the temperature gradients in this region of the endwall are small.

Contoured endwall

Measurements and computational predictions of the contoured endwall overall effectiveness ϕ are shown in Figure 5.3 for blowing ratios of M_{avg} = 1 and 2. Overlaid on the contour plots are the locations of the film cooling holes, impingement holes, plenum boundaries and an elevation map for the height of the contoured endwall. Dotted lines indicate negative height values where there is a valley. The measured results are shown for Passage 4. The area used for averaging is shown by the box in Figure 1.3b. The agreement between the predictions and measurements of the contoured endwall effectiveness is similar to that of the flat endwall effectiveness. In general the predictions show good with the measurements of contoured endwall effectiveness except for the common failure of RANS to accurately predict film cooling jet attachment (Dyson et al., 2012; Foroutan & Yavuzkurt, 2014; Stewart & Bogard, 2014), which was also noted for the flat endwall simulations. Downstream in the passage the predicted ϕ is about 0.05 less than the measurements. This difference between the measured and predicted ϕ downstream was also observed for the flat endwall and was attributed to the heat losses from boundaries assigned as adiabatic in the simulations.

Task: Measure endwall overall effectiveness w/ TBC (Penn State)

Flat endwall

Measurements and predictions of the flat endwall overall effectiveness with TBC, ϕ_{TBC}, are found for the cooling configuration with both impingement and film cooling. Figure 5.4a-f compares ϕ_{TBC} to the cases without TBC along the inviscid streamlines shown in Figure 4.8. The experimental ϕ without TBC

and the predicted data (in red) have been extracted from the measured and predicted contours. The measurements of ϕ_{TBC} (dashed black lines) are only available at the discrete thermocouple locations. Higher cooling performance is observed along the inviscid streamlines with TBC compared with the no TBC cases for the three blowing ratios. TBC increases the effectiveness on the PS line at all measurement locations by nearly a constant amount. The increase from ϕ to ϕ_{TBC} varies on the SS along the length of the streamline, especially between $0.2 < s/C_{ax} < 0.7$. The local effects of film cooling seen on the endwall without TBC have been smeared out in ϕ_{TBC} because the TBC is insulating the endwall from the external flow, which includes film cooling.

Both ϕ_{TBC} and ϕ are under-predicted downstream in the passage for $s/C_{ax} > 0.7$. These discrepancies are attributed to the conduction losses at the endwall sides previously discussed. The predictions show some influence of the film cooling on ϕ_{TBC}, which cannot be observed in the discrete measurements. The agreement of the predictions in the passage is better on the PS than the SS streamline because the prediction of film cooling attachment is relevant on the SS streamline only. The PS crosses a few film cooling holes at or just upstream of the hole exits, which show up as sharp peaks in Figure 5.4a-c. Other than at these peaks, the endwall along the PS streamline is influenced by internal cooling only.

The SS crosses the downstream path of several film cooling jets, and in these areas, the predictions diverge slightly from the measurements. The SS ϕ data, shown in Figure 5.4d-f, have a sharp drop around $s/C_{ax} = 0.2$ following a film cooling hole. At $M_{avg} = 0.6$ (Figure 5.4d), the SS line continues to slowly decrease consistent with the behavior of an attached film cooling jet. As blowing ratio increases (Figure 5.4e and f), the behavior reflects that of a detached and reattached jet because measured ϕ slightly increases again following the sharp drop. For $M_{avg} = 1.0$ between s/C_{ax} of 0.1-0.5 (Figure 5.4e), the prediction shows the trend of detachment and reattachment, but the resulting ϕ is over-predicted. For $M_{avg} = 2.0$, there is a slight under-prediction of ϕ on the SS (Figure 5.4f) around s/C_{ax} of 0.1-0.3, which is related to the deficiency of RANS in predicting the diffusion of detached film cooling jets.

The predictions of ϕ_{TBC} are plotted as contours in Figure 5.5a and b. Compared to the predicted flat endwall contours without TBC in Figure 5.2b and d, ϕ_{TBC} is significantly higher at all locations on the endwall. The TBC provides a substantial cooling effect on the endwall, which is particularly uniform above the impingement area. The TBC insulates the endwall from the external film cooling as well as from mainstream heating. When the blowing ratio is increased from $M_{avg} = 1.0$ to $M_{avg} = 2.0$, the area of high effectiveness under the TBC widens, and the effectiveness around the film cooling holes increases from increased in-hole convection.

The average increases in ϕ due to changes in the blowing ratio and due to the addition of TBC are compared in Table 5.2. The change due to an increase in M is calculated from an area-average across the

impingement area shown in Figure 1.3b. The $\overline{\overline{\Delta\phi_{TBC}}}$ is the average difference between and ϕ (without TBC) at the measurement locations along the streamlines. The values in the table show that the improvement due to the addition of TBC is greater than the improvement from increasing blowing ratio. Changing blowing ratio is less effective at reducing endwall temperatures than adding TBC, which is consistent with the findings on the vane surface (Davidson et al., 2014).

The improvement in ϕ due to the TBC for the measurements and simulations is plotted in Figure 5.6. The values for the experiment are those given in Table 5.2. The predicted data are an average across the entire conducting endwall surface. Figure 5.6 demonstrates that $\overline{\overline{\Delta\phi_{TBC}}}$ slightly increases with blowing ratio. The measured and predicted values for improvement with TBC agree very well, indicating that the discrete thermocouple locations used to measure the endwall temperatures under the TBC provide a good indication of the effect throughout the passage.

The net heat flux reduction with TBC, Δq_r, can be calculated at the endwall outer surface using Equation (5.1).

$$\Delta q_r = \frac{q_w - q_{w,TBC}}{q_w} \tag{0.4}$$

The predicted Δq_r is plotted in Figure 5.6 for the y-axis on the right side of the plot. The simulations predict that Δq_r also increases with blowing ratio. Similar trends are found for Δq_r when applied to the other endwall surfaces (the internal endwall surface and the film cooling holes). Therefore, adding TBC gives a greater reduction in q_w, and a greater improvement in ϕ at higher blowing ratios. With TBC, the endwall is insulated from the hot mainstream, but still influenced by the internal cooling. In general, internal cooling becomes more effective as blowing ratio increases, generating higher heat transfer coefficients. The insulating effect of the TBC allows the internal impingement and in-hole convection to cool the endwall more effectively.

The measured and predicted dimensionless temperatures on the outer TBC surface, τ, are shown in Figure 5.7 for the flat endwall. Experimental measurements are shown for three blowing ratios along the top, and computational predictions are on the bottom. Because the TBC has a higher thermal resistance than the endwall, τ is generally lower than ϕ and is closer in appearance to the effectiveness for an adiabatic wall, η. However, as blowing ratio increases, impingement and in-hole convection begin to have a greater effect on τ, as seen in the measurements. The insulating effect of TBC is also observed in the lower temperatures measured at the exit of the holes compared to the cases without TBC.

The corresponding predictions for τ show reasonable agreement to the experiments. Like the measurements, the simulations predict temperatures on the outside of the TBC to be hotter than the bare

endwall. However, the predicted τ is slightly lower than measured, especially for M_{avg} = 2.0. Also, the simulation for M_{avg} = 1.0 in Figure 5.7d shows more jet attachment than the experiments, which is consistent with the ϕ comparison at the same blowing ratio. The fully detached jets for M_{avg} = 2.0 in Figure 5.7e have less influence on τ compared to the experiments, a trend that was also observed for ϕ.

The external TBC temperatures, τ, along the inviscid SS and PS streamlines are given in in Figure 5.8a-c. The data within the film cooling hole outlets have been removed. As blowing ratio increases, the SS data (dashed lines) stay about the same or slightly decrease because the film cooling jets become detached from the TBC surface. The decreased cooling by the film jets is balanced by the increased cooling by internal impingement. In contrast, the PS data increase with each increase in blowing ratio because the PS streamline does not cross the path of the film cooling jets, and is influenced by internal cooling. As discussed in reference to the contours, the simulations predict lower τ than measured and less influence on τ by the internal cooling than the experiments indicate. This is more apparent on the PS after $s/C_{ax} > 0.25$, and on the SS after $s/C_{ax} > 0.7$, downstream of the film cooling jets. Despite the under-prediction, the trends of the data in the passage are well captured by the simulations.

Contoured endwall

The film cooling overall effectiveness with and without TBC along the two streamlines is plotted in Figure 5.9a-f. The flat endwall data are in black, and the contoured endwall data are in red. The data for the PS streamline are in Figure 5.9a-c, and for the SS streamline in Figure 5.9d-f. The lines with open symbols are the continuous ϕ_f measurements without TBC, and the filled symbols are the discrete ϕ measurements with TBC obtained from the streamline thermocouples in Figure 1.3b. Without TBC, the endwall ϕ_f for the flat and contoured endwalls are almost the same on the PS, but have some differences on the SS. On the SS, the contoured ϕ_f is higher than the flat ϕ_f between $0.1 < s/C_{ax} < 0.6$ for M_{avg} = 1.0 and 2.0. This region of the SS streamline crosses the first row of film cooling holes and the jet paths. Therefore, the improvement with contouring shows the better attachment of these film cooling jets with contouring. For M_{avg} = 0.6, the film cooling jets are mostly attached for the flat endwall, so the contouring has almost the same performance as the flat endwall.

With TBC, the film cooling overall effectiveness improved for all cases. Again, the flat and contoured ϕ_{TBC} is very similar on the PS, but there are some differences on the SS from better film cooling attachment for the contoured endwall cases. However, ϕ_{TBC} is less affected by film cooling attachment than ϕ or τ because the TBC layer is between the film coolant and the ϕ_{TBC} measurement. Therefore, the differences between the flat and contoured endwall ϕ_{TBC} are expected to be smaller than for the flat and contoured endwall ϕ or τ. Although there was no difference between the flat and contoured endwall ϕ for

M_{avg} = 0.6, the contoured ϕ_{TBC} is slightly higher than the flat ϕ_{TBC} for M_{avg} =0.6. The jet attachment for the flat endwall at this blowing ratio may be diminished when TBC is included because of the vertical cuts made in the TBC for the film cooling holes. In that case, endwall contouring can provide some improvement in the film cooling attachment over the flat endwall with TBC even at the lowest blowing ratio.

The impingement only overall effectiveness is also plotted along the streamlines in Figure 5.10a-f. The flat endwall data are in black, and the contoured endwall data are in red. Figure 5.10a-c is for the PS streamline, and Figure 5.10d-f is for the SS streamline. The ϕ_o data without TBC are in the open symbols connected by the continuous lines. The contoured endwall ϕ_o is consistently lower than the flat endwall ϕ_o, which is consistent with the observations from the contour plots and laterally averaged plots based on the trends with *H*/*D*. The reasons for the decrease in ϕ_o with contouring is because both h_i and h_∞ are reduced with contouring as discussed previously. The discrete filled symbols are the ϕ_o under the TBC for the flat and contoured cases. With TBC, the effectiveness is significantly higher than without TBC. The peak overall effectiveness increases by about 0.2 with TBC. Although the contoured ϕ_o was consistently lower than the flat ϕ_o without TBC, the differences between the flat and contoured lines with TBC are not significant for any of the cases at either streamline. Therefore, the reduction in impingement effectiveness is not as significant as the improvement with TBC. Additionally, the effect of increased h_∞ with contouring does not matter as much when TBC is added because the TBC provides insulation between the endwall temperature measurement and the mainstream convective heating.

Although the impingement only TBC effectiveness increases slightly for each increase in blowing ratio, the effect of internal cooling on the external TBC temperature is limited by the insulation of the TBC. Additionally, the contoured endwall τ_o is even less than the flat endwall τ_o. This trend is of reduced impingement effectiveness with contouring is consistent with the results of contoured and flat ϕ_o without TBC, discussed in Phase IV. The contoured effectiveness is consistently less than the flat endwall because the internal heat transfer coefficients are reduced, and because the external heat transfer coefficients are increased within the impingement array area. The h_i is reduced from the flat endwall because the distance from the impingement plate varies with contouring, and values of *H/D* higher and lower than 2.9 have decreased h_i. Additionally, the measured h_∞ with contouring is 10-30% higher than the flat endwall for much of the impingement area (Lynch et al., 2011b) as shown in Figure 1.2.

Computational predictions for the contoured endwall overall effectiveness data with combined film and impingement cooling with TBC are shown in Figure 5.11. Elevation lines of the contoured endwall height, the cooling holes and the plenum boundaries are overlaid. Comparing Figure 5.11 to the corresponding flat endwall predictions in Figure 5.5, there are not many differences. The contoured

endwall is slightly warmer than the flat endwall downstream in Figure 5.11a. However, the contoured endwall is approximately 5% cooler than the flat endwall in the valley of the contour in the upstream half toward the suction side. Since the TBC is insulating the endwall from most of the effects of film cooling, the cooler endwall is due to locally improved impingement cooling. Therefore, the contoured endwall impingement effectiveness can actually improve locally compared to the flat endwall, when the coolant is exhausted through film cooling holes.

The measured overall effectiveness for the contoured endwall with combined film and impingement cooling is compared to the flat endwall along the PS and SS streamlines in Figure 5.12a-f. The contoured endwall measurements are in red, and the corresponding flat endwall results are shown in black. The data for the PS streamline are in Figure 5.12a-c, and SS streamline in Figure 5.12d-f. The solid lines and open symbols are the continuous ϕ measurements without TBC, and the filled symbols are the discrete ϕ_{TBC} measurements obtained from the thermocouples under the TBC, shown in Figure 1.3b. Without TBC the endwall ϕ for the flat and contoured endwalls are almost the same as discussed previously. With TBC, the flat and contoured ϕ_{TBC} are also similar on the SS, but larger differences are observed between the flat and contoured ϕ_{TBC} on the PS in Figures 5.12a-c. Upstream of the first row of film cooling holes, which have a peak around $s/C_{ax} = 0.1$, the contoured endwall ϕ_{TBC} is less than the flat endwall. Upstream of the film cooling hole exits, impingement and in-hole convection are the only cooling mechanisms. In addition, this upstream pressure side region of the contoured endwall passage has increased h_∞ over the flat endwall by up to 30%, as shown in Figure 1.2b (Lynch et al., 2011b). Although the TBC is insulating the endwall to some extent, locally increased h_∞ upstream of film cooling increases heating from the mainstream. Downstream of the film cooling holes on the PS ($s/C_{ax} > 0.2$) the opposite trend is found; the contoured endwall ϕ_{TBC} is greater than the flat endwall. This local increase with contouring is aligned with the region of higher effectiveness in the predictions previously discussed. In this downstream pressure side region of the contoured endwall passage, the h_∞ is 10-30% less than the h_∞ for the flat endwall, from Figure 1.2b (Lynch et al., 2011b). Locally reduced h_∞ helps to further protect the endwall from the mainstream heating. The changes in h_∞ from the flat to contoured endwall along the SS streamline are not as significant, ranging from about -10% to 10%, from Figure 1.2b (Lynch et al., 2011b).

TBC effectiveness, τ, for the contoured endwall with film and impingement cooling is shown for measurements in Figure 5.13a-c and predictions in Figure 5.13d-e. Just like the flat endwall, the effects of in-hole convection and impingement cooling are more limited for τ compared to ϕ. In areas upstream of the film cooling hole exits, the τ for the contoured endwall is even less than τ for the flat endwall. This trend between the flat and contoured endwalls is consistent with the ϕ_{TBC} results in Figure 5.12a-c for the

upstream portion of the PS streamline. High values of τ are found in areas where there is film cooling attachment. Compared to the flat endwall, the contoured endwall has better attachment of the film cooling jets at the two highest blowing ratios. The predictions in Figure 5.13d and e show a similar extent of film cooling attachment as the measurements. However, the effect of film cooling is slightly over-predicted for M_{avg} = 1.0 and under-predicted for M_{avg} = 2.0, similar to other cases in the study. Because of the reduced impact of the internal cooling and the increased film cooling attachment with the contoured endwall, there is not much change in the contoured endwall τ as blowing ratio increases.

Conclusions

The experimental and computational studies of the turbine endwall and vane models completed in this research program have provided a comprehensive understanding of turbine cooling with combined film cooling and TBC. To correctly simulate the cooling effects of TBC requires the use of matched Biot number models, a technique developed in our laboratories. This technique allows for the measurement of the overall cooling effectiveness which is a measure of the combined internal and external cooling for a turbine component. The overall cooling effectiveness provides an indication of the actual metal temperature that would occur at engine conditions, and is hence a more powerful performance indicator than the film effectiveness parameter that is commonly used for film cooling studies. Furthermore these studies include the effects of contaminant depositions which are expected to occur when gas turbines are operated with syngas fuels. Detailed conclusions from the endwall studies performed at Penn State University and the vane model studies performed at the University of Texas are presented below.

The conjugate heat transfer methodology was implemented for an endwall geometry. Through experiments and computational simulations, the effects of cooling configuration, contaminant deposition, endwall contouring and a thermal barrier coating on the overall cooling effectiveness were studied. Additionally, flowfield measurements revealed the interactions between film cooling and the passage secondary flows, which affect the three-dimensional endwall heat transfer. Relevance of the scaled temperatures relied on proper scaling of the parameters important to conjugate heat transfer, namely the Biot number and ratio of heat transfer coefficients, as well as geometry and Reynolds numbers. The endwall was constructed from Corian and designed with a generic cooling arrangement of angled cylindrical film cooling holes. The film cooling was fed from an array of impingement jets under the endwall. Infrared thermography was used to measure the endwall temperatures.

The relative influence of impingement and film cooling for the flat endwall base case was compared first. With regards to the overall effectiveness, film cooling was most effective around the film cooling holes due to in-hole convection. The film cooling jet attachment was generally poor, but was better for the lowest blowing ratio. These initial studies showed that the dominant factor in endwall cooling was from impingement, which generated a uniform distribution of overall effectiveness and increased with blowing ratio. The combined film and impingement cooling case demonstrated high effectiveness from in-hole convection as well as uniformly high effectiveness across the impingement array.

Molten particle deposition was experimentally simulated on the endwall of a gas turbine blade cascade. The experiments matched the relevant thermal and flow parameters that influence the deposition behavior. Some mitigation of deposition was observed for the higher blowing ratio, at the film cooling hole exits and in the areas cooled by in-hole convection and impingement. This result indicates that the

correct flow and thermal boundary conditions are needed to accurately simulate the deposition itself. In addition, an effective strategy to mitigate deposition may be to increase or improve turbine cooling. In addition to the thermal behavior of the endwall affecting the amount of deposition, the deposition affects the thermal performance of the endwall. Decreased effectiveness was measured after deposition on the internal endwall surface for all cases. The deposition added an insulating layer to the endwall but also degraded the performance of the cooling systems. The reasons for higher endwall temperatures with deposition are attributed to two roughness effects. There is a reduction in the film cooling performance because of the additional mixing that occurs from the roughness of the surface. Second, the roughness increases the external heat transfer coefficients, which increases the overall endwall heat transfer.

The contoured endwall investigation began with an investigation of the effect of varying the impingement channel height. Although the impingement only effectiveness decreased when the impingement channel height was changed, the combined film and impingement effectiveness was not significantly decreased. The results with contouring showed similar trends, with contouring decreasing the impingement only case but having little effect on the combined film and impingement case. Higher external heat transfer coefficients for the upstream half of the passage with contouring also contributed to additional heating of the impingement only case. When film cooling was included in the contoured endwall, the effective external driving temperature was reduced. Therefore, higher heat transfer coefficients with contouring did not increase heating to the endwall. The influence of the passage vortex on the cooling of the endwall near the trailing edge was diminished for the contoured endwall compared to the flat endwall. Another reason for improved film cooling effectiveness with contouring is that the film cooling jets have better attachment to the surface compared to a flat endwall if there is a local favorable pressure gradient due to the local surface gradient in the contouring. Although the impingement height, external heat transfer coefficients, and film cooling attachment changed with contouring, these effects together resulted in unchanged average overall effectiveness from the flat endwall to the contoured endwall with combined film and impingement. The existence of local changes in the overall effectiveness from the flat to the contoured endwall indicated that film cooling and internal cooling should be considered in the design of a contoured endwall in order to optimize the contoured endwall heat transfer performance.

The flowfield measurements of the passage vortex show that the passage vortex size, location and strength are influenced by the film cooling. The passage vortex convected away from the endwall, and film cooling increased this motion towards the midspan. Multiple bands of increased *tke* were measured at the trailing edge indicating the presence of a secondary vortex above the passage vortex. When film cooling was added, the trailing edge plane became less organized, and at the highest blowing ratio a third

area of peak *tke* appeared. Therefore, it was found that the passage flowfield and vortices are affected by the presence of film cooling.

Computational predictions of conjugate heat transfer were compared to the experimental results for both the flat and contoured endwalls. Generally there was good agreement between the predictions and the measurements except for the common failure to accurately predict film cooling jet attachment and a 5% under-prediction of effectiveness downstream of the cooling area. The conjugate simulations with TBC in predicted the correct trends across the passage for both the endwall and the TBC surface. Overall, the conjugate heat transfer simulations in conjunction with a suitable unstructured grid provide reasonable temperature predictions that can be used to analyze the endwall heat transfer.

The improvement in effectiveness for the flat endwall with TBC was quantified with measurements of overall effectiveness with TBC and TBC effectiveness for the flat and contoured endwalls. The improvement in overall effectiveness due to TBC was evaluated and found to be significant. Adding TBC produced a greater improvement in overall effectiveness than the improvements achieved by increasing blowing ratio alone. The TBC protected the endwall from the hot mainstream, reduced heat transfer, and allowed the internal cooling to be more effective. As blowing ratio increased, a greater improvement in overall effectiveness was observed because the TBC was more effective at reducing heat transfer. The reduction in heat transfer with TBC also caused the outer TBC temperature to be higher in comparison to the endwall temperature without TBC. The predictions of TBC effectiveness were reasonably close to the measurements, and the correct trends were captured by the simulations.

Measurements and predictions of the TBC effectiveness and overall effectiveness with TBC were also completed for the contoured endwall for all of the cooling arrangements. Like the comparisons between the flat and contoured endwall without TBC, there was improved film cooling attachment with contouring, and decreased impingement effectiveness with contouring because the contouring reduced internal heat transfer and increased external heat transfer. Although the TBC effectiveness of the flat and contoured endwalls behaved as expected based on the overall effectiveness without TBC, the overall effectiveness with TBC had some differences. With TBC, the impingement only overall effectiveness was not reduced with contouring, but was the same between the flat and contoured endwalls. Because the TBC insulates the endwall from the external effects, the local increases in external heat transfer with contouring are mitigated with TBC. Additionally the improvement with TBC is much more significant than the difference between the flat and contoured overall effectiveness without TBC.

The experimental program with the vane model included determining the effects of TBC with internal cooling alone, with combined internal cooling and external film cooling, and with deposition of contaminants to the external surface. Again the key to this test program was to correctly simulate the conjugate heat transfer effects by using a matched Biot number model. When a simulated TBC was added

to the matched Biot number model, the material and thickness of the simulated TBC was carefully selected to again match the appropriate scaling parameters with engine conditions. It is important to recognize that TBC thicknesses on actual engine operations vary significantly from 5% of the airfoil wall thickness to 50% of the wall thickness. Our test program included a moderate range of TBC thicknesses from 20% to 33% of the vane wall thickness which corresponded to 60% to 100% of the coolant hole diameter when using film cooling.

Tests with no film cooling, i.e. with internal cooling alone, showed that TBC had a dramatic effect on overall cooling effectiveness with the effectiveness levels increasing from $\phi = 0.1$ to $\phi = 0.45$ in the leading edge region and from $\phi = 0.4$ to $\phi = 0.8$ on the pressure side of the vane model. Givne the dramatic increase in overall cooling effectiveness, analytical models based on a 1D thermal transport approximation were developed to determine whether these enhancements due to TBC were predictable. Although these models generally predicted slightly lower levels of enhancement of overall cooling effectiveness than measured, the predictions were close enough to measured values to confirm that the measured enhancements were reasonable. The slight discrepancy between measurements and predictions was attributed to the 3D conduction within the vane body.

An important part of this study was the evaluation of enhanced film cooling configurations that can be formed with the TBC coatings. The specific configurations tested were craters, ideal trench, modified trench, and realistic trench, along with a standard round hole configuration for reference. Measurements of the "TBC effectiveness," i.e. the normalized temperature on the external surface of the TBC gave a good indication of the film effectiveness, and confirmed that the various trench configurations formed from TBC performed well, with much greater film effectiveness than round holes, particularly at very high blowing ratios, i.e. $M > 2$. The most important configuration tested was the "realistic trench" which was designed to simulate a trench that could realistically be manufactured given the tolerances for applying TBC to engine parts. For the TBC thickness of 1D the performance of the realistic trench was similar to that of the ideal trench, but for a TBC thickness of 0.6D, the performance of the realistic trench was significantly degraded.

Evaluation of the combined effects of film cooling and TBC on overall cooling effectiveness has never been done before, and provided one of the most significant results from this research program. Experiments were conducted with the vane model with varying film cooling configurations and coolant blowing ratios. The focus of these experiments was on the pressure side of the vane model because this test program would also include deposition of contaminants, which is known to be most severe on the pressure side of a turbine airfoil. The most striking results from this experimental program was the discovery that overall cooling effectiveness was very insensitive to coolant hole configuration and to the blowing ratio used. Examining this more closely, we found that even though the external film

effectiveness ranged from very low to very high, the overall cooling efficiency was about the same. Furthermore the increases in overall cooling effectiveness in the vicinity of the coolant holes were similar upstream of the coolant and downstream of the coolant holes. Since external film effectiveness occurs only downstream of a coolant holes, this indicates that the primary cooling that occurs with film cooling holes when combined with TBC is the convective cooling within the holes. This indicates a dramatic paradigm shift in the design process when using combined film cooling and TBC for cooling turbine components. For these designs there is no advantage in using exotic (and expensive) film cooling holes which improve external film effectiveness. Simple round holes will be sufficient, and they should be located to take advantage of localized convective cooling in the holes, without regard to the coolant flow outside the hole. Furthermore operation at high blowing ratios, for which round hole coolant jets will separate, should not be a concern because the primary cooling comes from within the coolant hole.

This research program also included the evaluation of the effects of contaminant depositions on overall cooling effectiveness, and whether any of the film cooling configurations would reduce depositions on the surface. Simulations of the deposition molten contaminant materials on the surface of the van model was done over a long enough period to achieve essentially a steady state deposition thickness. The depositions were found to cause a very rough surface and to significantly degraded the film effectiveness of all film cooling configurations. Although all film cooling configurations showed some partial blockage by the depositions, none of the configurations were completely blocked. None of the film cooling figurations were found to significantly reduce the deposition of contaminants to the surface. The key result from the testing of the effects of contaminant deposition on the vane model came from the measurements of overall cooling effectiveness. Despite the significant degradation of the external film effectiveness due to blockage and increased surface roughness, and to increased external heat transfer coefficients that would occur with increased surface roughness, the overall cooling effectiveness did not decrease, and in some cases slightly increased. This was attributed to the insulating effect of the layer of contaminant deposition on the surface of the TBC. The thickness of this contaminant deposition was similar to the thickness of the TBC, and it had lower thermal conductivity than the vane model, though higher than the simulated TBC. When scaled to engine conditions, the thermal conductivity of the wax layer deposits in our experimental simulation were determine to be a appropriate approximation of the thermal conductivity of the deposits that would occur in engine conditions. Consequently our results showing that contaminant depositions do not have a serious effect on the overall cooling effectiveness are a good indication of the expected performance at engine conditions.

References

Albert, J.E. and Bogard, D.G., (2012) "Experimental Simulation of Contaminant Deposition on a Film Cooled Turbine Airfoil Leading Edge," *ASME J. of Turbomachinery*, Vol. 134, pp. 051014.1-10.

Albert, J. E., & Bogard, D. G. (2013). Experimental Simulation of Contaminant Deposition on a Film-Cooled Turbine Vane Pressure Side With a Trench. *J. Turbomach., 135*(5), 051008. doi:10.1115/1.4007821

Bons, J. P., Crosby, J., Wammack, J. E., Bentley, B. I., & Fletcher, T. H. (2007). High-Pressure Turbine Deposition in Land-Based Gas Turbines From Various Synfuels. *J. Eng. Gas Turbines Power*, *129*(1), 135. doi:10.1115/1.2181181

Crawford, M. E. (2009). *TEXSTAN (academic version)*. Austin, TX: University of Texas.

Davidson, F.T., 2012, "An Experimental Study of Film Cooling, Thermal Barrier Coatings and Contaminant Deposition on an Internally Cooled Turbine Airfoil Model," Ph.D. Dissertation, University of Texas at Austin.

Davidson, F. T., Kistenmacher, D. A., & Bogard, D. G. (2014a). Film Cooling With a Thermal Barrier Coating: Round Holes, Craters, and Trenches. *J. Turbomach., 136*(4), 041007. doi:10.1115/1.4024883

Davidson, F.T., Kistenmacher, D.A., and Bogard, D.G., (2014b) "A Study of Deposition on a Turbine Vane with a Thermal Barrier Coating and Various Film Cooling Geometries," ASME J. of Turbomachinery, Vol. 136 pp. 041009.1-11.

DaVis 8.1.4. (2012). (Version 8.1.4). Ypsilanti, Michigan: LaVision Inc. Retrieved from www.lavision.de/en

Dees, J.E., Bogard, D.G., Ledezma, G.A., and Laskowski, G.M., 2013, "Overall and Adiabatic Effectiveness Values on a Scaled Up, Simulated Gas Turbine Vane" *ASME J. Turbomachinery*, Vol. 135 pp. 051017.1-10.

Dennis, R. A., Shelton, W. W., & Le, P. (2007). Development of Baseline Performance Values for Turbines in Existing IGCC Applications. In *Proceedings of ASME Turbo Expo* (pp. GT2007–28096). ASME. doi:10.1115/GT2007-28096

Dyson, T. E., Bogard, D. G., & Bradshaw, S. D. (2012). Evaluation of CFD Simulations of Film Cooling Performance on a Turbine Vane Including Conjugate Heat Transfer Effects. In *Proceedings of ASME Turbo Expo* (pp. GT2012–69107).

Dorrington, J.R., Bogard, D.G., and Bunker, R.S. (2007) "Film Effectiveness Performance for Coolant Holes Embedded in Various Shallow Trench and Crater Depressions," In *Proceedings of ASME Turbo Expo* (GT2007-27992).

Florschuetz, L. W., Truman, C. R., & Metzger, D. E. (1981). Streamwise Flow and Heat Transfer Distributions for Jet Array Impingement with Crossflow. *J. Heat Transfer*, *103*(2), 337–342. doi:10.1115/1.3244463

FLUENT 13.0.0. (2010). (Version 13.0.0). Cannonsburg, PA: ANSYS Inc.

Foroutan, H., & Yavuzkurt, S. (2014). Simulation of the Near-Field Region of Film Cooling Jets Using RANS and Hybrid URANS/LES Models. In *Proceedings of ASME Turbo Expo* (pp. GT2014–25959). ASME. doi:10.1115/GT2014-25959

Goldstein, R. J., & Spores, R. A. (1988). Turbulent Transport on the Endwall in the Region Between Adjacent Turbine Blades. *J. Heat Transfer*, *110*(4a), 862–869. doi:10.1115/1.3250586

Hollworth, B. R., & Dagan, L. (1980). Arrays of Impinging Jets with Spent Fluid Removal through Vent Holes on the Target Surface—Part 1: Average Heat Transfer. *J. Eng. Power*, *102*(4), 994–999. doi:10.1115/1.3230372

Kistenmacher, D. A. (2013, May). *Experimental Investigation of Film Cooling and Thermal Barrier Coatings on a Gas Turbine Vane with Conjugate Heat Transfer Effects*. University of Texas at Austin.

Kistenmacher, D.A., Davidson, F.T., & Bogard, D.G., (2014) "Realistic Trench Film Cooling With a Thermal Barrier Coating and Deposition," ASME J. of Turbomachinery, Vol. 136 pp. 091002.1-12, DOI: 10.1115/1.4026613

Knezevici, D. C., Sjolander, S. A., Praisner, T. J., Allen-Bradley, E., & Grover, E. A. (2010). Measurements of Secondary Losses in a Turbine Cascade With the Implementation of Nonaxisymmetric Endwall Contouring. *J. Turbomach., 132*(1), 011013. doi:10.1115/1.3072520

Lawson, S. A., Lynch, S. P., & Thole, K. A. (2013). Simulations of Multiphase Particle Deposition on a Nonaxisymmetric Contoured Endwall With Film-Cooling. *J. Turbomach., 135*(3), 031032. doi:10.1115/1.4007598

Lawson, S. A., & Thole, K. A. (2012a). Simulations of Multiphase Particle Deposition on Endwall Film-Cooling. *J. Turbomach., 134*(1), 011003. doi:10.1115/1.4002962

Lawson, S. A., & Thole, K. A. (2012b). Simulations of Multiphase Particle Deposition on Endwall Film-Cooling Holes in Transverse Trenches. *J. Turbomach., 134*(5), 051040. doi:10.1115/1.4004756

Li, R., Wang, L., Yang, T., & Raninger, B. (2007). Investigation of MSWI fly ash melting characteristic by DSC–DTA. *Waste Management*, *27*(10), 1383–1392. doi:10.1016/j.wasman.2006.11.017

Lynch, S. P., Thole, K. A., Kohli, A., & Lehane, C. (2011a). Computational Predictions of Heat Transfer and Film-Cooling for a Turbine Blade With Nonaxisymmetric Endwall Contouring. *J. Turbomach.*, *133*(4), 041003. doi:10.1115/1.4002951

Lynch, S. P., Thole, K. A., Kohli, A., & Lehane, C. (2011b). Heat Transfer for a Turbine Blade With Nonaxisymmetric Endwall Contouring. *J. Turbomach.*, *133*(1), 011019. doi:10.1115/1.4000542

Marcum, D., & Gaither, J. (1999). Mixed Element Type Unstructured Grid Generation for Viscous Flow Applications. In *AIAA Computational Fluid Dynamic Conference* (p. AIAA 1999–3252). Norfolk, VA.

Menter, F. R. (1994). Two-equation eddy-viscosity turbulence models for engineering applications. *AIAA Journal*, *32*(8), 1598–1605. doi:10.2514/3.12149

Moffat, R. J. (1988). Describing the uncertainties in experimental results. *Exp. Therm. Fluid Sci.*, *1*(1), 3–17. doi:10.1016/0894-1777(88)90043-X

Panda, R. K., & Prasad, B. V. S. S. S. (2012). Conjugate Heat Transfer From a Flat Plate With Combined Impingement and Film Cooling. In *Proceedings of ASME Turbo Expo* (pp. GT2012–68830).

Pointwise 17.1r3. (2013). (Version 17.1 Release 3). Fort Worth, TX: Pointwise, Inc.

Praisner, T. J., Allen-Bradley, E., Grover, E. A., Knezevici, D. C., & Sjolander, S. A. (2007). Application of Non-Axisymmetric Endwall Contouring to Conventional and High-Lift Turbine Airfoils. In *Proceedings of ASME Turbo Expo* (pp. GT2007–27579). doi:10.1115/GT2007-27579

Richards, G. A., Logan, R. G., Meyer, C. T., & Anderson, R. J. (1992). Ash Deposition at Coal-Fired Gas Turbine Conditions: Surface and Combustion Temperature Effects. *J. Eng. Gas Turbines Power*, *114*(1), 132–138. doi:10.1115/1.2906295

Schwänen, M., & Duggleby, A. (2009). Identifying Inefficiencies in Unsteady Pin Fin Heat Transfer. In *Proceedings of ASME Turbo Expo* (pp. GT2009–60219). ASME. doi:10.1115/GT2009-60219

Snedden, G., Dunn, D., Ingram, G., & Gregory-Smith, D. (2009). The Application of Non-Axisymmetric Endwall Contouring in a Single Stage, Rotating Turbine. In *Proceedings of ASME Turbo Expo* (pp. GT2009–59169). ASME. doi:10.1115/GT2009-59169

Stewart, W. R., & Bogard, D. G. (2015). Experimental Thermal Field Measurements of Film Cooling Above the Suction Surface of a Turbine Vane. *J. Eng. Gas Turbines Power.* ; 137(10):102604-102604-10. doi: 10.1115/1.4030263

Stewart, W. R., Kistenmacher, D.A., & Bogard, D. G. (2014). Effects of TBC Thickness on an Internally Cooled and Film Cooled Model Turbine Vane. In Proceedings of ASME Turbo Expo (pp. GT2014–27117). ASME. doi:10.1115/GT2014-27117

Viskanta, R. (1993). Heat transfer to impinging isothermal gas and flame jets. *Experimental Thermal and Fluid Science*, *6*(2), 111–134. doi:10.1016/0894-1777(93)90022-B

Wang, H. P., Olson, S. J., Goldstein, R. J., & Eckert, E. R. G. (1997). Flow Visualization in a Linear Turbine Cascade of High Performance Turbine Blades. *J. Turbomach., 119*(1), 1. doi:10.1115/1.2841006

Wang, Q., Tian, S., Wang, Q., Huang, Q., & Yang, J. (2008). Melting characteristics during the vitrification of MSWI fly ash with a pilot-scale diesel oil furnace. *Journal of Hazardous Materials, 160*(2-3), 376–381. doi:10.1016/j.jhazmat.2008.03.043

Williams, R. P., Dyson, T. E., Bogard, D. G., & Bradshaw, S. D. (2014). Sensitivity of the Overall Effectiveness to Film Cooling and Internal Cooling on a Turbine Vane Suction Side. *J. Turbomach., 136*(3), 031006. doi:10.1115/1.4024681

Zelesky, M. (2011, September 20). personal communication.

Publications

Davidson, F.T., Kistenmacher, D.A., and Bogard, D.G., (2014) "Film Cooling with a Thermal Barrier Coating: Round Holes, Craters, and Trenches," ASME J. of Turbomachinery, Vol. 136 pp. 041007.1-11.

Davidson, F.T., Kistenmacher, D.A., and Bogard, D.G., (2014) "A Study of Deposition on a Turbine Vane with a Thermal Barrier Coating and Various Film Cooling Geometries," ASME J. of Turbomachinery, Vol. 136 pp. 041009.1-11.

Davidson, F.T., Dees, J.E., and Bogard, D.G., (2011) "An Experimental Study of Thermal Barrier Coatings and Film Cooling on an Internally Cooled Simulated Turbine Vane," ASME Gas Turbine Expo, paper GT2011-46604, Vancouver, Canada.

Kistenmacher, D.A., Davidson, F.T., and Bogard, D.G., (2014) "Realistic Trench Film Cooling with a Thermal Barrier Coating and Deposition," ASME J. of Turbomachinery, Vol. 136 pp. 091002.1-12, DOI: 10.1115/1.4026613

Mensch, A. and Thole, K.A. (2014) "Overall Effectiveness of a Blade Endwall with Jet Impingement and Film Cooling," *Journal of Engineering for Gas Turbines and Power*, 136, pp. 031901.

Mensch A. and Thole, K.A. (2014) "Conjugate Heat Transfer Measurements and Predictions of a Blade Endwall With a Thermal Barrier Coating," *Journal of Turbomachinery*, 136, pp. 121003.

Mensch, A. and Thole, K.A. (2014) "Simulations of Multiphase Particle Deposition on a Gas Turbine Endwall with Impingement and Film Cooling," ASME International Mechanical Engineering Congress & Exhibition, IMECE2014-36682.

Mensch A. and Thole, K.A. (2015) "Conjugate Heat Transfer Analysis of the Effects of Impingement Channel Height for a Turbine Blade Endwall with Internal Jet Impingement and External Film Cooling," *International Journal of Heat and Mass Transfer*, 82, pp. 66-77.

Mensch A. and Thole, K.A. (2015) "Overall Effectiveness and Flowfield Measurements for an Endwall with Non-Axisymmetric Contouring," recommended for ASME Turbo Expo, GT2015-42706.

Stewart, W.R. and Bogard, D.G., (2015) "Experimental Thermal Field Measurements of Film Cooling Above the Suction Surface of a Turbine Vane," *J. Eng. Gas Turbines Power.* ; 137(10):102604-102604-10. doi: 10.1115/1.4030263.

Stewart, W.R., Kistenmacher, D.A., and Bogard, D.G., (2014) "Effects of TBC Thickness on an Internally Cooled and Film Cooled Model Turbine Vane," ASME Gas Turbine Expo, paper GT2014-27117, Düsseldorf, Germany.

Dissertations and Theses

Mensch, A., 2015, "Using Conjugate Heat Transfer to Assess the Cooling Performance on a Turbine Endwall," Ph.D. Dissertation, Pennsylvania State University.

Davidson, F.T., "An Experimental Study of Film Cooling, Thermal Barrier Coatings and Contaminant Deposition on an Internally Cooled Turbine Airfoil Model," Ph.D. Dissertation, Univ. of Texas, 2012.

Kistenmacher, D.A., "Experimental investigation of film cooling and thermal barrier coatings on a gas turbine vane with conjugate heat transfer effects," MS Thesis, Univ. of Texas, 2013.

Stewart, W.R., "Conjugate heat transfer effects on gas turbine film cooling : including thermal fields, thermal barrier coating, and contaminant deposition," MS Thesis, Univ. of Texas, 2014.

Nomenclature

Variable	Units	Description
A	m^2	Area
Bi	-	Biot number (ht/k_{solid})
C	m	Chord length
C_d	-	Discharge coefficient
C_p	-	Pressure coefficient
c_p	J/kgK	Specific heat
D / d	mm	Hole diameter
DR	-	Density ratio (ρ_c/ρ_∞)
H	mm	Gap height
h	W/m^2K	Convective heat transfer coefficient
I	-	Momentum flux ratio ($\rho_c U_c^2/\rho_\infty U_\infty^2$)
k	W/m^2K	Thermal conductivity
L / l	mm	Length
M	-	Blowing ratio ($\rho_c U_c/\rho_\infty U_\infty$)
Ma	-	Mach number
$\dot{m}$	kg/s	Mass flowrate
Nu	-	Nusselt number (hd/k_{fluid})
P	Pa	Pressure
PIV	-	Particle Image Velocimetry
PS	-	Pressure side streamline
p	mm	Pitch length
q	W/m^2	Heat flux
Re	-	Reynolds number ($\rho_\infty U_\infty C_{ax}/\mu_\infty$)
S	m	Blade span
SS	-	Suction side streamline
s	mm or m	Surface distance or streamline length
T	°C	Temperature
TSP	-	Thermal Scaling Parameter
t	mm	Thickness
tke	J	Turbulent kinetic energy ($3/4[(u')^2+(v')^2]$)
U	m/s	Velocity
u'	m/s	Fluctuating velocity
x, y, z	mm	Global coordinates, where x is axial direction

Greek		
χ_f	-	Internal coolant warming factor, (T_∞-$T_{c,inlet}$)/ (T_∞-$T_{c,internal}$)
δ	m	Boundary layer thickness
δ*	m	Displacement thickness
μ	kg/ms	Dynamic viscosity
η	-	Adiabatic effectiveness (T_∞-T_{aw})/ (T_∞-$T_{c,exit}$)
ρ	kg/m^3	Density
τ	-	TBC effectiveness (T_∞-T_{TBC})/ (T_∞-$T_{c,internal}$)
ϕ	-	Overall effectiveness (T_∞-T_w)/ (T_∞-$T_{c,internal}$)

ϕ_f	-	Overall effectiveness for film cooling only $(T_\infty - T_{w,f})/(T_\infty - T_{c,inlet})$
ϕ_o	-	Overall effectiveness for impingement cooling only $(T_\infty - T_{w,o})/(T_\infty - T_{c,internal})$
θ	-	Momentum thickness
ω	-	Wax effectiveness $(T_\infty - T_{wax})/(T_\infty - T_{c,in})$

Subscript, Accents

$\overline{(\ )}$	-	Laterally averaged
$\overline{\overline{(\ )}}$	-	Area averaged
avg	-	Average
aw	-	Adiabatic wall surface
ax	-	Axial
c	-	Coolant or Characteristic (e.g. characteristic length)
c,in	-	Coolant upstream of the impingement plate
c,inlet	-	Coolant at the inlet to the film cooling hole
dep	-	Deposition
f	-	With film cooling only, no impingement
i	-	Internal
∞	-	Mainstream or external
∞*,in*		Mainstream conditions at the cascade inlet
loc	-	Local
meas	-	Measured
n		Normal component
o	-	With impingement only, no film cooling
p		Particle
s	-	Static
str		Streamwise component
TBC	-	TBC surface or with TBC
tot	-	Total
w	-	Wall

Tables

Table 1.1. Flow Conditions and Blade Geometry [PSU]

		Boundary Layer Parameters $2.85C_{ax}$ Upstream of Blade 4 (Lynch et al., 2011b)	
Scale factor	8.6		
C_{ax}	0.218 m		
p/C_{ax}	0.826		
S/C_{ax}	2.50	δ/S	0.061
Inlet Re	$1.22x10^5$	δ^*/S	0.0062
Exit Re	$1.98x10^5$	θ/S	0.0046
Inlet U_∞	10.5 m/s	Boundary layer shape factor	1.34
Inlet, exit flow angles	35°, 60°		
Inlet, exit Ma	0.029, 0.047	u'/U	0.060

Table 2.1. Engine Endwall Parameters and the Conducting Endwall Model [PSU]

	Engine	Model - Flat	Model - Contoured
M_{avg}	1.0 – 2.0 (2011)	0.6, 1.0, 2.0	0.6, 1.0, 2.0
H/D	3	3	0.6-3.4
h_i, W/m^2-K	2839 (2011)	22-57	21-54
h_∞, W/m^2-K	2839 (2011)	25-55	20-50
k_w, W/m-K	22 (2011)	0.99-1.06	0.99-1.06
t, mm	2.0 (2011)	12.7	12.7
h_∞/h_i	1.0	0.5-2.3	0.4-2.3
Bi	0.27	0.3-0.65	0.25-0.7
k_{TBC}, W/m-K	0.8-1.7	0.061	0.061
t_{TBC}, mm	0.1-0.7	1.92	1.92
$R_{TBC}/R_w = \frac{t_{TBC}k_w}{t_w k_{TBC}}$	0.6-9.3	2.5	2.5
Stk_D	0.004–40 (Bons et al., 2007)	median: 6 (Lawson & Thole, 2012a)	
Stk_{Cax}	8x10-5–0.7 (Bons et al., 2007)	median: 0.1 (Lawson & Thole, 2012a)	
TSP	$1x10^{-4}$–1.2 (Bons et al., 2007; Q. Wang et al., 2008; Li et al., 2007; Dennis et al., 2007)	median: 0.3 (Lawson et al., 2013)	

Table 2.2. Comparison of vane and TBC properties for engine and wind tunnel models.

Parameter	Real Turbine	Model Turbine		Units
		Original TBC	Thinner TBC	
Vane Thickness	1.3-3	12.7		mm
TBC Thickness	0.14 – 0.72	4.2	2.5	mm
Vane Conductivity	20	1.02		W/m-K
TBC Conductivity	0.83 – 1.7	0.065		W/m-K
Heat Transfer Coeff.	1500 – 5000	25 – 90		W/m^2-K
TBC/Vane Thickness	0.05 – 0.5	0.33	0.20	-
Vane/TBC Conductivity	12 – 24	15.7		-
Vane Bi	0.3 – 0.6	0.3 – 1.1		-

Table 2.3. UT Vane model and test operational parameters

Parameter	Value
Chord Length (C)	531 mm
Vane Span (*H*)	549 mm
Vane Pitch (*P*)	457 mm
Turning Angle	72 degrees
Mainstream Temperature ($T_{e,\infty}$)	301 or 305 K
Mainstream Velocity (U_∞)	5.8 m/s
Density Ratio (DR)	1.2
Inlet Reynolds Number (Re_{inlet})	190,000
Turbulence Level (*Tu*)	20 %
Integral Length Scale (Λ_f)	40 mm

Table 4.1. Distance from the Endwall of the Center of the Low Velocity Region, Z_p/S [PSU]

	Plane A	Plane B	Plane C
No Film Cooling	0.13	0.13	0.16
M_{avg} = 1.0	0.15	0.15	0.16
M_{avg} = 2.0	0.16	0.16	0.16

Table 5.1. Measured Improvement in Overall Effectiveness Due to an Increase in Blowing Ratio and Due to the Addition of TBC [PSU]

ΔM	$\overline{\overline{\Delta\phi}}_M$	M_{avg}	$\overline{\overline{\Delta\phi}}_{TBC} = \overline{\overline{\phi}}_{TBC} - \overline{\overline{\phi}}$
0.6 – 1.0	0.05	0.6	0.13
		1.0	0.14
1.0 – 2.0	0.04	2.0	0.17

Figures

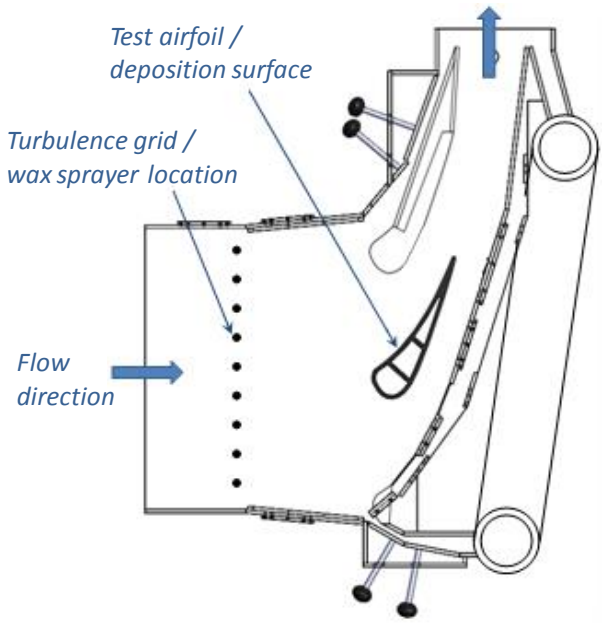

Figure 1.1. Schematic of the vane cascade test section (UT).

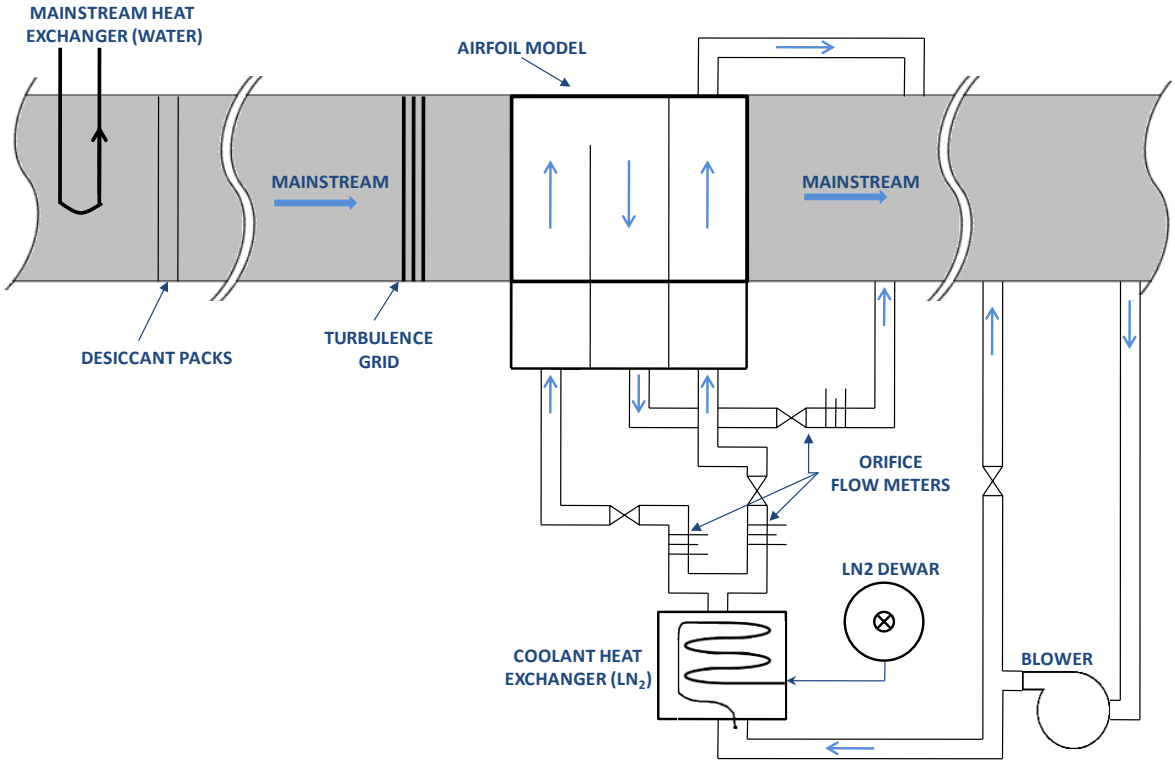

Figure 1.2. Schematic of coolant air supply to the vane model (UT).

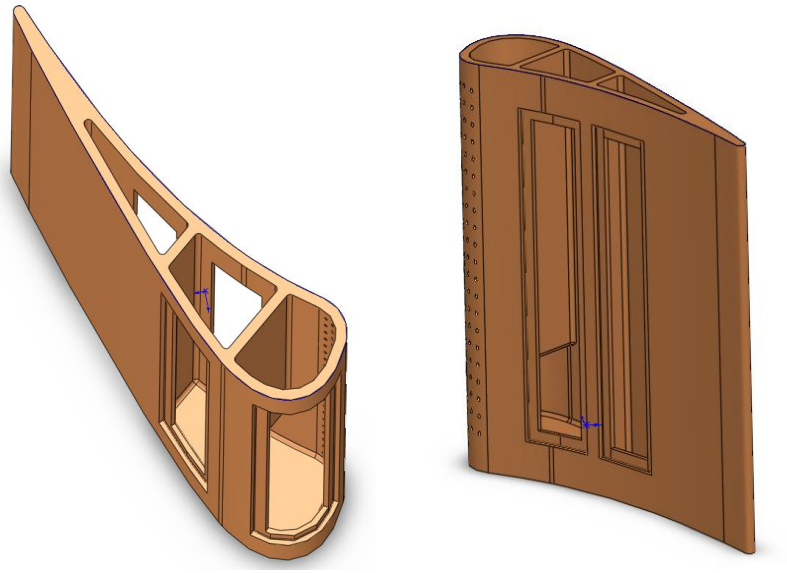

Figure 1.3. Schematic of turbine vane models, with hatches removed, showing internal passages.

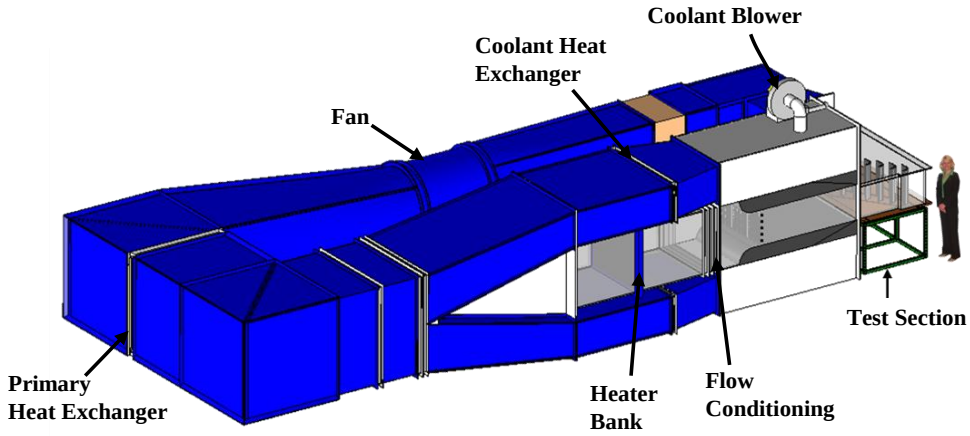

Figure 1.4. Illustration of wind tunnel facility at PSU.

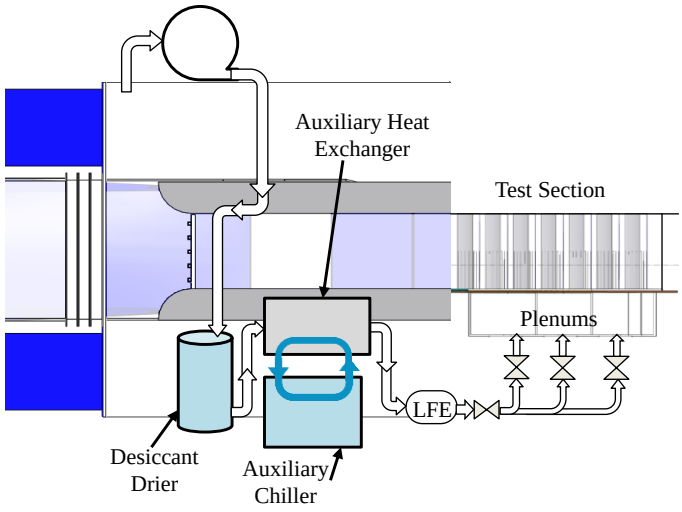

Figure 1.5. Diagram of coolant loop with auxiliary cooling capability and the inlet flow development section, side view.

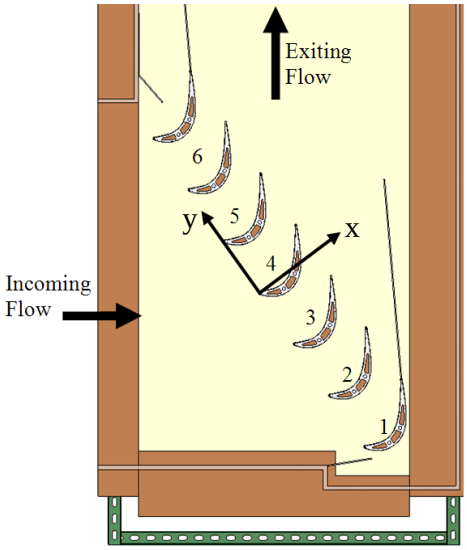

Figure 1.6. Top view schematic of the Pack-B linear blade cascade.

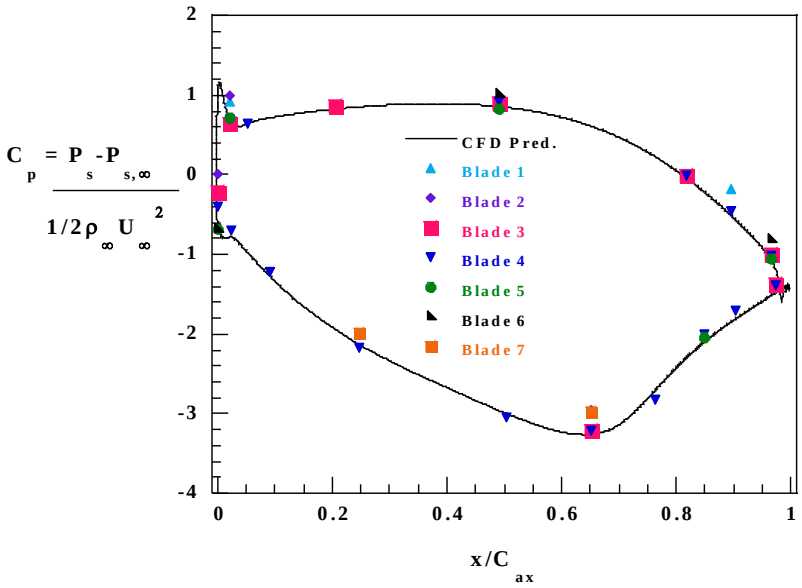

Figure 1.7. Pack-B cascade static pressure distribution at the blade midspan compared to a CFD prediction (Lynch et al., 2011a)**.**

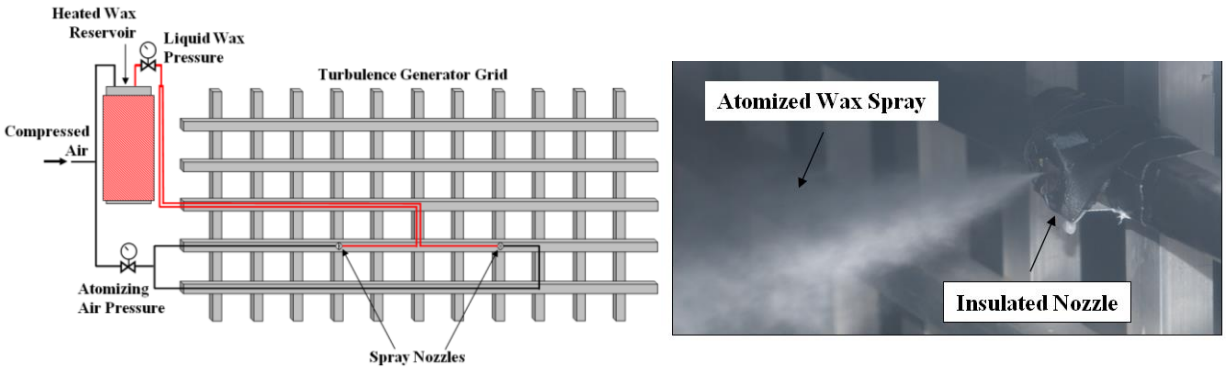

Figure 1.8. Two-nozzle wax injection system located in the turbulence grid.

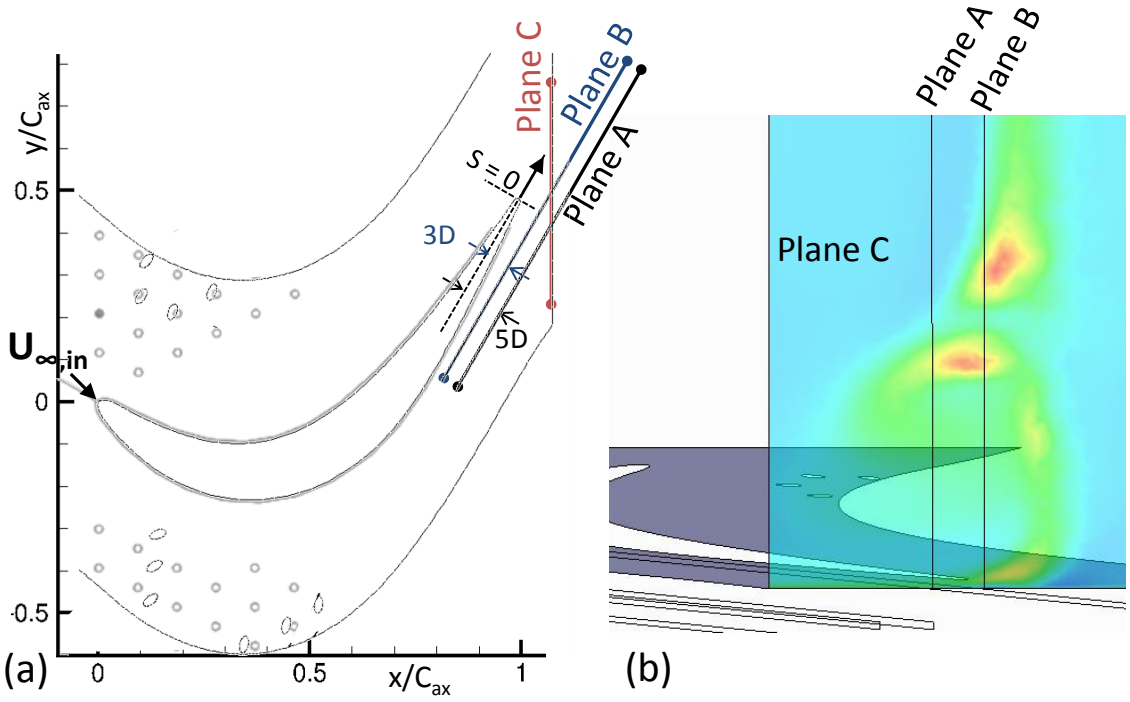

Figure 1.9. Planes measured with PIV (a) shown from above and (b) shown from the view of Plane C overlaid with flat endwall CFD tke contours for M_{avg} = 2.0.

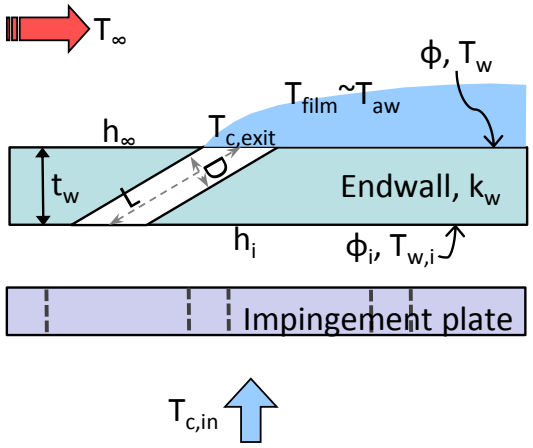

Figure 2.1. Configuration of a conjugate wall with impingement and film cooling.

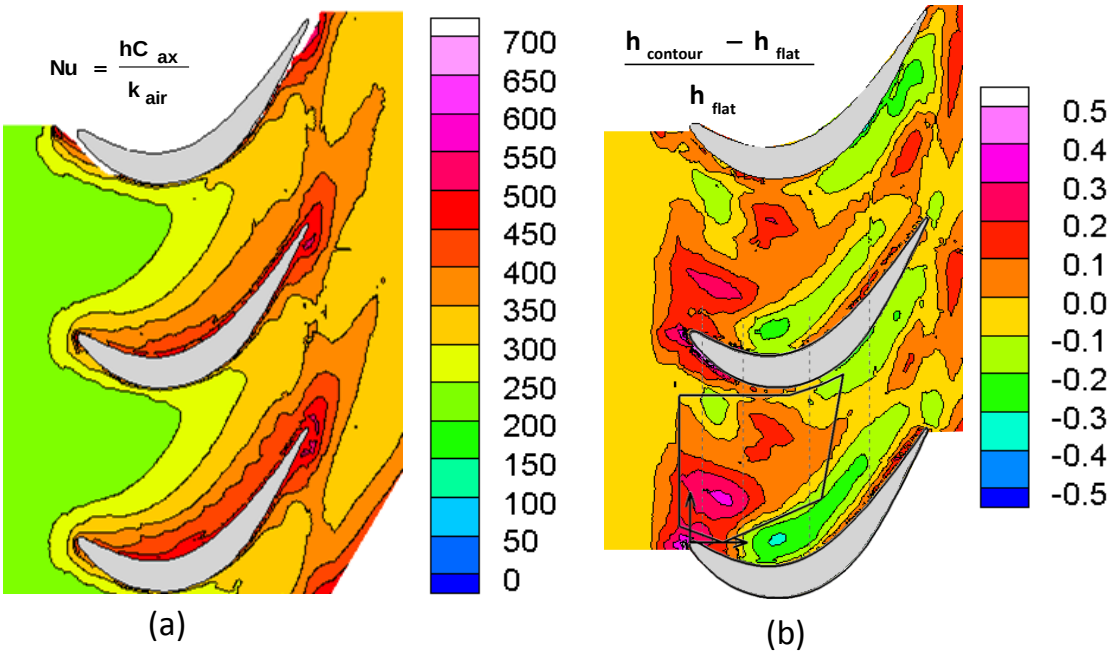

Figure 2.2. **Heat transfer measurements for the Pack-B cascade at Re_{exit} of $2x10^5$ (Lynch et al., 2011b), (a) Nusselt number contours for the flat endwall, (b) heat transfer augmentation contours due to endwall contouring.**

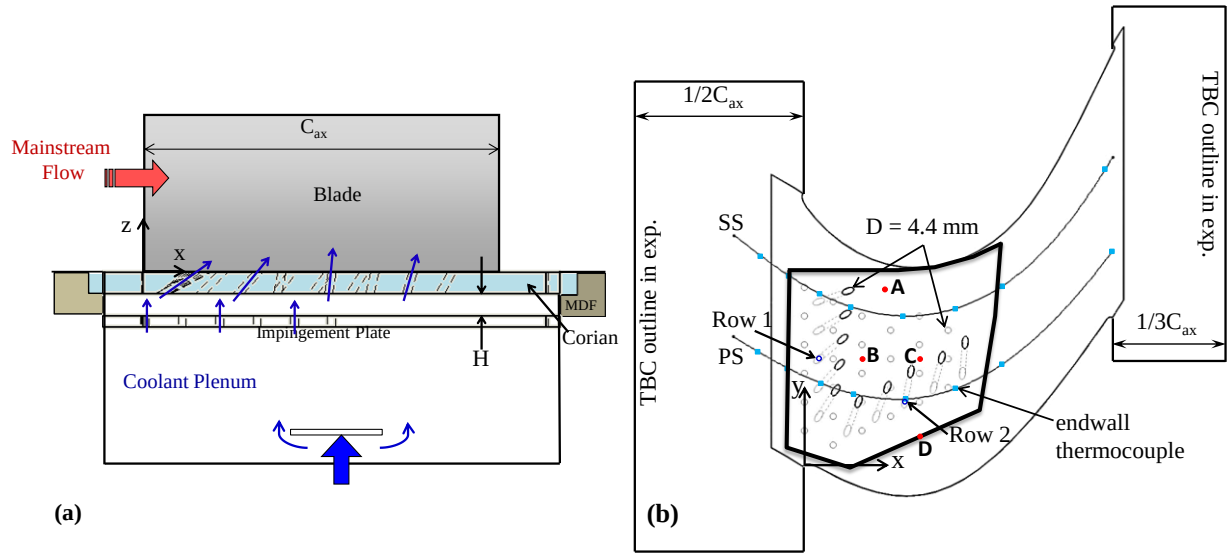

Figure 2.3. **Schematic of internal and external cooling scheme for the flat endwall from the side view (a) and the top view showing TBC outline, internal surface thermocouples (red), and TBC interface surface thermocouples (blue) (b) [PSU].**

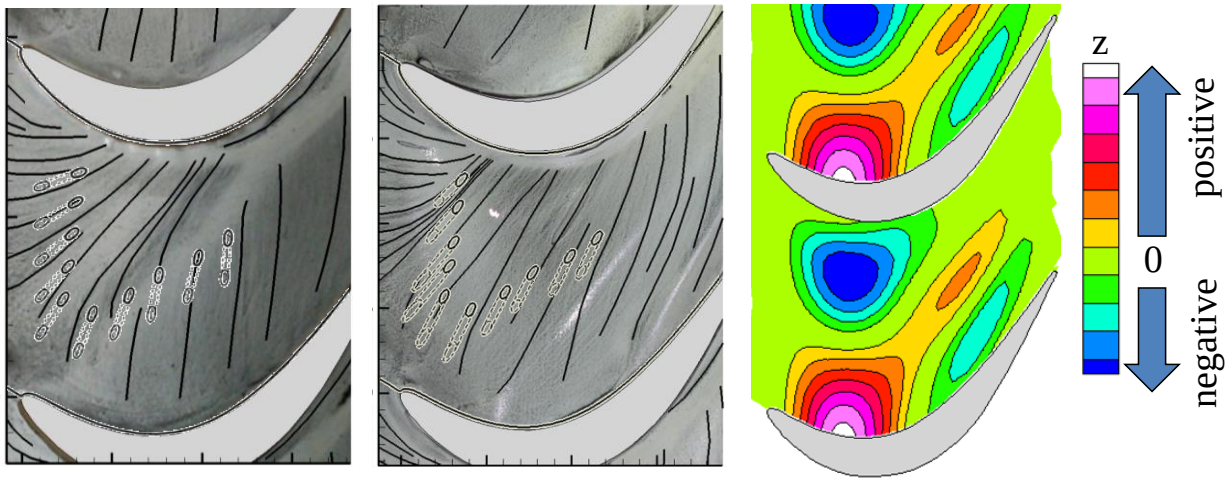

Figure 2.4. **Comparison of oil flow visualization of endwall streaklines** (Lynch et al., 2011b) **with film cooling hole inlet and outlet locations for the (a) flat and (b) contoured endwalls, and qualitative representation of the contoured endwall height variation [PSU].**

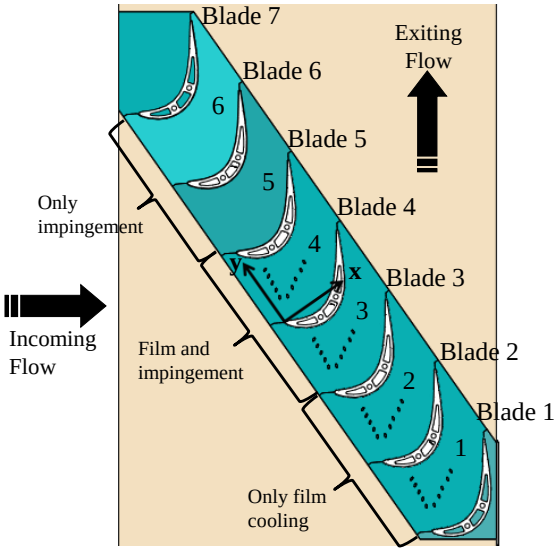

Figure 2.5. **Top view schematic of the passages 1-6 and the types of cooling in each [PSU].**

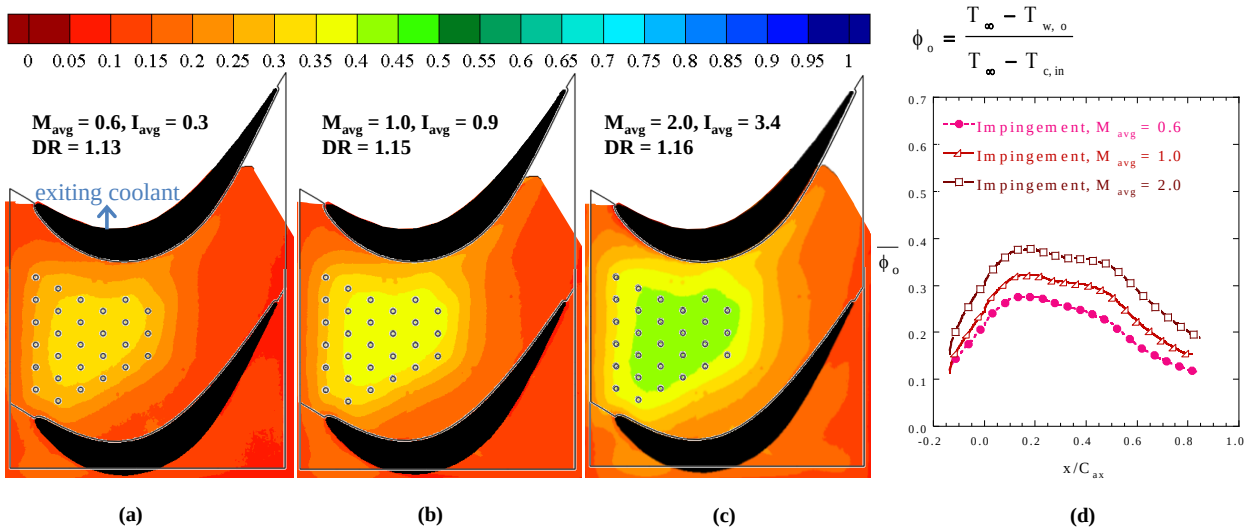

Figure 2.6. **Contours of ϕ_o for blowing ratios: (a) M_{avg} = 0.6, (b) M_{avg} = 1.0, (c) M_{avg} = 2.0, with 90° impingement holes and plenum boundaries overlaid, and (d) pitchwise laterally averaged ϕ_o plotted as a function of axial distance [PSU].**

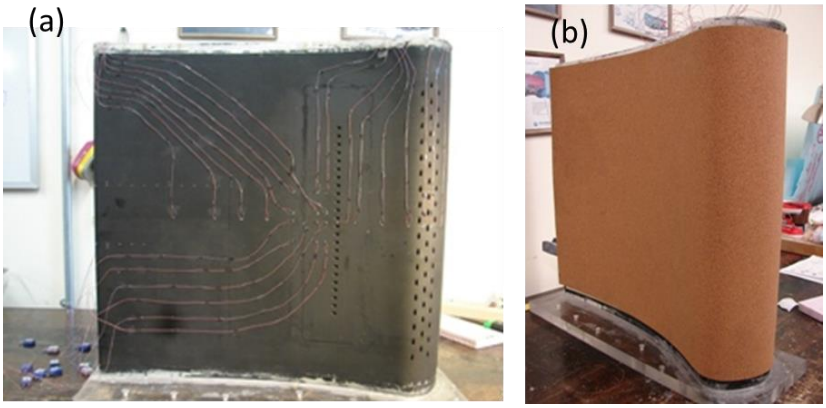

Figure 2.7. Images showing (a) thermocouples on the pressure side of vane and (b) model with simulated TBC cork layer attached.

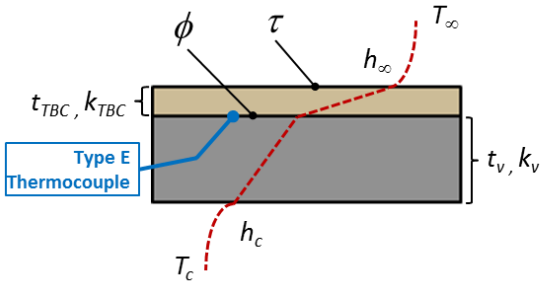

Figure 2.8: Vane wall cross-section with TBC and relative location of measurements of interest.

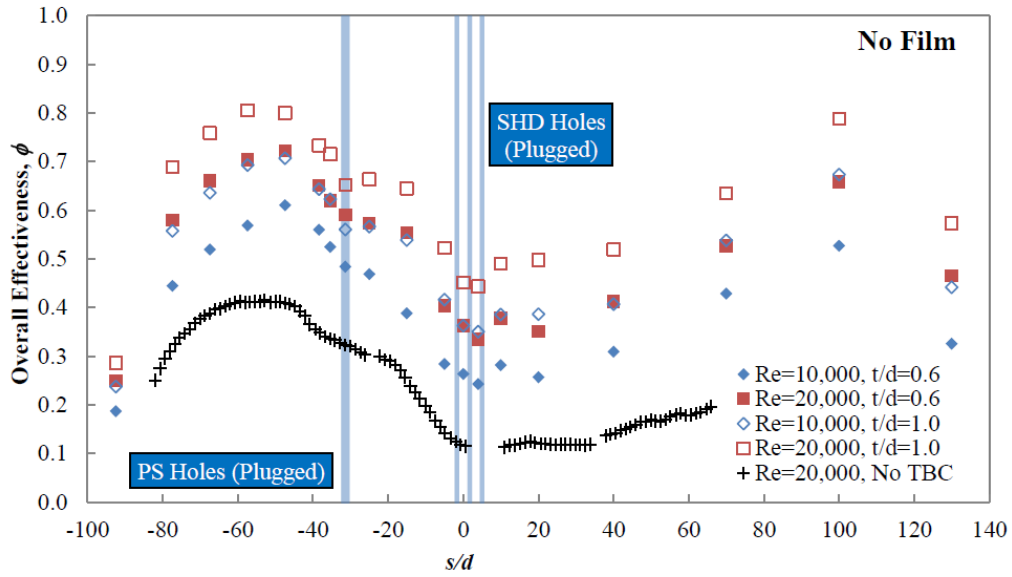

Figure 2.9. Effect of TBC thickness on ϕ with Tu=20%, DR=1.2, M=0 and Re_{avg}=20,000.

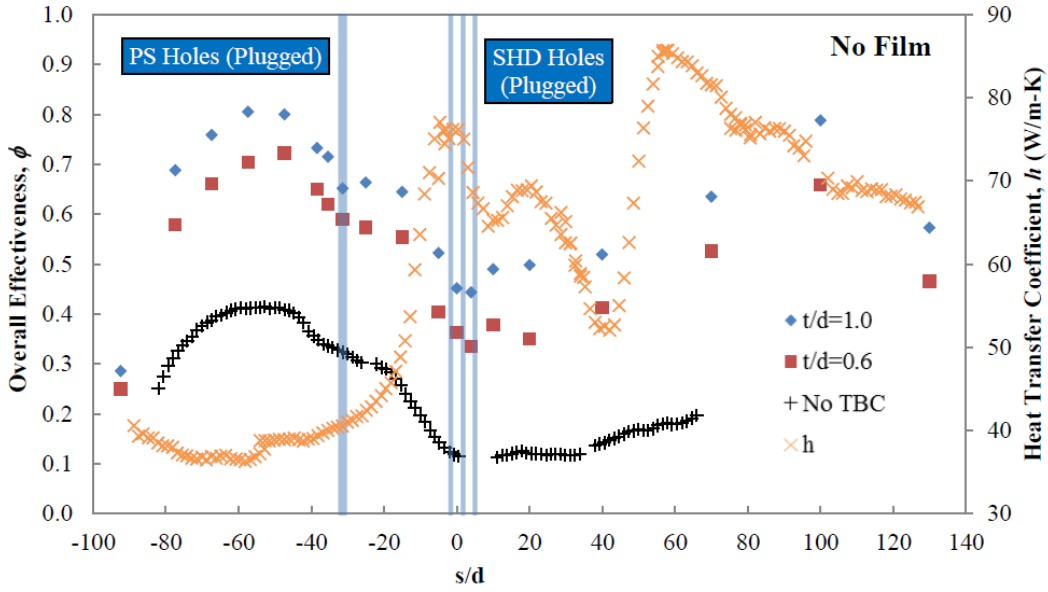

Figure 2.10. Comparison of ϕ distributioins with corresponding heat transfer coefficient distribution for Tu=20%, M=0 and Re_{avg}=20,000.

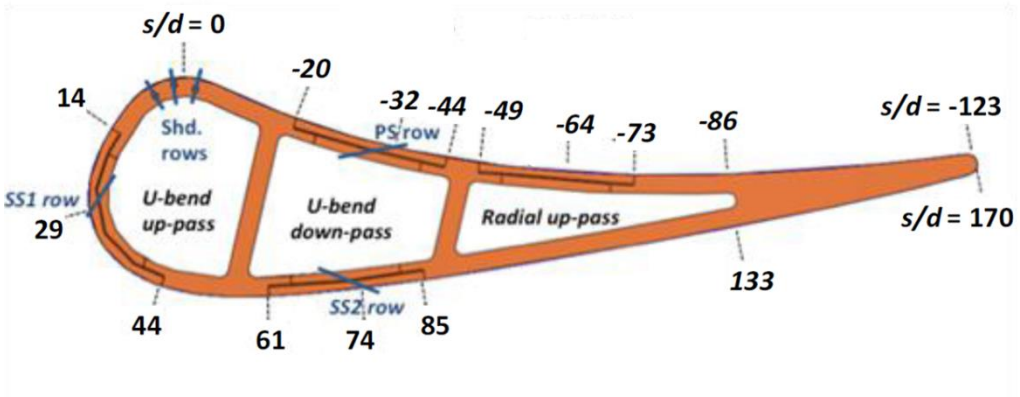

Figure 2.11. Schematic of the turbine vane model showing the internal coolant channels.

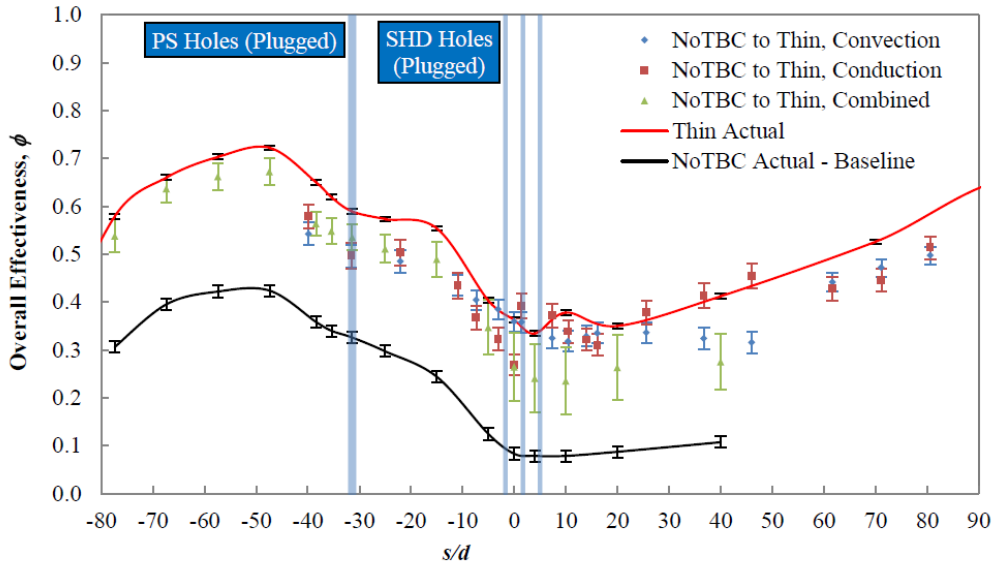

Figure 2.12. Comparison of three different ϕ prediction methods that predict the performance of the thin TBC from the No TBC case.

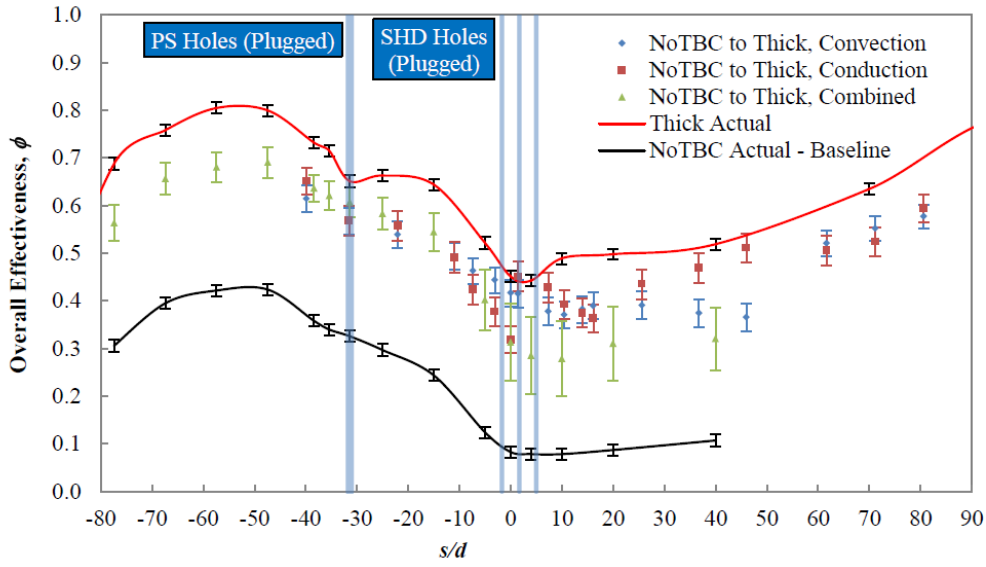

Figure 2.13. Comparison of three different ϕ prediction methods that predict the performance of the thick TBC from the No TBC case.

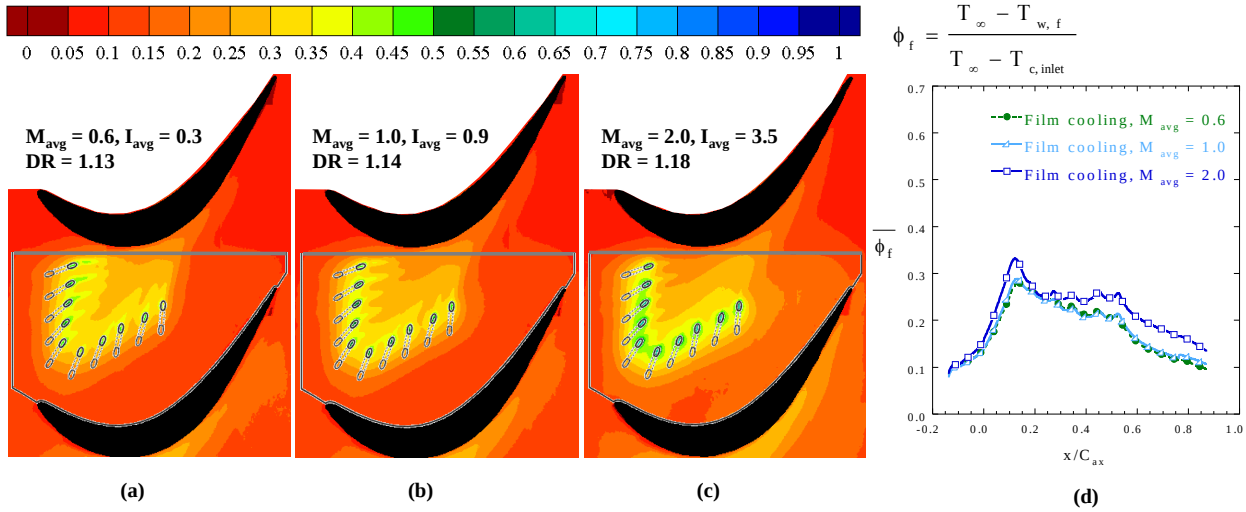

Figure 3.1. Contours of ϕ_f for blowing ratios: (a) M_{avg} = 0.6, (b) M_{avg} = 1.0, (c) M_{avg} = 2.0, with 30° inclined holes and plenum boundaries overlaid, and (d) pitchwise laterally averaged ϕ_f plotted as a function of axial distance [PSU].

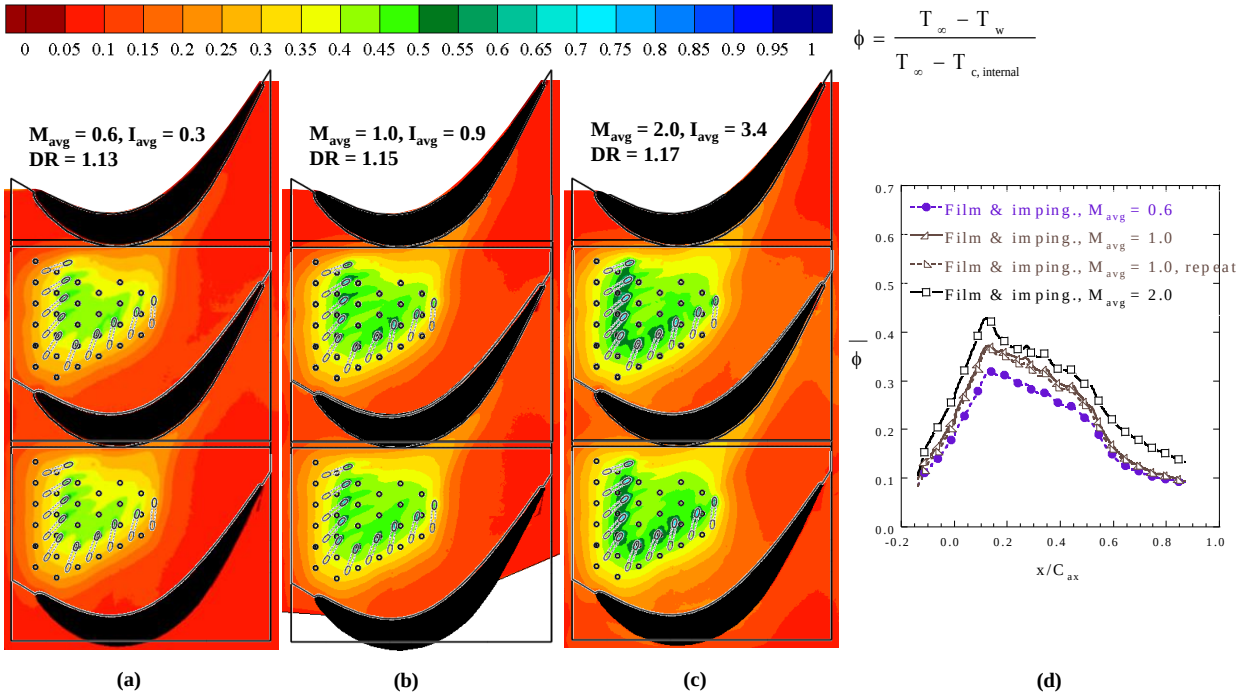

Figure 3.2. **Contours of ϕ for: (a) M_{avg} = 0.6, measured (b) M_{avg} = 1.0, measured (c) M_{avg} = 1.0, predicted, (d) M_{avg} = 2.0, measured, and (e) M_{avg} = 2.0, predicted, with 30° inclined film holes, 90° impingement holes, and plenum boundaries overlaid [PSU].**

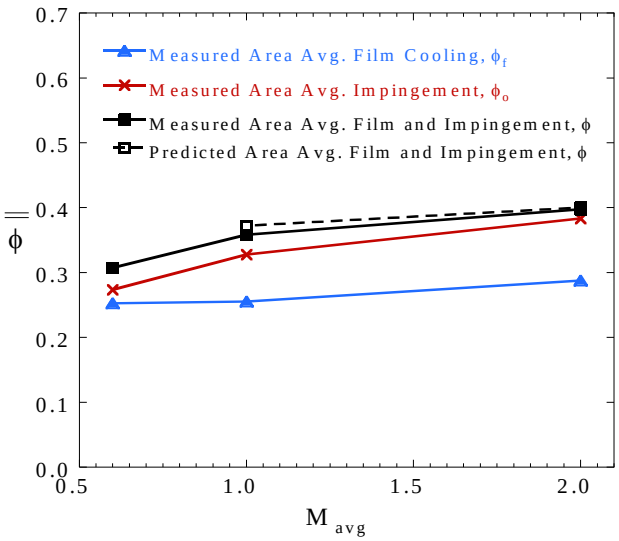

Figure 3.3. **Area averaged ϕ (using area outlined in Figure 1.2b) plotted as a function of blowing ratio for all three cooling configurations [PSU].**

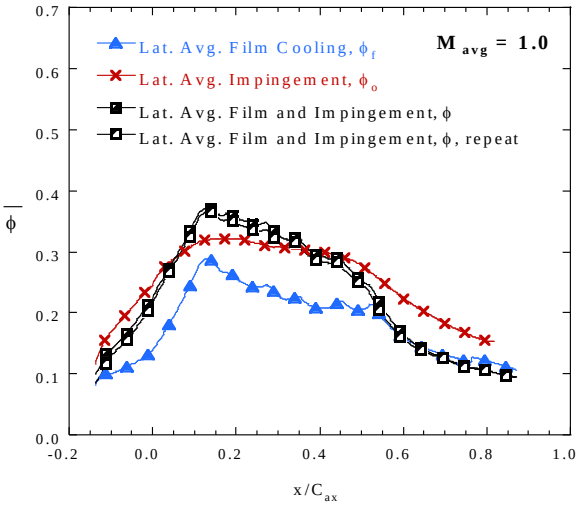

Figure 3.4. Pitchwise laterally averaged ϕ plotted as a function of axial distance for the three cooling configurations at M_{avg} = 1.0 [PSU].

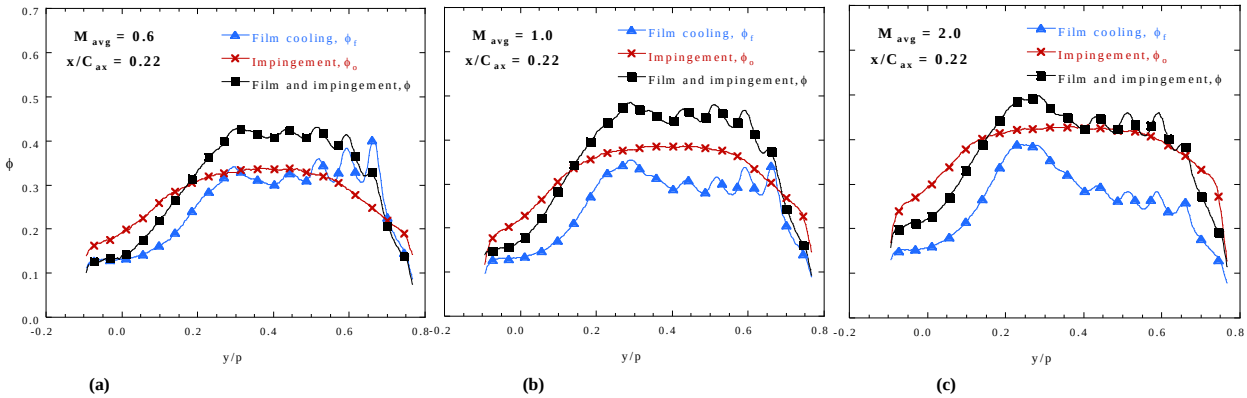

Figure 3.5. Overall effectiveness of all cooling configurations plotted as a function of y/p at x/C_{ax} = 0.22 for (a) M_{avg} = 0.6, (b) M_{avg} = 1.0, and (c) M_{avg} = 2.0 [PSU].

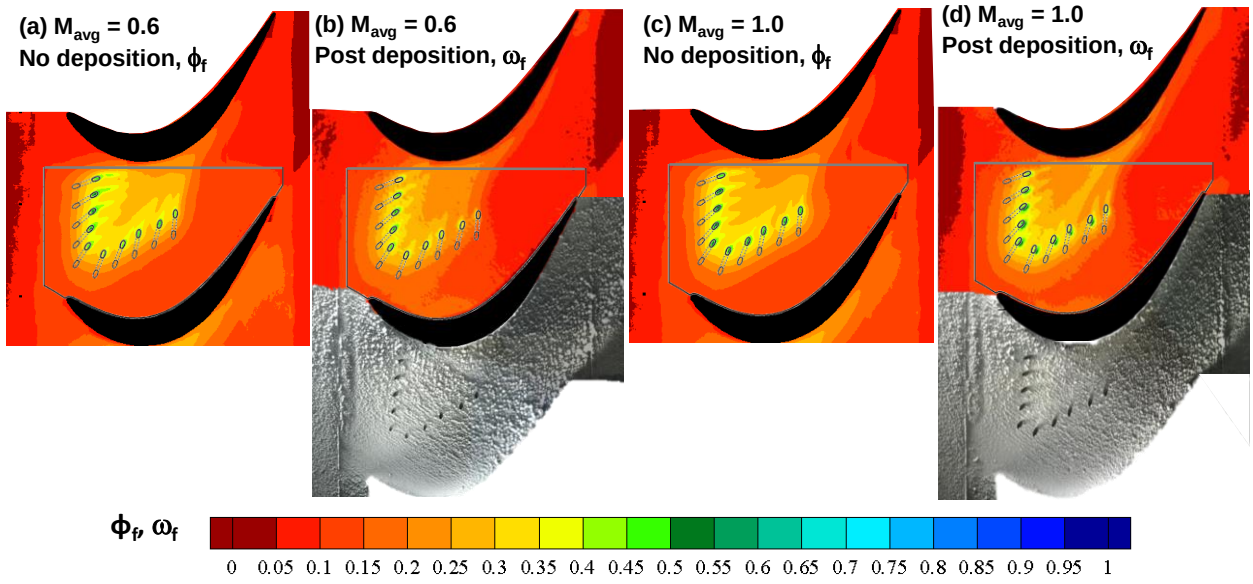

Figure 3.6. **Film cooling only contours of (a) ϕ_f without deposition for M_{avg} = 0.6, (b) wax effectiveness, ω_f, and deposition photographs for M_{avg} = 0.6, (c) ϕ_f for M_{avg} = 1.0, and (d) ω_f, and deposition photographs for M_{avg} = 1.0 [PSU].**

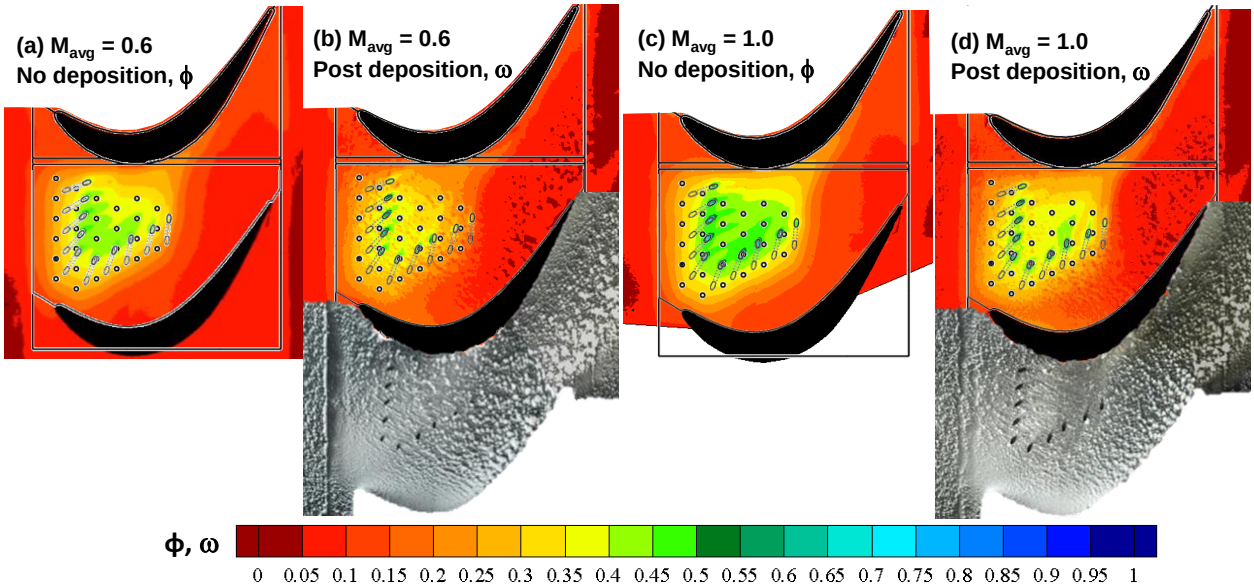

Figure 3.7. **Film and impingement cooling contours (a) ϕ without deposition for M_{avg} = 0.6, (b) wax effectiveness, ω, and deposition photographs for M_{avg} = 0.6, (c) ϕ for M_{avg} = 1.0, and (d) ω, and deposition photographs for M_{avg} = 1.0 [PSU].**

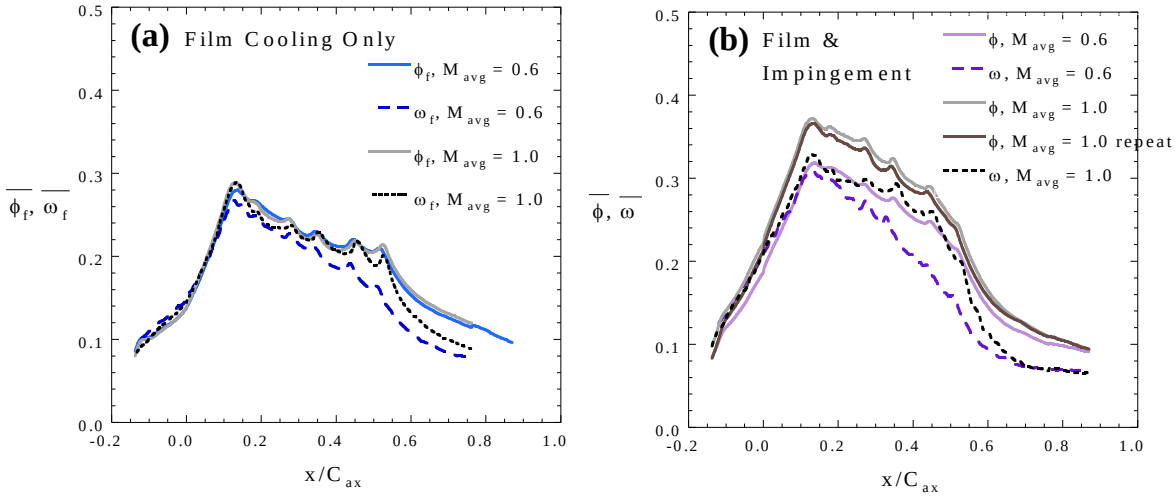

Figure 3.8. **Laterally averaged overall effectiveness without deposition, ϕ, and wax effectiveness, ω, across the passage for M_{avg} = 0.6 and 1.0 for (a) film cooling only, and (b) film and impingement [PSU].**

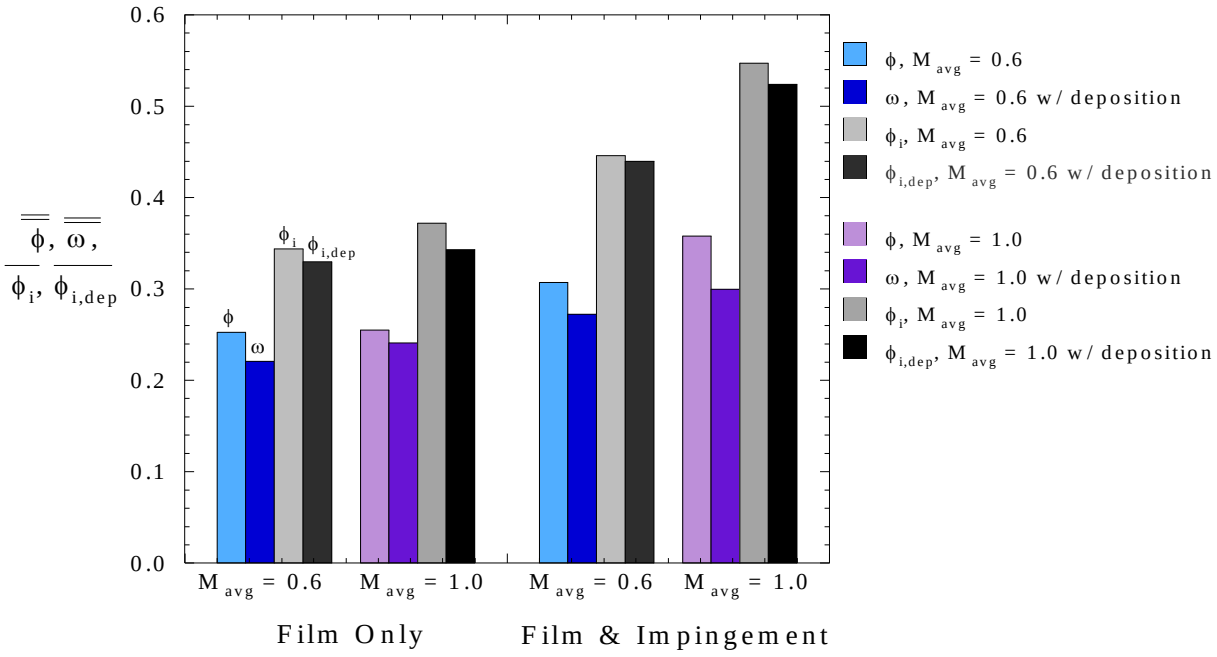

Figure 3.9. **Area average overall effectiveness without deposition, ϕ, area average wax effectiveness ω, and average internal effectiveness with and without deposition, ϕ_i, $\phi_{i,dep}$, for film cooling only and combined film and impingement at different blowing ratios [PSU].**

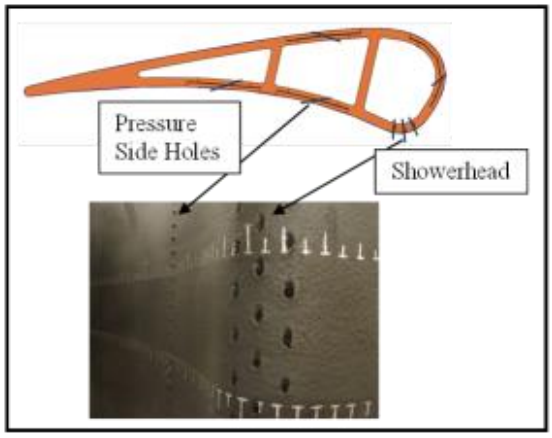

3.10. Schematic and photograph of showerhead and pressure side of vane with TBC.

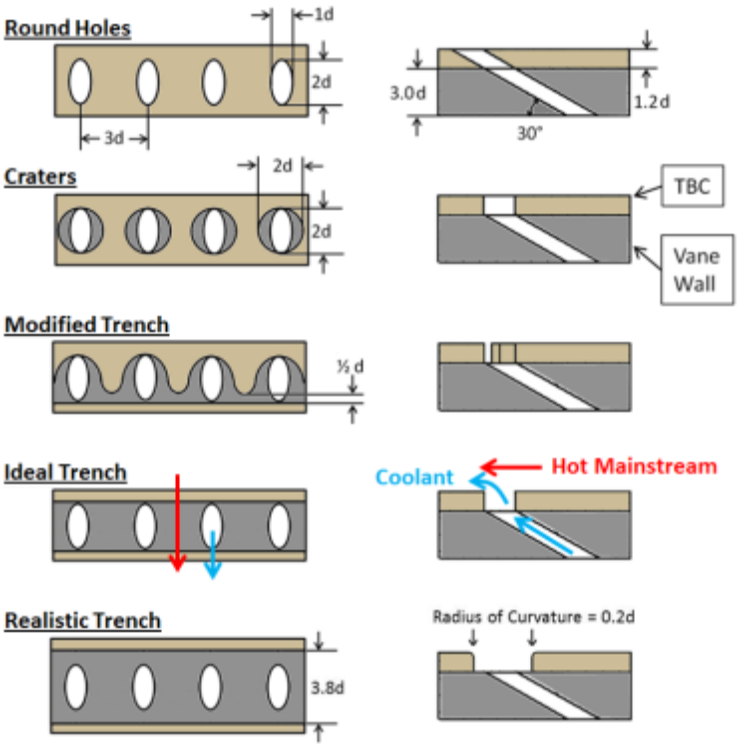

Figure 3.11. Film cooling configurations with overlying layer of TBC.

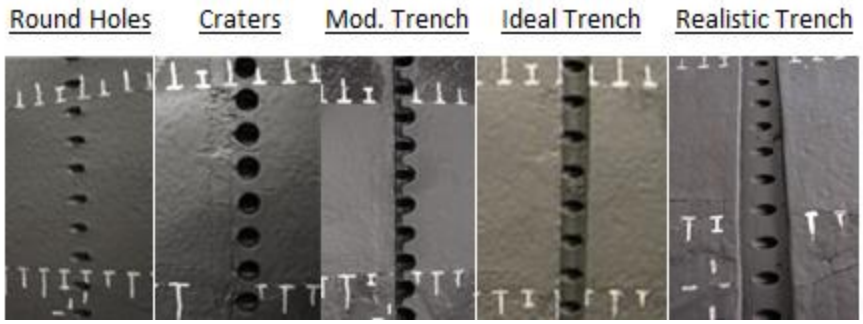

Figure 3.12. Images of film cooling geometries on pressure side of vane with TBC.

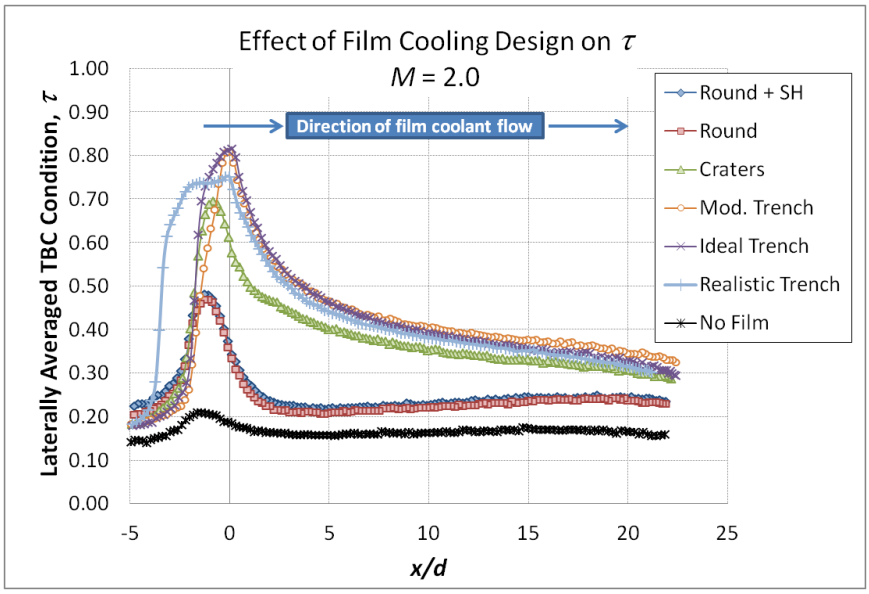

Figure 3.13. Comparison of film cooling configurations in terms of laterally averaged τ distributions for M = 2.0 and TBC thickness t/d = 1.2.

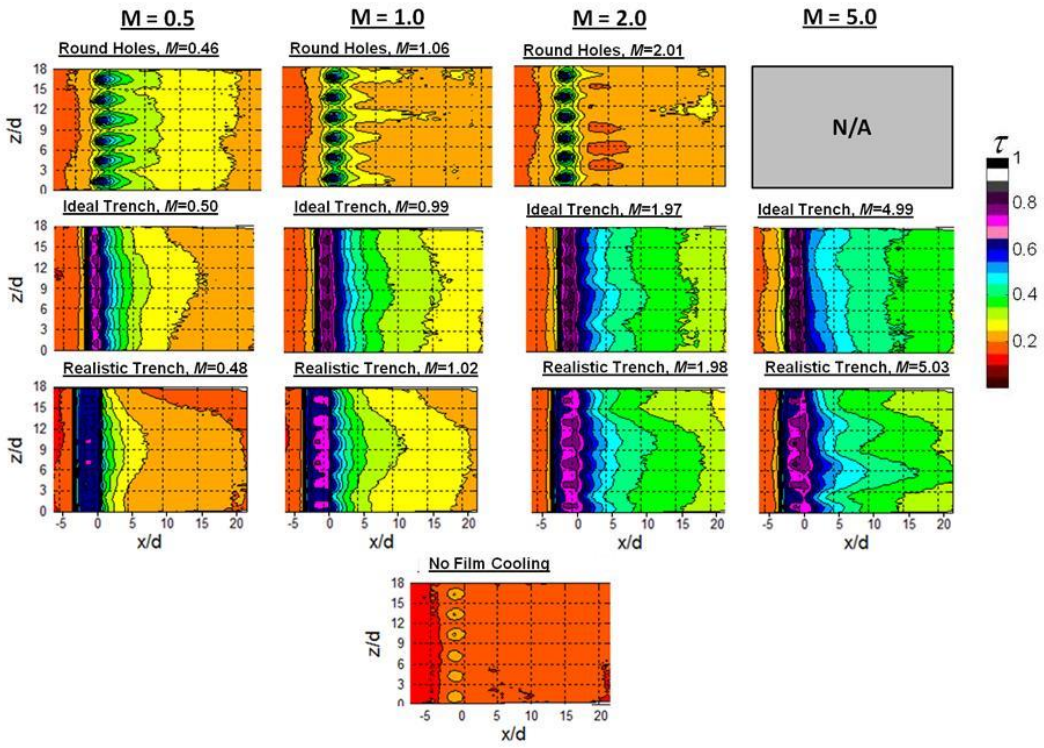

Figure 3.14. Contours of τ distributions for round, ideal trench, and realistic trench configurations with TBC thickness *t/d* = 1.2.

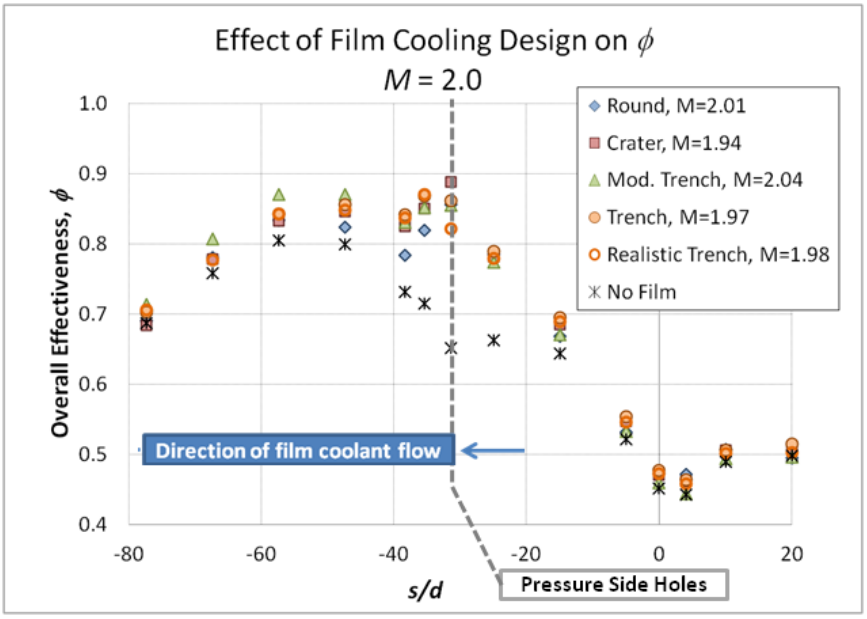

Figure 3.15. Comparison of film cooling configurations in terms of laterally averaged ϕ distributions for *M* = 2.0 and TBC thickness *t/d* = 1.2.

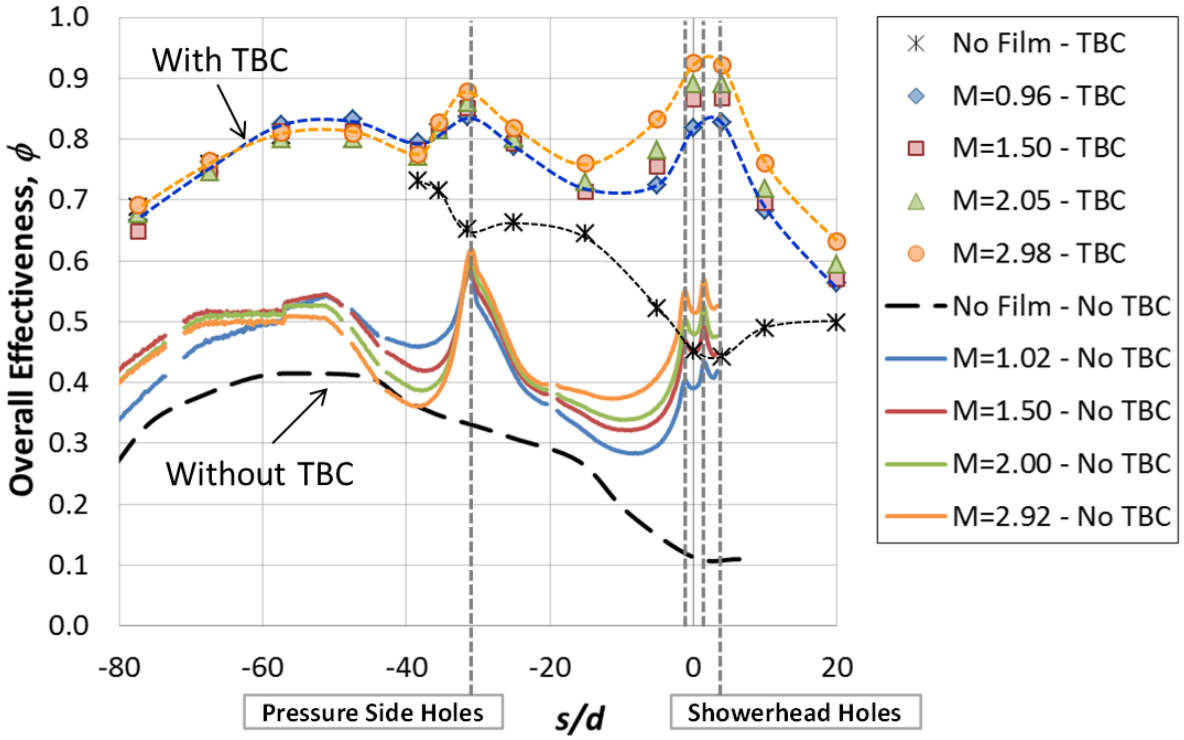

Figure 3.16. Comparison of ϕ with and without TBC for round holes with an active showerhead.

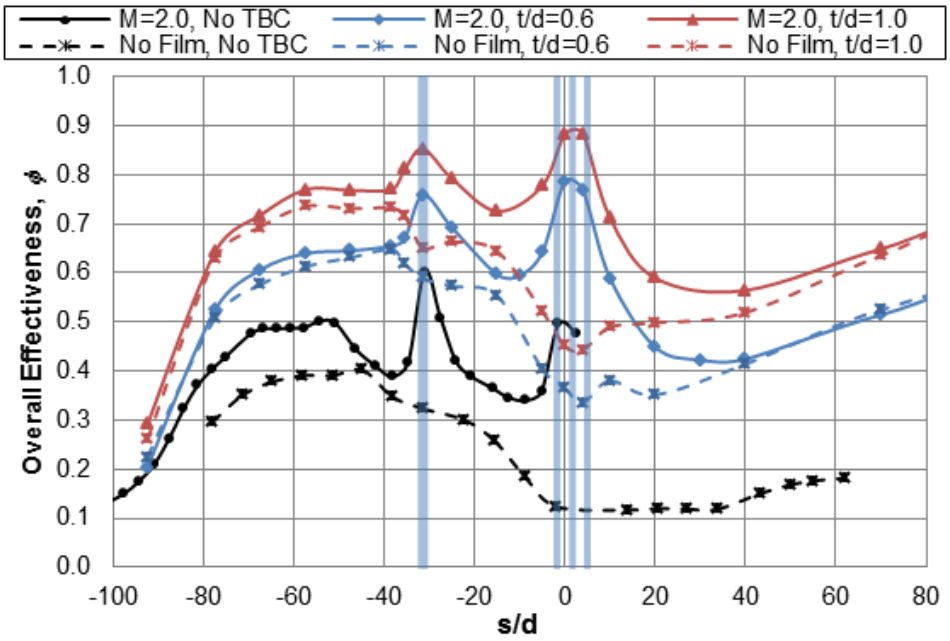

Figure 3.17. Comparison of performances of thick and thin TBC for round holes with an active showerhead.

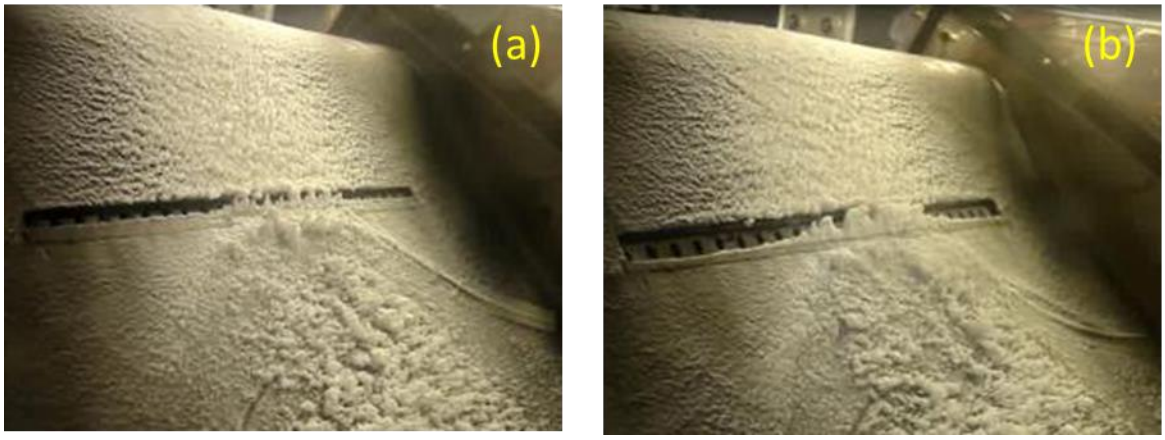

Figure 3.18. Images of deposition on the (a) ideal and (b) realistic trenches immediately following the conclusion of deposition.

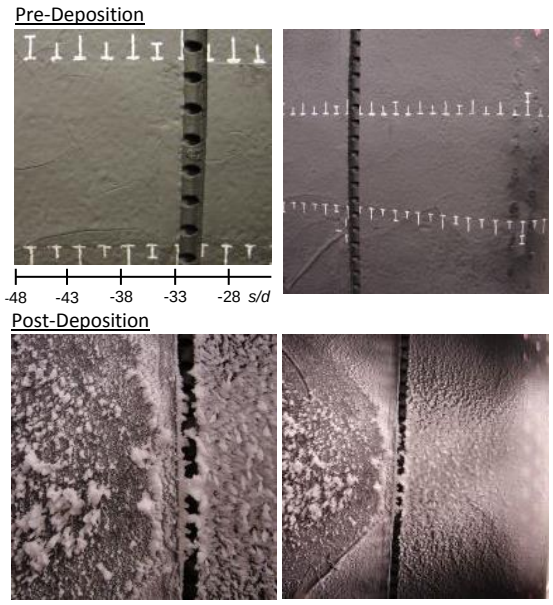

Figure 3.19. Photographs before and after deposition for an ideal trench at *M*=2.0.

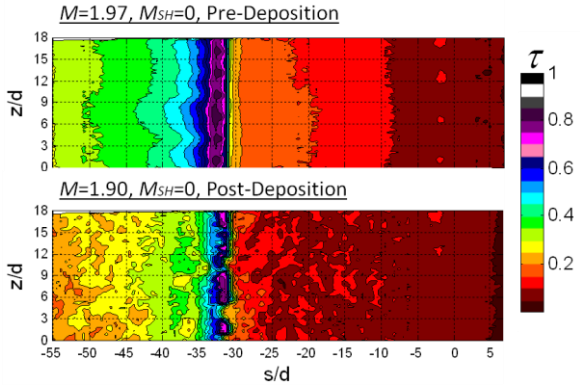

Figure 3.20. Contour plots of τ for an ideal trench at *M*=2.0 before and after deposition.

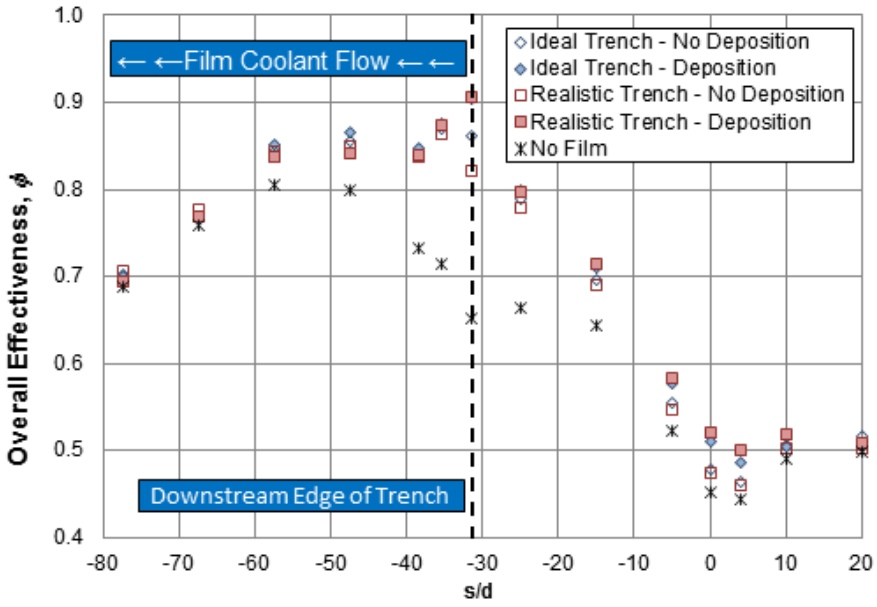

Figure 3.21. Effect of deposition on ϕ for varying film cooling designs at M=2.0.

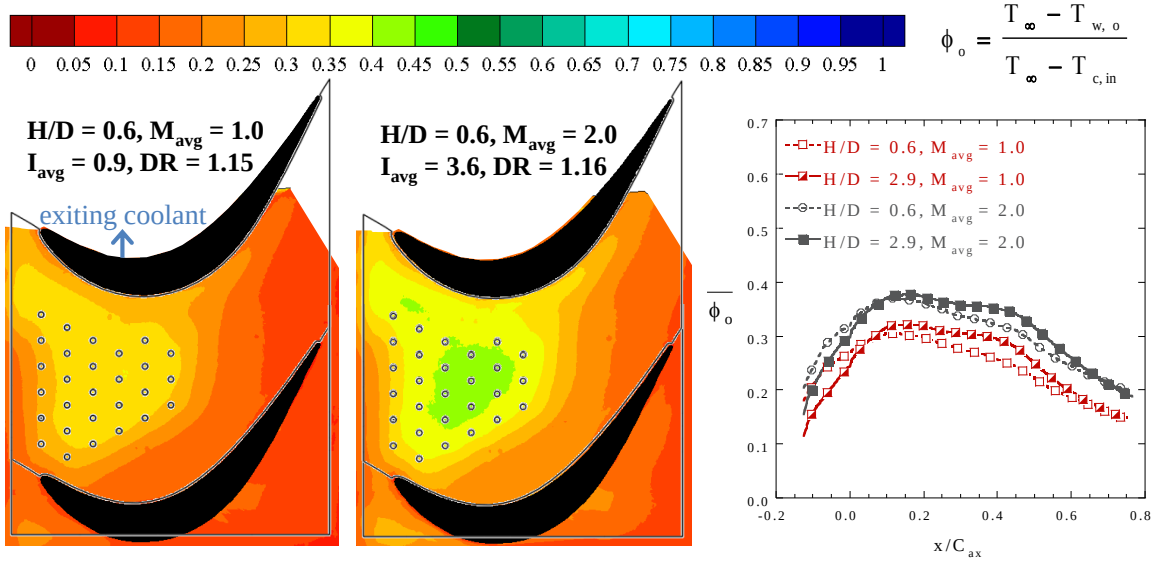

(a) **(b)** **(c)**

Figure 4.1. **Contours of flat endwall measured ϕ_o at H/D = 0.6 for blowing ratios: (a) M_{avg} = 1.0, (b) M_{avg} = 2.0, with 90° impingement holes and plenum boundaries overlaid, and (c) pitchwise laterally averaged ϕ_o for H/D = 0.6 and 2.9 plotted as a function of axial distance [PSU].**

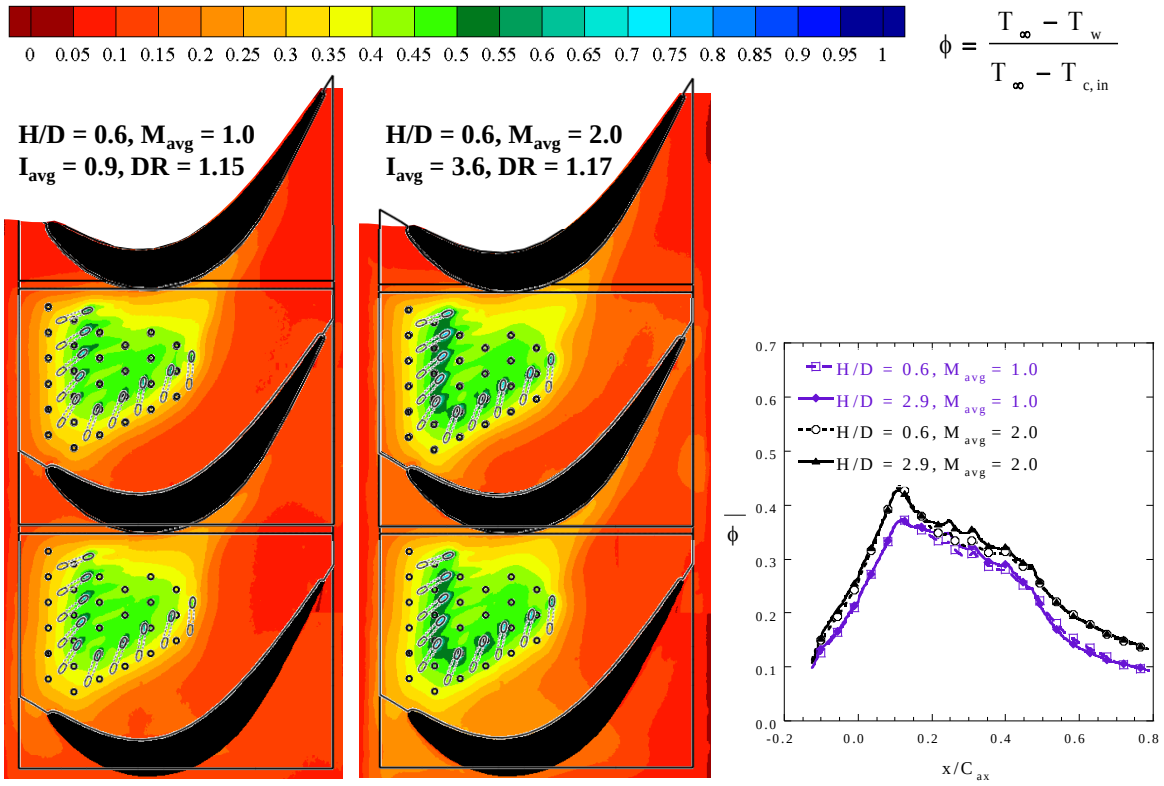

(a) **(b)** **(c)**

Figure 4.2. **Contours of flat endwall measured ϕ at *H/D* = 0.6 for blowing ratios: (a) M_{avg} = 1.0, (b) M_{avg} = 2.0, with 30° inclined film holes, 90° impingement holes, and plenum boundaries overlaid, and (c) pitchwise laterally averaged ϕ for *H/D* = 0.6 and 2.9 plotted as a function of axial distance [PSU].**

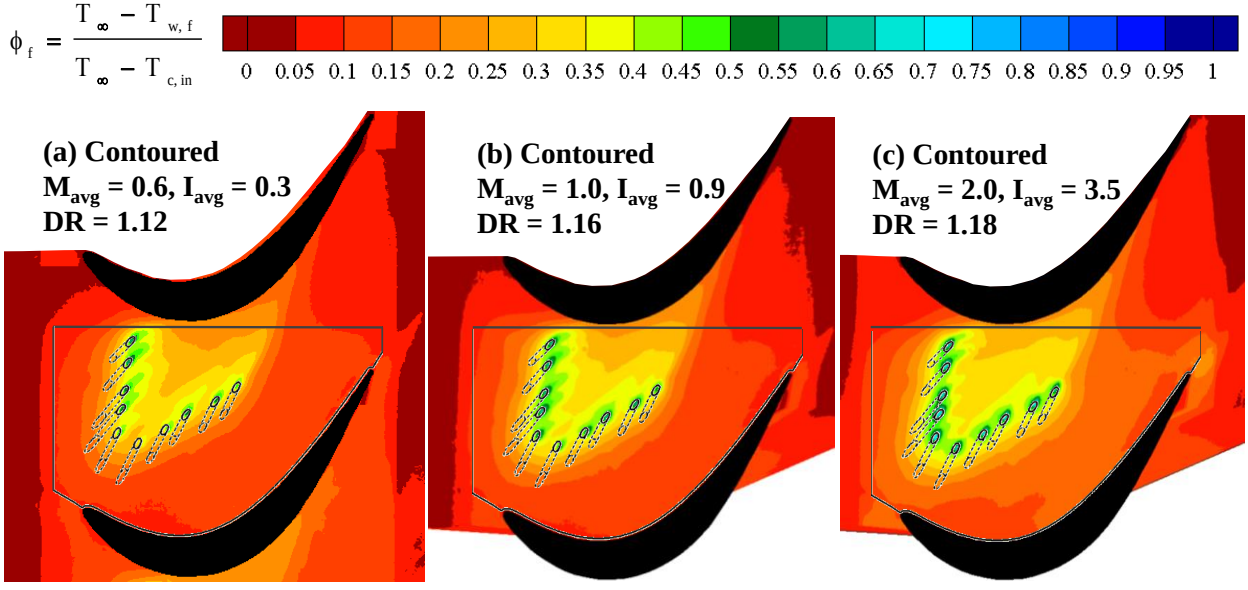

Figure 4.3. **Contoured enwall measured ϕ_f, film cooling only, for the contoured endwall for blowing ratios: (a) M_{avg} = 0.6, (b) M_{avg} = 1.0 and (c) M_{avg} = 2.0 [PSU].**

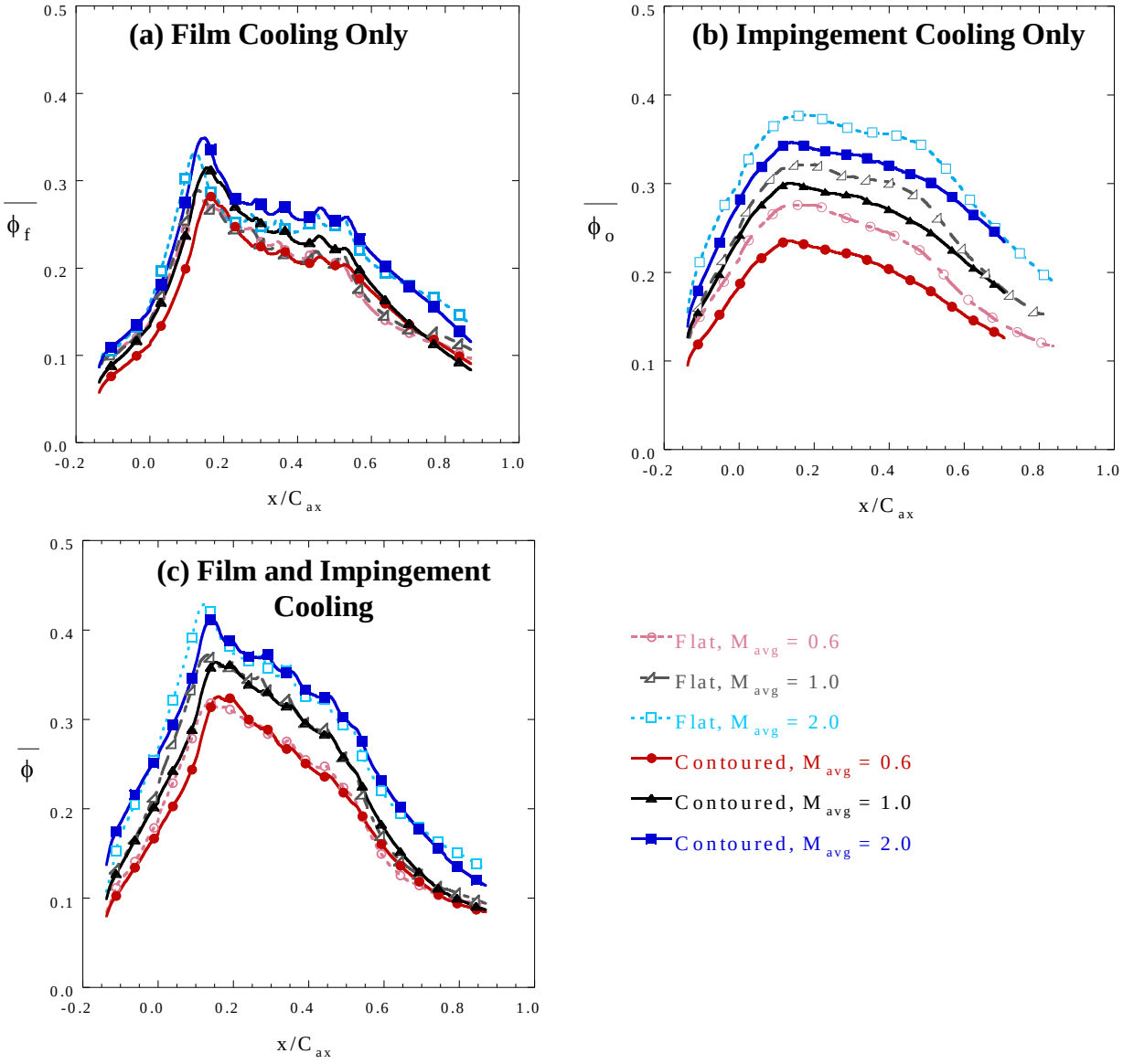

Figure 4.4. **Comparison of the pitchwise laterally averaged measured ϕ for the flat and contoured endwalls plotted as a function of x/C_{ax} for (a) film cooling only, (b) impingement cooling only, and (c) impingement plus film cooling [PSU].**

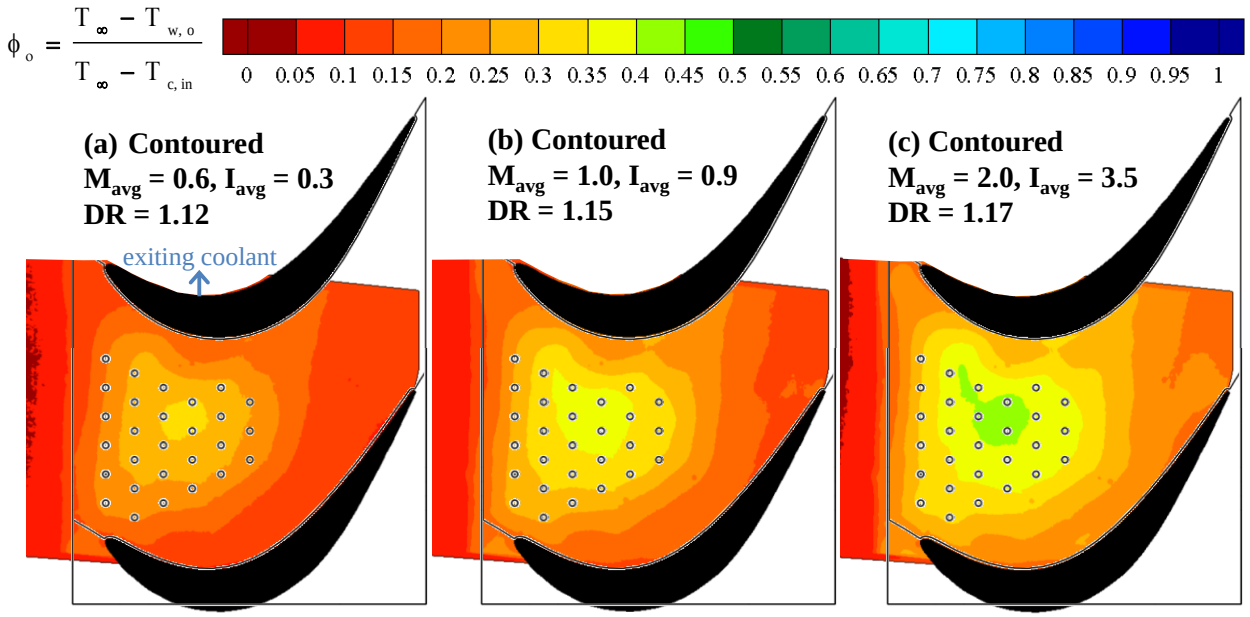

Figure 4.5. **Contoured endwall measured ϕ_o, internal impingement cooling only, for the contoured endwall for blowing ratios: (a) M_{avg} = 0.6, (b) M_{avg} = 1.0, (c) M_{avg} = 2.0 [PSU].**

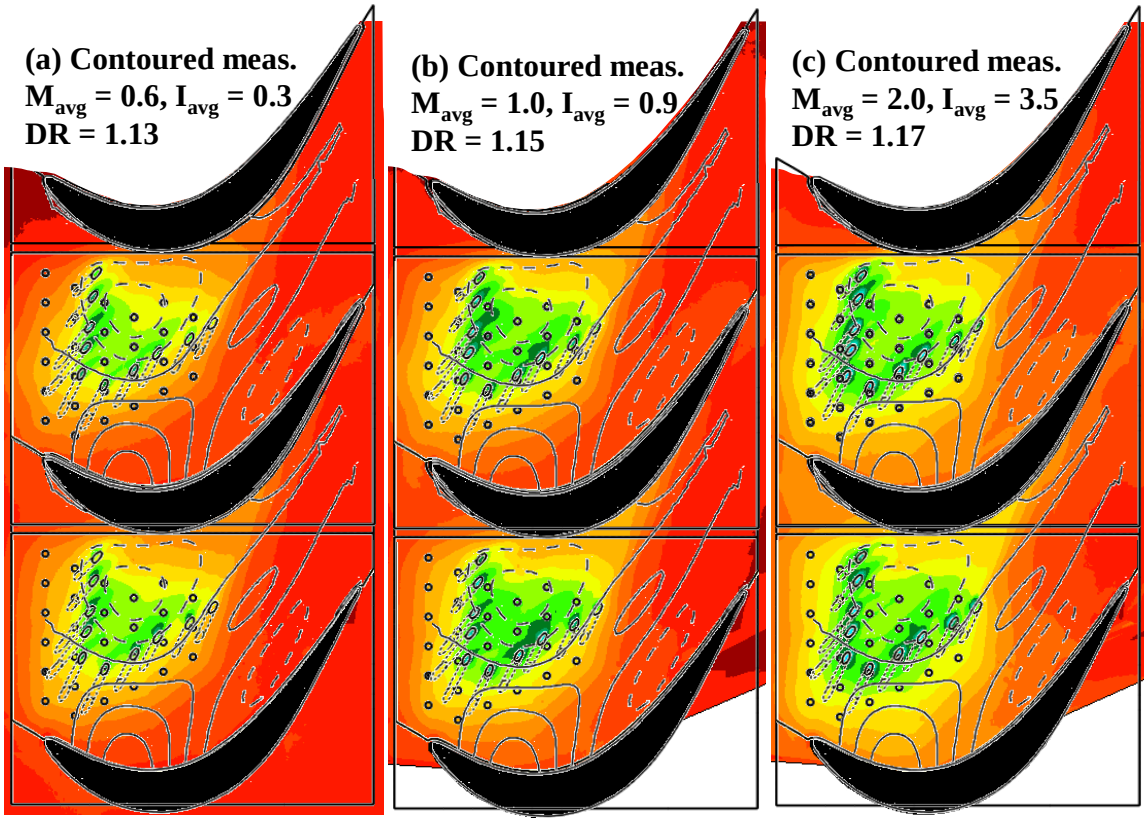

Figure 4.6. **Contoured endwall measured ϕ with internal impingement plus film cooling, for: (a) M_{avg} = 0.6, (b) M_{avg} = 1.0, (c) M_{avg} = 2.0 [PSU].**

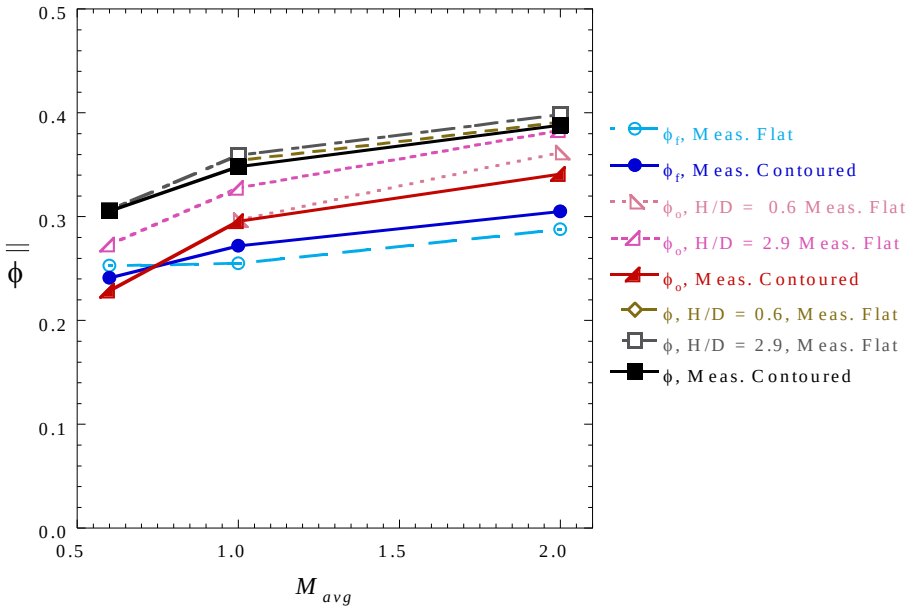

Figure 4.7. Comparison of the measured area averaged ϕ for the flat and contoured endwalls plotted as a function of M_{avg} for film cooling only (blue), impingement cooling only (red), and impingement plus film cooling (black) [PSU].

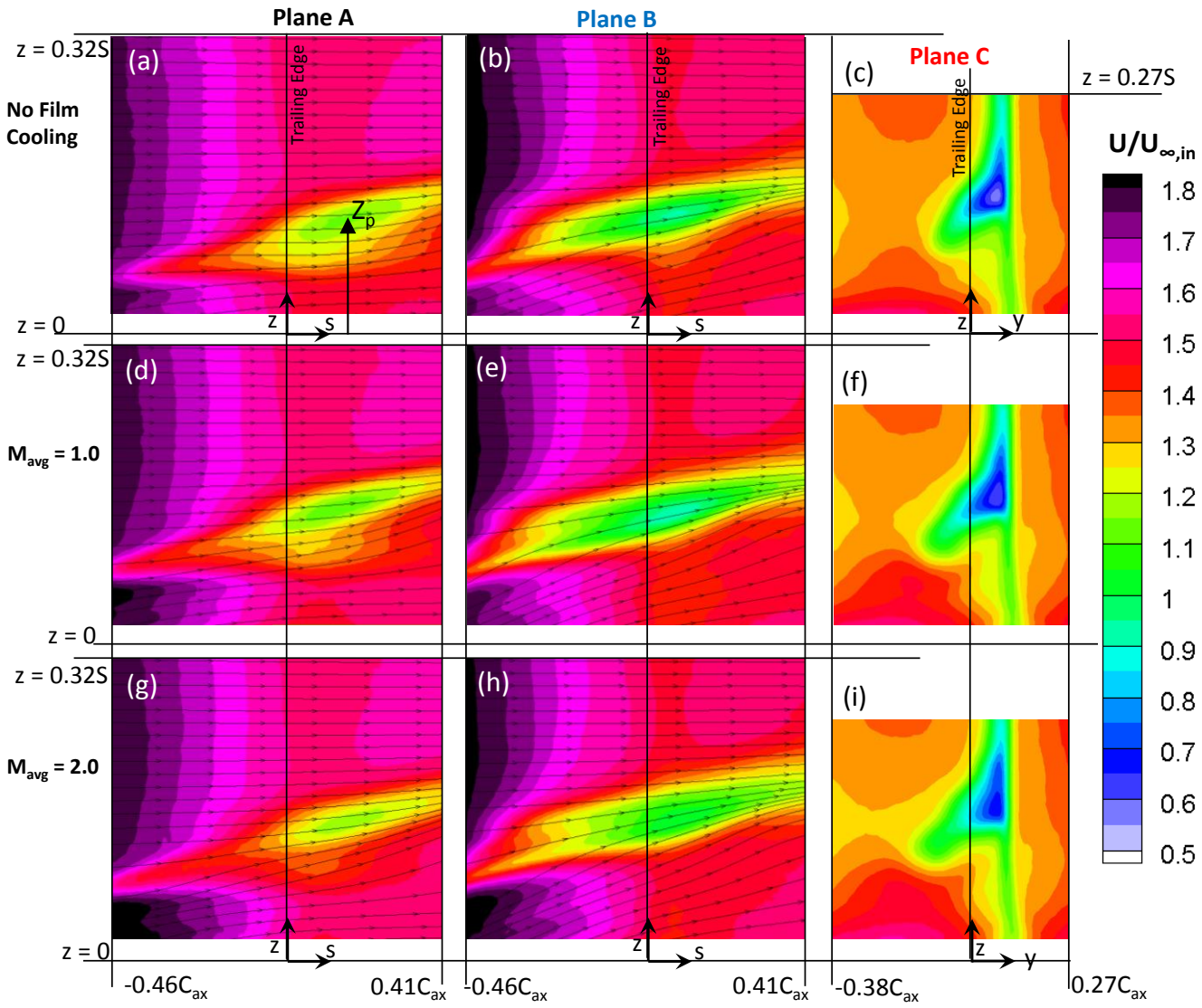

Figure 4.8. **In-plane time-averaged streamlines measured with PIV, colored by velocity magnitude for the contoured endwall for (a-c) no film cooling, (d-f) M_{avg} = 1.0, and (g-i) M_{avg} = 2.0 [PSU].**

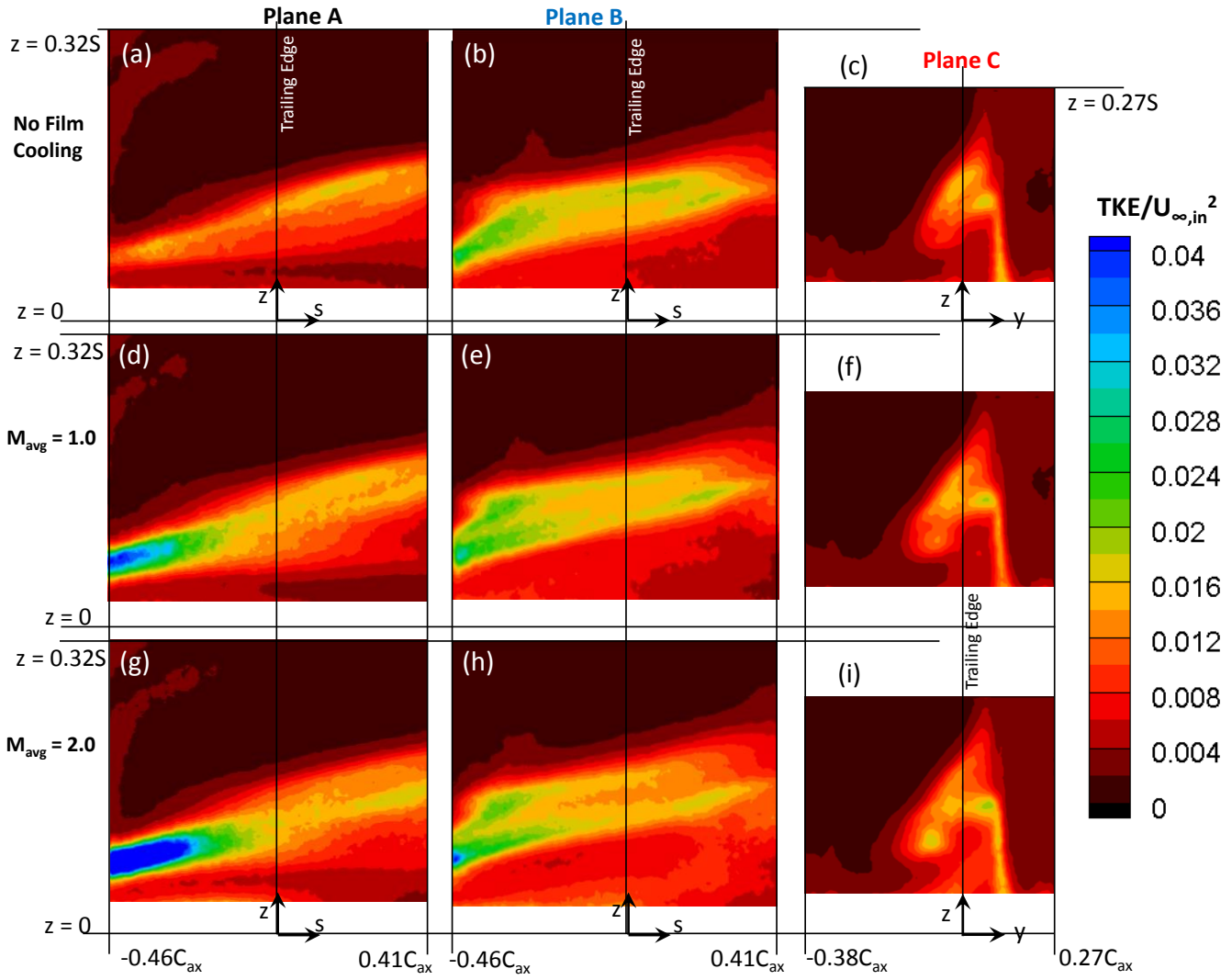

Figure 4.9. Turbulent kinetic energy measured with PIV for the contoured endwall for (a-c) no film cooling, (d-f) M_{avg} = 1.0, and (g-i) M_{avg} = 2.0 [PSU].

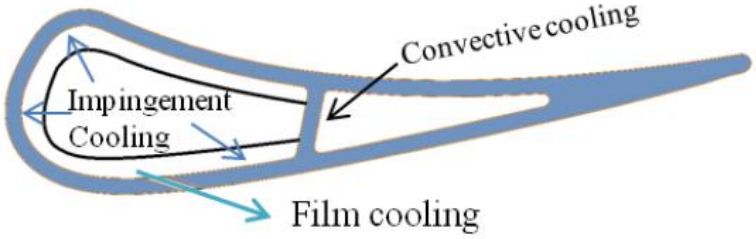

Figure 4.10. Diagram of C3X vane indicating internal cooling and film cooling location (from Dyson et al., 2012).

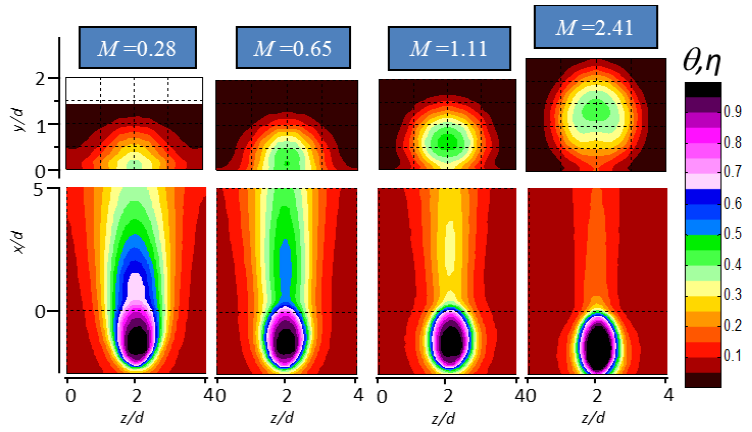

Figure 4.11. Contour plots of θ and η (not corrected for in wall conduction effects) showing good agreement at y/d=0 and x/d=5

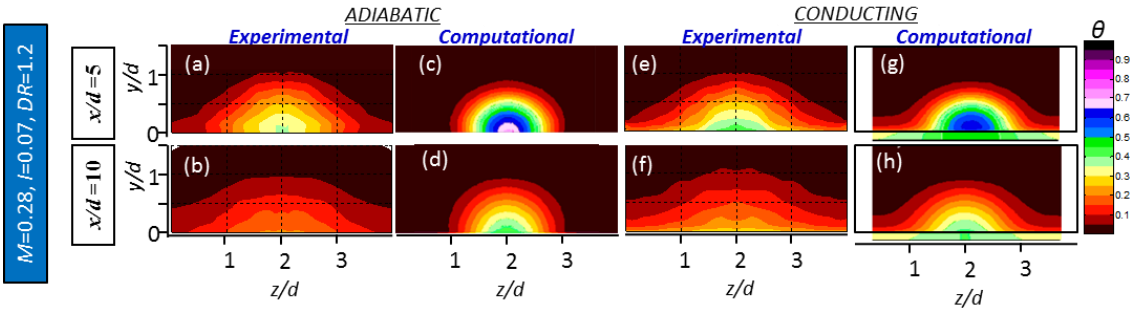

Figure 4.12. Experimental and computational (Dyson et al., 2012) thermal fields above the adiabatic and conducting vane surfaces at x/d = 5 and 10, M=0.28

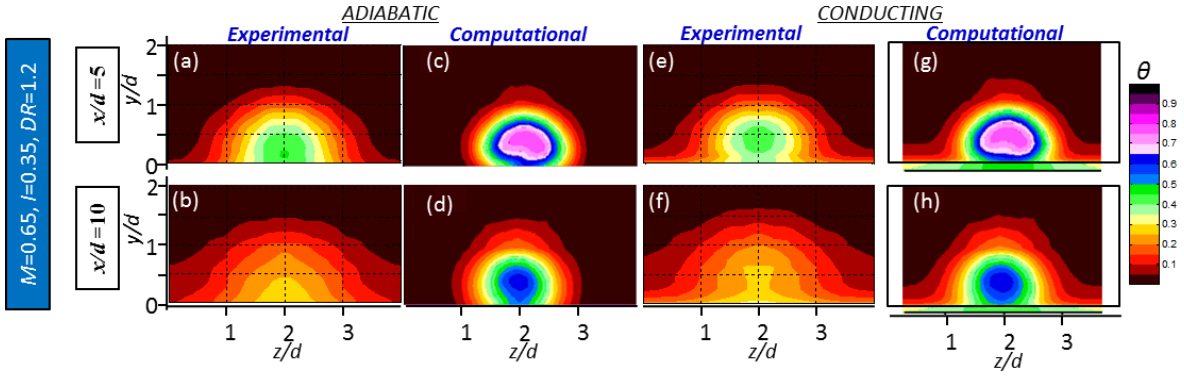

Figure 4.13. Experimental and computational [12] thermal fields above the adiabatic and conducting vane surfaces at x/d = 5 and 10, M=0.65

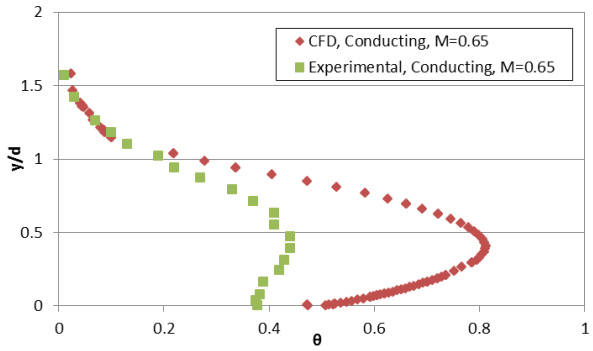

Figure 4.14. Centerline profiles of θ at x/d=5 and M=0.65 comparing experimental measurements and computational predictions (Dyson et al., 2012)

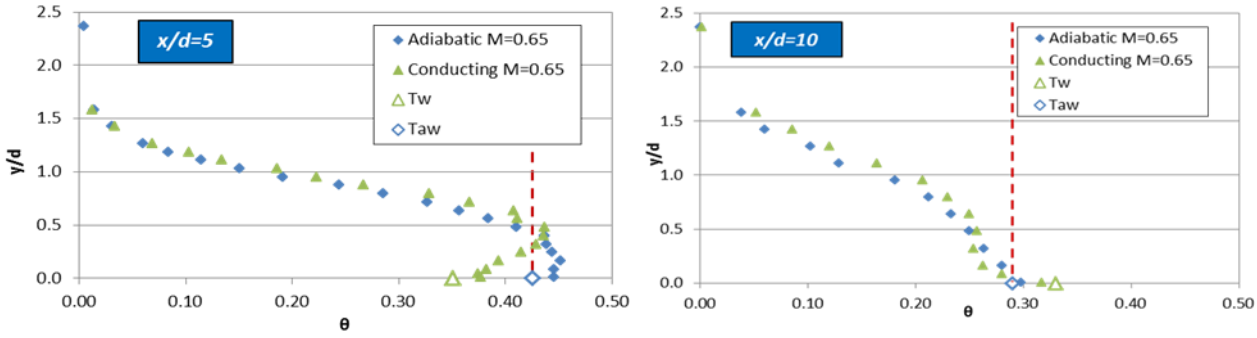

Figure 4.15. Centerline profiles of θ, z/d=2, x/d=5 and 10, M=0.65

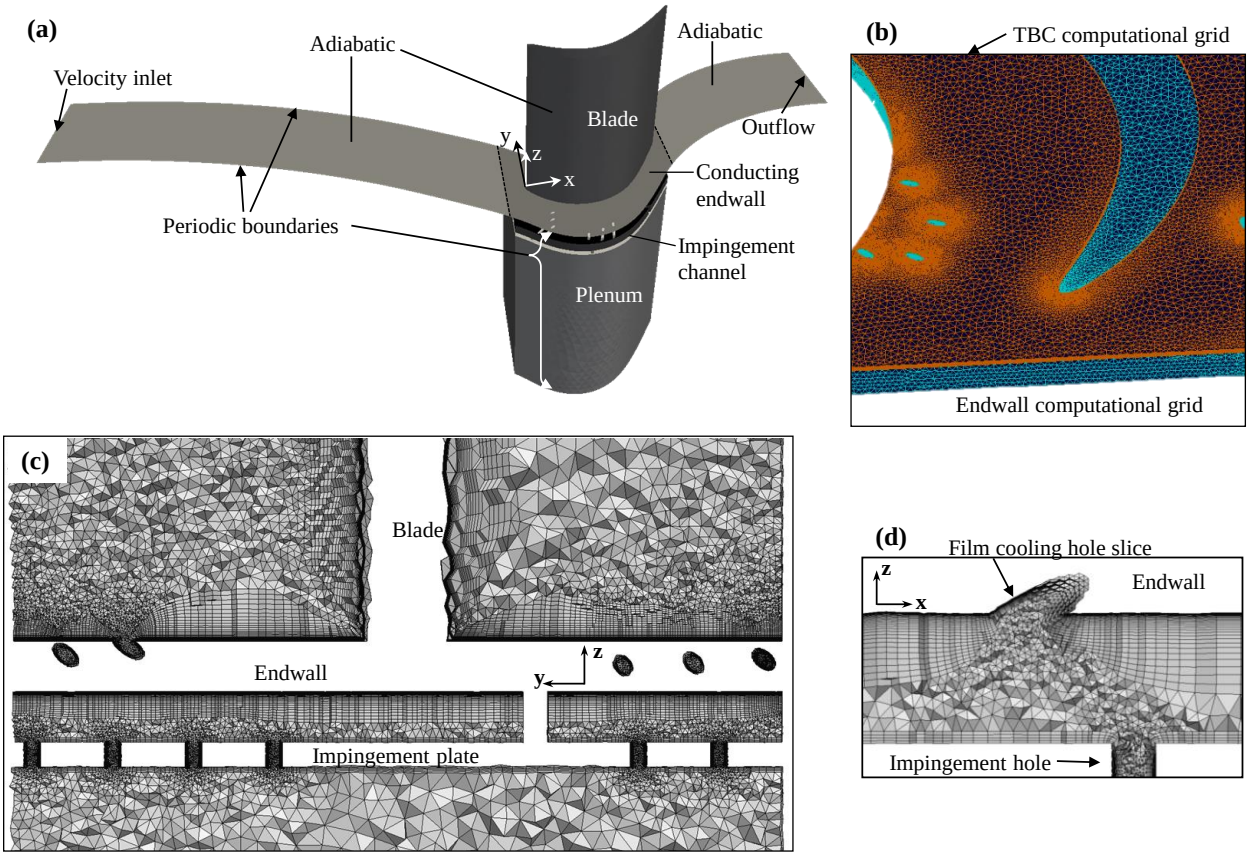

Figure 5.1. **Depiction of (a) the computational domain and boundary conditions, (b) the surface grid for the endwall and TBC, (c) the prism layer volume grid in the mainstream, channel, and plenum, and (d) the volume grid in the holes and impingement channel [PSU].**

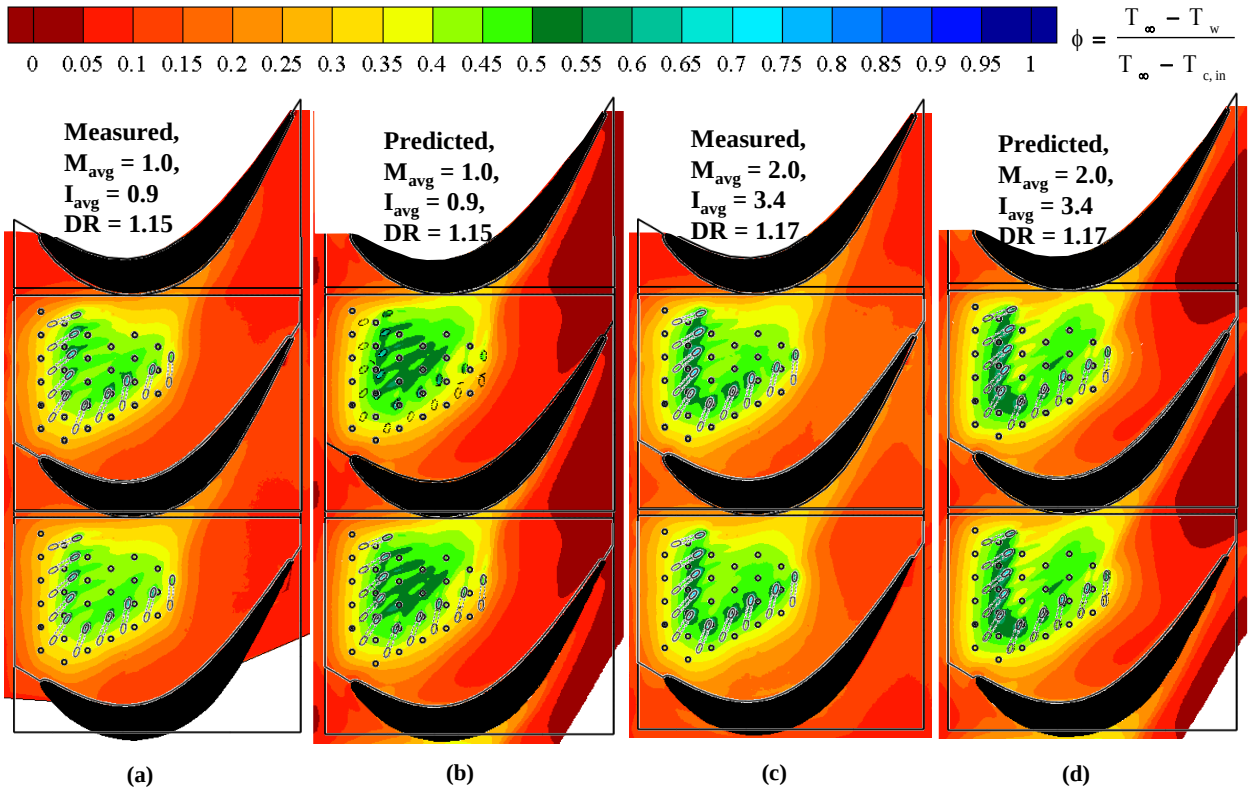

Figure 5.2. **Contours of ϕ for: (a) M_{avg} = 1.0, measured, (b) M_{avg} = 1.0, predicted, (c) M_{avg} = 2.0, measured, and (d) M_{avg} = 2.0, predicted [PSU].**

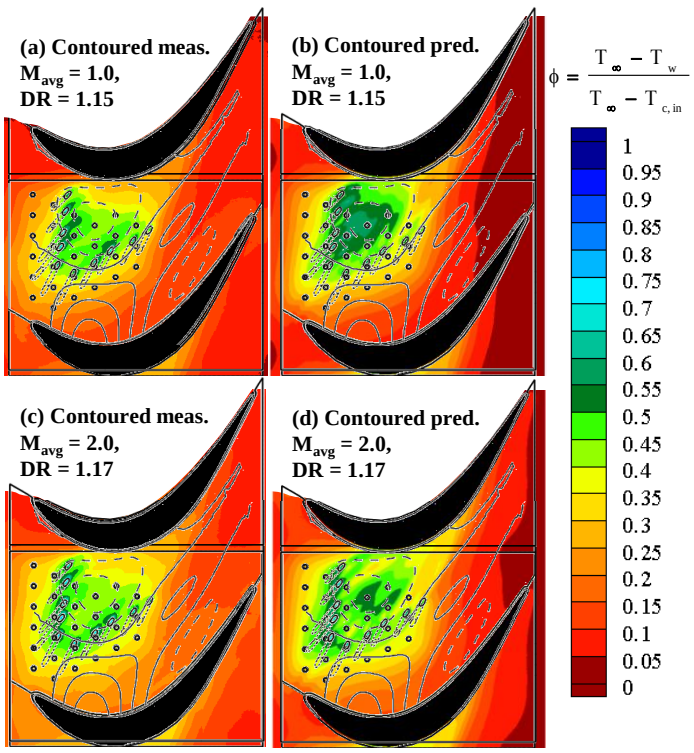

Figure 5.3. Contoured endwall overall effectiveness for (a) M_{avg} = 1.0 measured, (b) M_{avg} = 1.0 predicted, (c) M_{avg} = 2.0 measured, and (d) M_{avg} = 2.0 predicted [PSU].

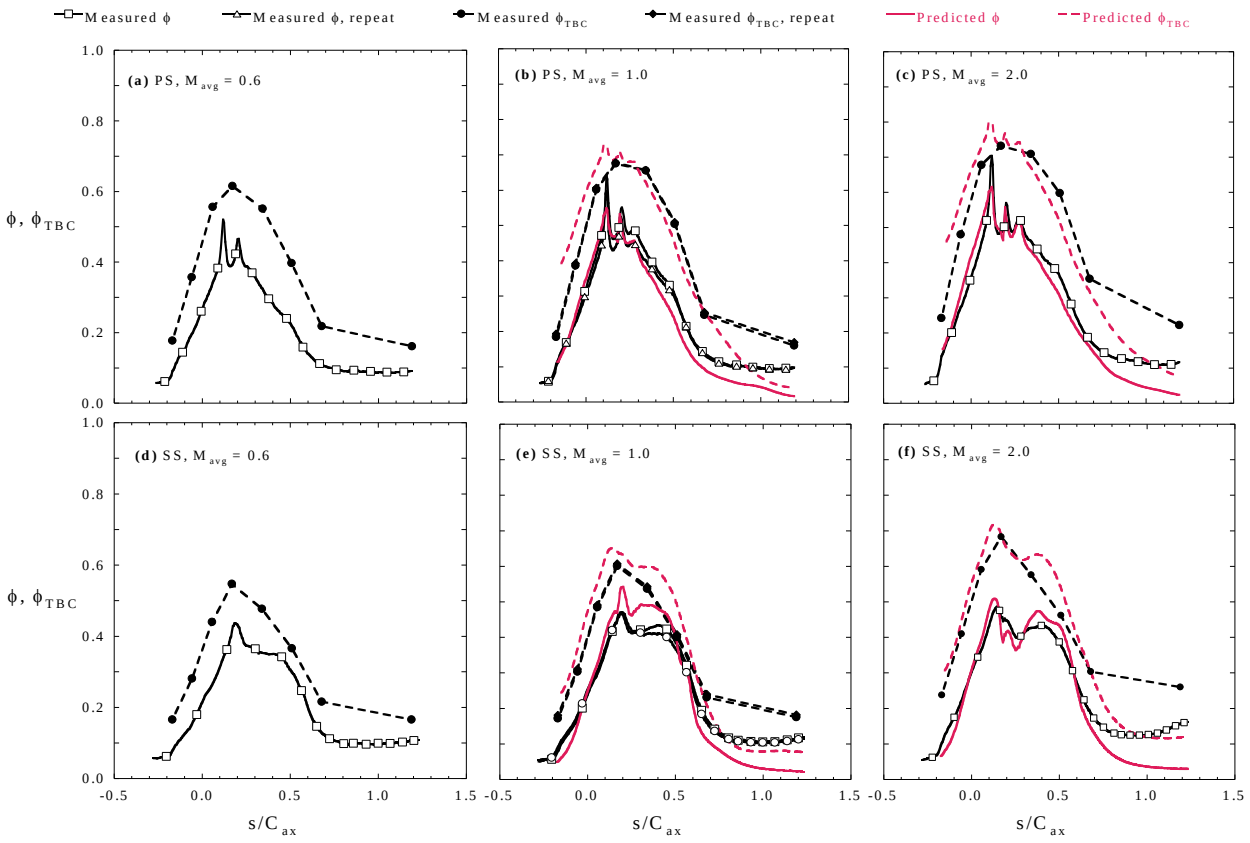

Figure 5.4. **Comparison of overall effectiveness with and without TBC, showing measured and predicted values, along inviscid streamlines, PS for a–c and SS for d–f [PSU].**

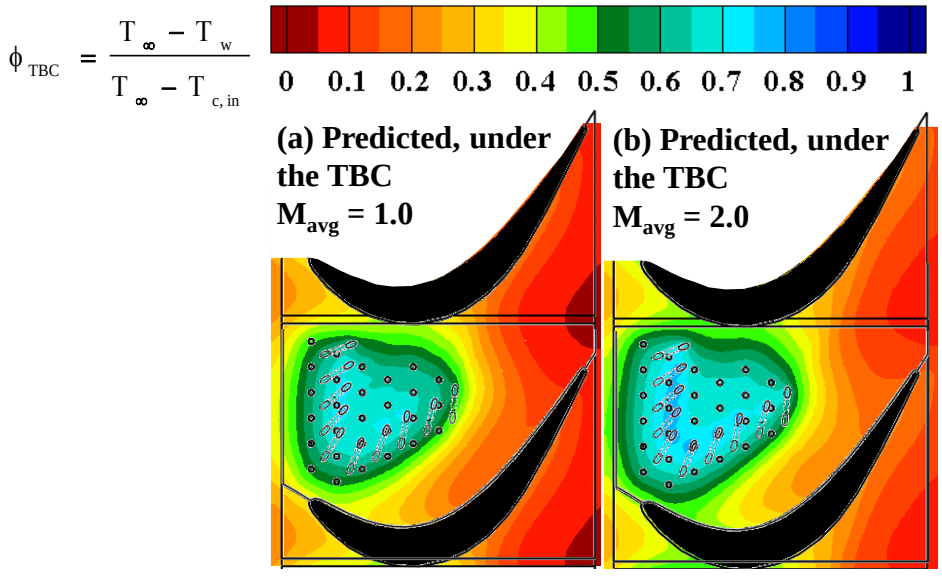

Figure 5.5. **Predicted overall effectiveness with TBC for (a) M_{avg} = 1.0 and (b) M_{avg} = 2.0 [PSU].**

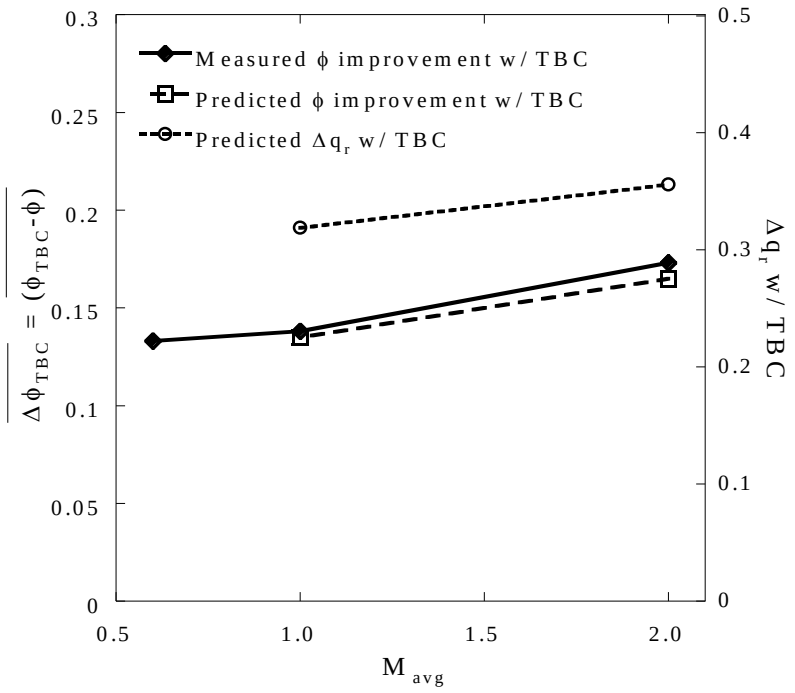

Figure 5.6. Measured and predicted improvement with TBC, $\overline{\overline{\Delta\phi_{TBC}}}$, and the predicted Δq_r for the external endwall surface plotted as a function of M_{avg} [PSU].

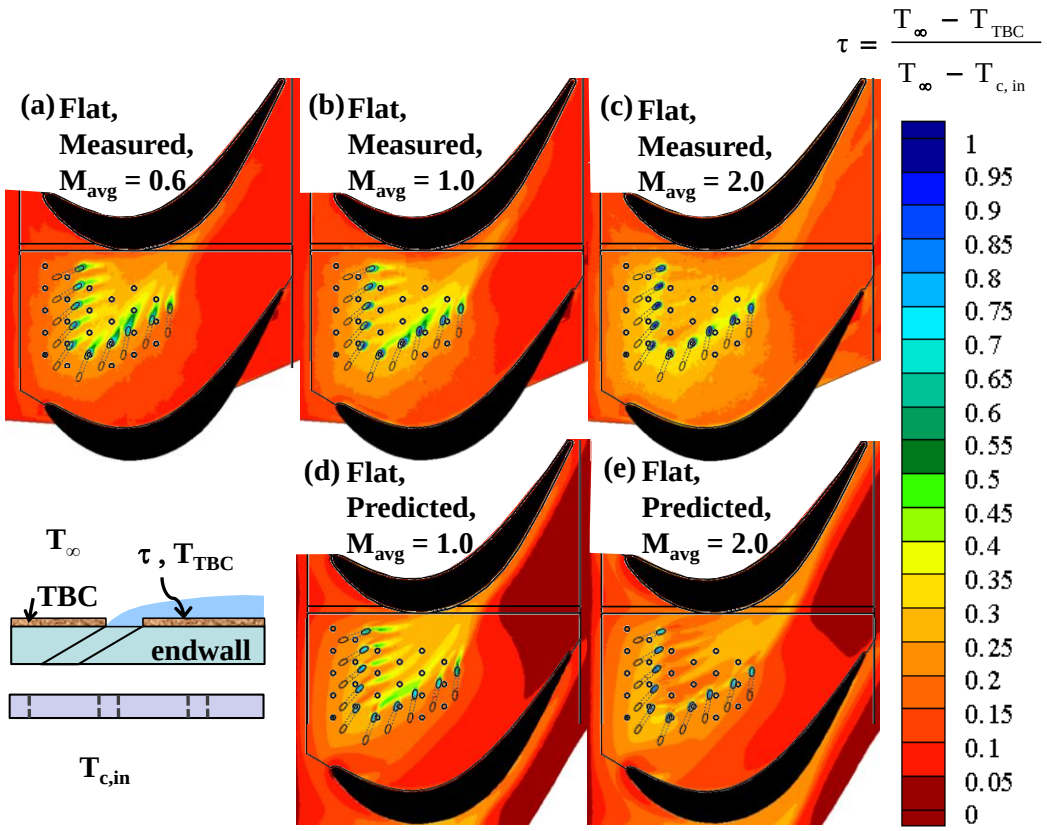

Figure 5.7. **Contours of TBC effectiveness for (a) M_{avg} = 0.6 measured, (b) M_{avg} = 1.0 measured, (c) M_{avg} = 2.0 measured, (d) M_{avg} = 1.0 predicted, and (e) M_{avg} = 2.0 predicted [PSU].**

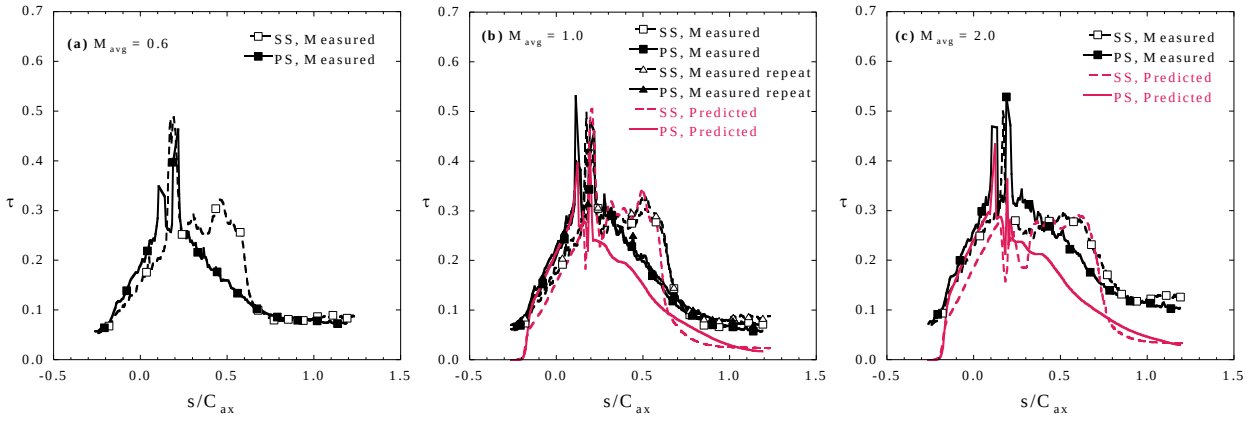

Figure 5.8. **Comparison of TBC effectiveness with film and impingement cooling, showing measured and predicted values, along inviscid streamlines, for (a) M_{avg} = 0.6, (b) M_{avg} = 1.0, and (c) M_{avg} = 2.0 [PSU].**

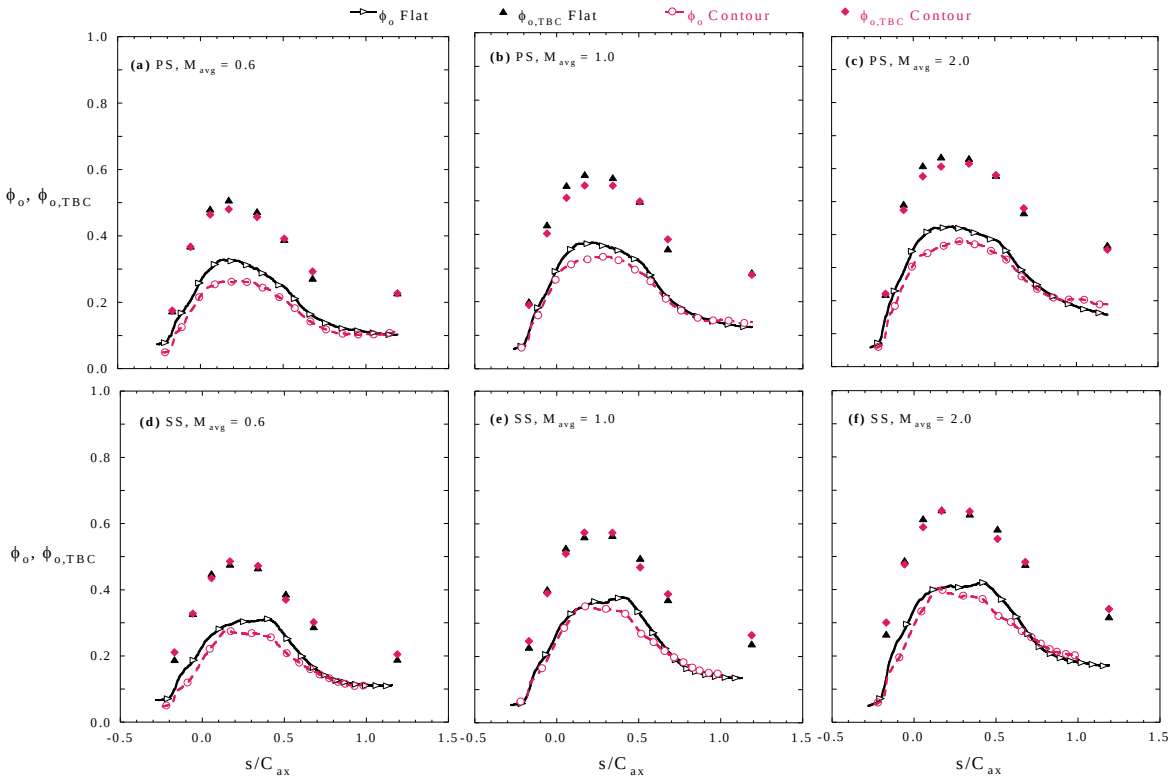

Figure 5.9. Comparison of impingement only overall effectiveness with and without TBC, for both flat and contoured endwalls, along inviscid streamlines, PS (a)–(c) and SS (d)–(f) [PSU].

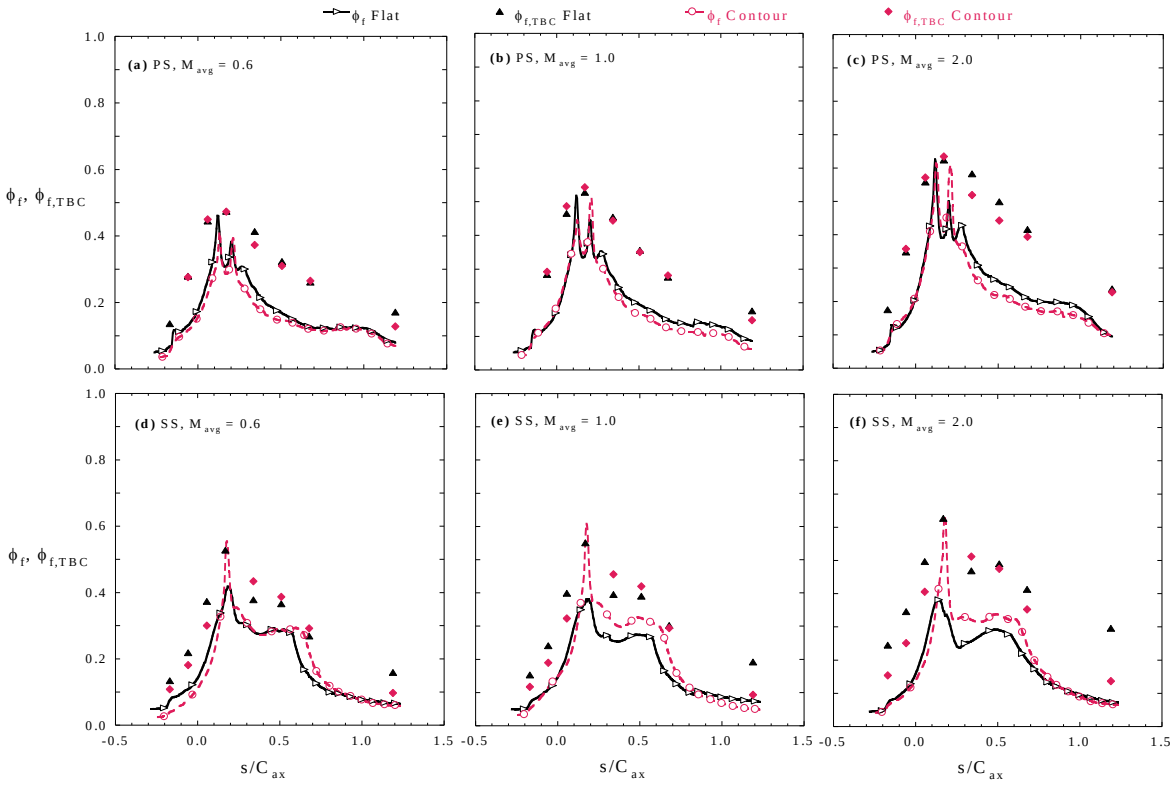

Figure 5.10. **Comparison of film cooling only overall effectiveness with and without TBC, for both flat and contoured endwalls, along inviscid streamlines, PS (a)–(c) and SS (d)–(f) (streamlines shown in Figure 7.1) [PSU].**

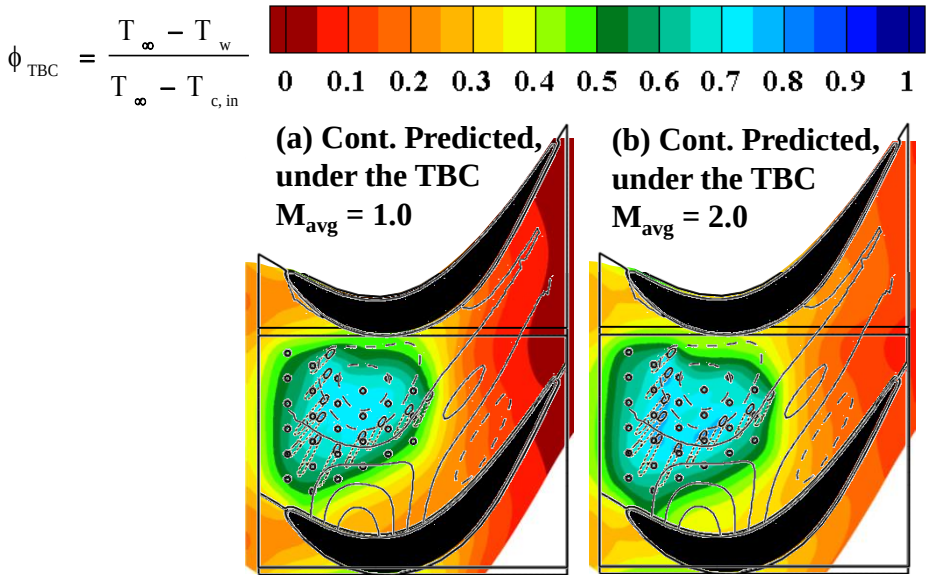

Figure 5.11. **Predicted contoured endwall overall effectiveness with TBC for (a) M_{avg} = 1.0 and (b) M_{avg} = 2.0 [PSU].**

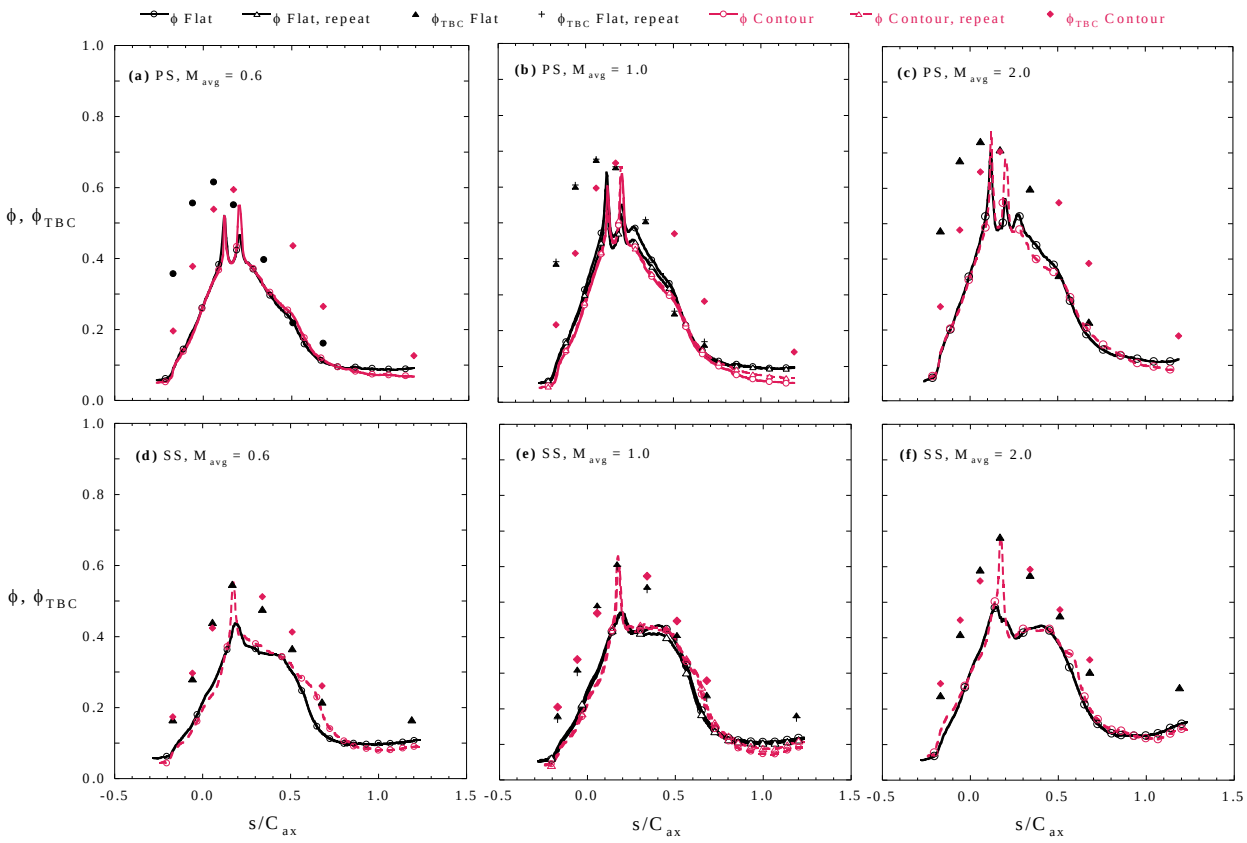

Figure 5.12. Comparison of overall effectiveness with and without TBC, for both flat and contoured endwalls, along inviscid streamlines, PS a–c and SS d–f [PSU].

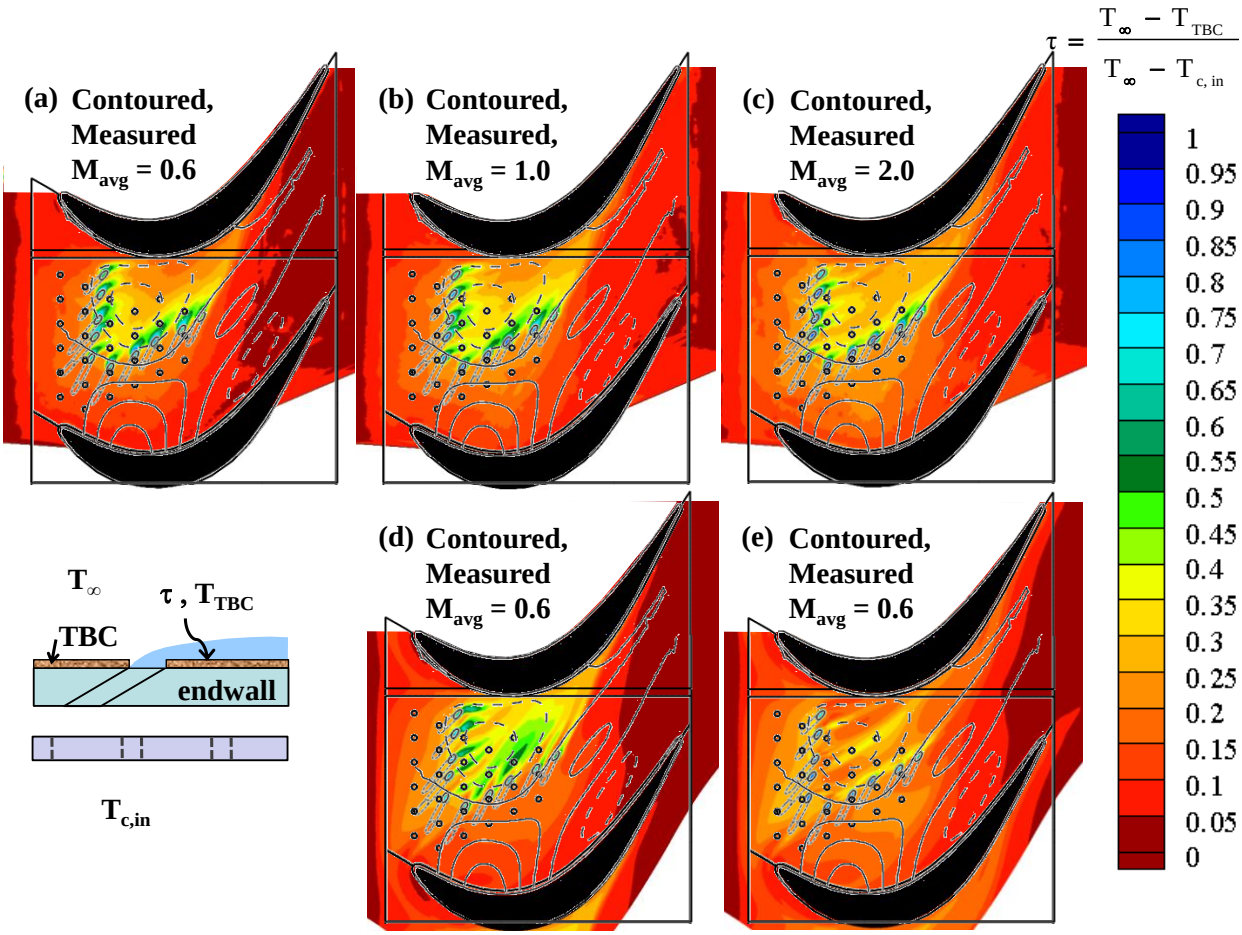

Figure 5.13. **Contoured endwall TBC effectiveness, τ, with internal impingement plus film cooling, for: (a) M_{avg} = 0.6 measured, (b) M_{avg} = 1.0 measured, (c) M_{avg} = 2.0 measured, (d) M_{avg} = 1.0 predicted, and (e) M_{avg} = 2.0 predicted [PSU].**